

# «ELECTRICAL ENGINEERING & ELECTROMECHANICS»

SCIENTIFIC & PRACTICAL JOURNAL

Journal was founded in 2002 by

National Technical University «Kharkiv Polytechnic Institute»

Co-Founder – State Institution «Institute of Technical Problems of Magnetism of the NAS of Ukraine»



## INTERNATIONAL EDITORIAL BOARD

- Klymenko B.V.** Editor-in-Chief, Professor, National Technical University "Kharkiv Polytechnic Institute" (NTU "KhPI"), Ukraine  
**Sokol Ye.I.** Deputy Editor, Professor, Corresponding member of NAS of Ukraine, rector of NTU "KhPI", Ukraine  
**Rozov V.Yu.** Deputy Editor, Professor, Corresponding member of NAS of Ukraine, Director of State Institution "Institute of Technical Problems of Magnetism of the NAS of Ukraine"(SI "ITPM NASU"), Kharkiv, Ukraine
- Batygin Yu.V.** Professor, Kharkiv National Automobile and Highway University, Ukraine  
**Bíró O.** Professor, Institute for Fundamentals and Theory in Electrical Engineering, Graz, Austria  
**Bolyukh V.F.** Professor, NTU "KhPI", Ukraine  
**Doležel I.** Professor, University of West Bohemia, Pilsen, Czech Republic  
**Féliachi M.** Professor, University of Nantes, France  
**Gurevich V.I.** Ph.D., Honorable Professor, Central Electrical Laboratory of Israel Electric Corporation, Haifa, Israel  
**Kildishev A.V.** Associate Research Professor, Purdue University, USA  
**Kuznetsov B.I.** Professor, SI "ITPM NASU", Kharkiv, Ukraine  
**Kyrylenko O.V.** Professor, Member of NAS of Ukraine, Institute of Electrodynamics of NAS of Ukraine, Kyiv, Ukraine  
**Podoltsev A.D.** Professor, Institute of Electrodynamics of NAS of Ukraine, Kyiv, Ukraine  
**Rainin V.E.** Professor, Moscow Power Engineering Institute, Russia  
**Rezynkina M.M.** Professor, SI "ITPM NASU", Kharkiv, Ukraine  
**Rožanov Yu.K.** Professor, Moscow Power Engineering Institute, Russia  
**Shkolnik A.A.** Ph.D., Central Electrical Laboratory of Israel Electric Corporation, member of CIGRE (SC A2 - Transformers), Haifa, Israel  
**Yufarov V.B.** Professor, National Science Center "Kharkiv Institute of Physics and Technology", Ukraine  
**Vinitzki Yu.D.** Professor, GE EEM, Moscow, Russia  
**Zagirnnyak M.V.** Professor, Corresponding member of NAES of Ukraine, rector of Kremenchuk M.Ostrohradskyi National University, Ukraine  
**Zgraja J.** Professor, Institute of Applied Computer Science, Lodz University of Technology, Poland

## НАЦІОНАЛЬНА РЕДАКЦІЙНА КОЛЕГІЯ\*

- Клименко Б.В.** головний редактор, професор, НТУ "ХПІ"  
**Сокол Є.І.** заступник головного редактора, член-кор. НАНУ, ректор НТУ "ХПІ"  
**Розов В.Ю.** заступник головного редактора, член-кор. НАНУ, директор ДУ "ІТПМ НАНУ"  
**Гречко О.М.** відповідальний секретар, к.т.н., НТУ "ХПІ"  
**Баранов М.І.** д.т.н., НДПКи "Молнія" НТУ "ХПІ"  
**Боев В.М.** професор, НТУ "ХПІ"  
**Веприк Ю.М.** професор, НТУ "ХПІ"  
**Гриб О.Г.** професор, НТУ "ХПІ"  
**Гурин А.Г.** професор, НТУ "ХПІ"  
**Данько В.Г.** професор, НТУ "ХПІ"  
**Жемеров Г.Г.** професор, НТУ "ХПІ"  
**Клепиков В.Б.** професор, НТУ "ХПІ"  
**Кравченко В.І.** професор, директор НДПКи "Молнія" НТУ "ХПІ"  
**Міліх В.І.** професор, НТУ "ХПІ"  
**Михайлов В.М.** професор, НТУ "ХПІ"  
**Омельяненко В.І.** професор, НТУ "ХПІ"  
**Пуйло Г.В.** професор, ОНТУ, Одеса  
**Резинкін О.Л.** професор, НТУ "ХПІ"  
**Сосков А.Г.** професор, ХНУМГ імені О.М. Бекетова, Харків  
**Ткачук В.І.** професор, НУ "Львівська Політехніка"  
**Шинкаренко В.Ф.** професор, Національний технічний університет України "Київський політехнічний інститут"

\* Члени національної редакційної колегії працюють у провідних українських наукових, освітніх та дослідницьких установах

## NATIONAL EDITORIAL BOARD\*

- Klymenko B.V.** Editor-in-Chief, professor, NTU "KhPI"  
**Sokol Ye.I.** Deputy Editor, corresponding member of NAS of Ukraine, rector of NTU "KhPI"  
**Rozov V.Yu.** Deputy Editor, corresponding member of NAS of Ukraine, Director of SI "ITPM NASU"  
**Grechko O.M.** Executive Managing Editor, Ph.D., NTU "KhPI"  
**Baranov M.I.** Dr.Sc. (Eng.), NTU "KhPI"  
**Boev V.M.** Professor, NTU "KhPI"  
**Vepryk Yu.M.** Professor, NTU "KhPI"  
**Gryb O.G.** Professor, NTU "KhPI"  
**Guryn A.G.** Professor, NTU "KhPI"  
**Dan'ko V.G.** Professor, NTU "KhPI"  
**Zhemerov G.G.** Professor, NTU "KhPI"  
**Klepikov V.B.** Professor, NTU "KhPI"  
**Kravchenko V.I.** Professor, NTU "KhPI"  
**Milykh V.I.** Professor, NTU "KhPI"  
**Mikhaylov V.M.** Professor, NTU "KhPI"  
**Omel'yanenko V.I.** Professor, NTU "KhPI"  
**Puilo G.V.** Professor, Odessa National Polytechnic University  
**Rezynkin O.L.** Professor, NTU "KhPI"  
**Soskov A.G.** Professor, O.M. Beketov National University of Urban Economy in Kharkiv  
**Tkachuk V.I.** Professor, Lviv Polytechnic National University  
**Shynkarenko V.F.** Professor, National Technical University of Ukraine "Kyiv Polytechnic Institute"

\* Members of National Editorial Board work in leading Ukrainian scientific, educational and research institutions

## Адреса редакції / Editorial office address:

Кафедра "Електричні апарати", НТУ "ХПІ", вул. Кирпичова, 21, м. Харків, 61002, Україна  
Dept. of Electrical Apparatus, NTU "KhPI", Kyrpychova Str., 21, Kharkiv, 61002, Ukraine

тел. / phone: +380 57 7076281, +380 67 3594696, e-mail: a.m.grechko@gmail.com (Гречко Олександр Михайлович / Grechko O.M.)

ISSN (print) 2074-272X

© National Technical University «Kharkiv Polytechnic Institute», 2016

ISSN (online) 2309-3404

© State Institution «Institute of Technical Problems of Magnetism of the NAS of Ukraine», 2016

Printed 23.12.2016. Format 60 x 90 1/8. Paper – offset. Laser printing.

Edition 200 copies. Order no.66/172-06-2016.

Design of cover by Vyrovets L.P. e-mail: vsv\_2007@ukr.net

Printed by Printing house «Madrid Ltd» (11, Maksymilianivska Str., Kharkiv, 61024, Ukraine)



**2016/6**

**TABLE OF CONTENTS**

***Electrical Engineering. Great Events. Famous Names***

**Baranov M.I.** An anthology of the distinguished achievements in science and technique. Part 35: Nobel Prize Laureates in Physics for 1990-1994..... 3

***Electrical Machines and Apparatus***

**Kulinchenko G.V., Maslennikov A.M., Baguta V.A.** Research of dynamic parameters of the electric drive on the basis of rolling rotor motor..... 9

**Matyushenko A.V.** Analysis of thermal state of traction brushless permanent motor for mine electric locomotive ..... 15

**Milykh V.I.** A turbo-generator design synthesis based on the numerical-field calculations at varying the number of stator slots..... 19

***Electrotechnical Complexes and Systems. Power Electronics***

**Kuznetsov B.I., Nikitina T.B., Voloshko A.V., Bovdyj I.V., Vinichenko E.V., Kobilyanskiy B.B.** Synthesis of an active shielding system of the magnetic field of power lines based on multiobjective optimization ..... 26

**Tugay D.V.** The phase reactor inductance selection technique for power active filter ..... 31

**Yushkov E.A.** Modeling of operation modes of ship power plant of combined propulsion complex with control system based on electronic controllers..... 39

***Theoretical Electrical Engineering and Electrophysics***

**Baranov M.I., Rudakov S.V.** Calculation-experimental method of research in a metallic conductor with the pulse current of electronic wavepackages and de Broglie electronic half-waves..... 45

***High Electric and Magnetic Field Engineering. Cable Engineering***

**Bezprozvannykh G.V., Kyessayev A.G.** The technological and exploitative factors of local increase of electric field strength in the power cable of coaxial design..... 54

***Power Stations, Grids and Systems***

**Nizhevskiy I.V., Nizhevskiy V.I., Bondarenko V.E.** The experimental validation of the grounding device resistance measurement method..... 60

**Sayenko Yu.L., Kalyuzhniy D.N.** Identification of generalized linear load in three-phase three-wire network in the problem of the distribution of actual contributions at the point of common coupling..... 65

**Khomenko I.V., Berezka S.K., Poliakov I.V.** Analysis of optimum operating modes of power transformers under operating conditions..... 70

M.I. Baranov

## AN ANTHOLOGY OF THE DISTINGUISHED ACHIEVEMENTS IN SCIENCE AND TECHNIQUE. PART 35: NOBEL PRIZE LAUREATES IN PHYSICS FOR 1990-1994

*Purpose. Implementation of brief analytical review of the distinguished scientific achievements of the world scientists-physicists, awarded the Nobel Prize in physics for period 1990-1994. Methodology. Scientific methods of collection, analysis and analytical treatment of scientific and technical information of world level in area physics of elementary particles, physics of high energies, of astrophysics, of modern theoretical and experimental physics. Results. The brief analytical review of the scientific openings and distinguished achievements of scientists-physicists is resulted in area of modern physical and technical problems which were marked the Nobel Prize in physics for period 1990-1994. Originality. Systematization is executed with exposition in the short concentrated form of the known scientific and technical materials, devoted pioneer researches results on dispersion of relativism electrons on protons (neutrons), to opening of likenesses of physics of hard matter and physics of the condensed state of matter, creation of revolutionary detector of elementary particles, to opening of new pulsars and new possibilities in the study of gravitation, to creation of neutron spectroscopy and method of neutron diffraction. Practical value. Popularization and deepening of scientific and technical knowledges for students, engineer and technical specialists and research workers in area of modern theoretical and experimental physics, extending their scientific range of interests and cooperant further development of scientific and technical progress in human society. References 25, figures 12.*

*Key words: modern physics, achievements, dispersion of relativism electrons on heavy particles, physics of hard matter and condensed state, multielectrode detector of elementary particles, new pulsars and gravitation, neutron spectroscopy and diffraction, review.*

*Приведен краткий аналитический обзор выдающихся научных достижений ученых мира, отмеченных Нобелевской премией по физике за период 1990-1994 гг. В число таких достижений вошли результаты пионерских исследований по рассеянию релятивистских электронов на протонах и нейтронах, открытие сходств физики твердой материи и физики конденсированного состояния вещества, создание революционного детектора элементарных частиц, открытие новых пульсаров и новые возможности в изучении гравитации, создание нейтронной спектроскопии и метода нейтронной дифракции. Библи. 25, рис. 12.*

*Ключевые слова: современная физика, достижения, рассеяние релятивистских электронов на тяжелых частицах, физика твердой материи и конденсированного состояния, мультиэлектродный детектор элементарных частиц, новые пульсары и гравитация, нейтронная спектроскопия и дифракция, обзор.*

**Introduction.** The world-renowned Swedish engineer, inventor of explosives and businessman Alfred Nobel (1833-1896) bequeathed to the respective fund 31.5 million SEK (at the time of about 5 million USD) [1] for the monetary rewards of the future Nobel Prize winners perpetrators of outstanding discoveries in physics and chemistry, and have achieved outstanding results in the field of physiology (medicine), literature and peace among peoples. We note that, personally handed the outstanding German experimental physicist Wilhelm Conrad Roentgen (1845-1923) «for the discovery of X-rays» [2] for 1901 the first Nobel Prize in Physics was, but gold medals (Fig. 1) and diploma embodiment, similar to that shown in Fig. 2, and relied check in the amount of 150 thousand SEK [3].



Fig. 1. Constant view of obverse and reverse of the gold medal of winners of the Nobel Prize in Physics [2, 3]

Over time, the amount of monetary award to the group of authors (no more than three co-authors) of this prestigious international award was increased and in 2011 was already 10 million SEK (1.3 million USD) [2, 3].

Taking into account the importance of the scientific results of Nobel Laureates, professional scientific interest of the author – electrophysicist and scientific and technical profile of our Journal, we will try, by five short essays in its five issues to present the principal outstanding achievements in science and technology by only Nobel Prize Laureates in Physics for the current period 1990-2015.

**1. The scattering of electrons on the elementary particles and the quark model in particle physics.** In 1990, «for pioneering studies of deep inelastic scattering of electrons on protons and coupled neutrons, which are essential for the development of the quark model in particle physics» American experimental physicists Jerome Isaac Friedman (Fig. 3) and Henry Way Kendall (Fig. 4) and Canadian-American experimental physicist Richard Edward Taylor (Fig. 5) have been awarded the most important in science Nobel Prize in physics [2, 6-8].

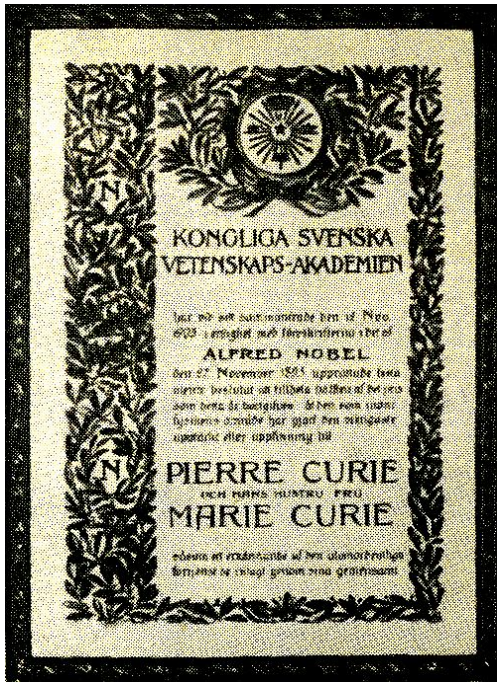


Fig. 2. Exterior of the Nobel Diploma of Prize Laureates in Physics for 1903 the prominent French experimental physicists Pierre and Marie Curie [4, 5]

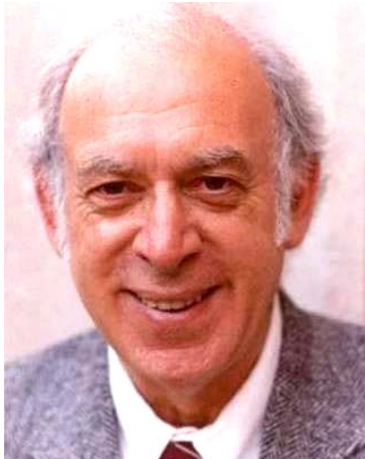


Fig. 3. Prominent American experimental physicist Jerome Isaac Friedman, born in 1930, Nobel Prize Laureate in physics for 1990

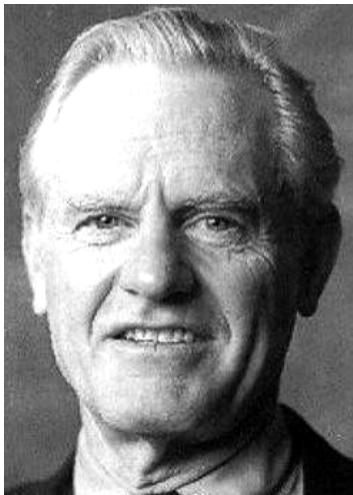


Fig. 4. Prominent American experimental physicist Henry Way Kendall (1926-1999), Nobel Prize Laureate in physics for 1990

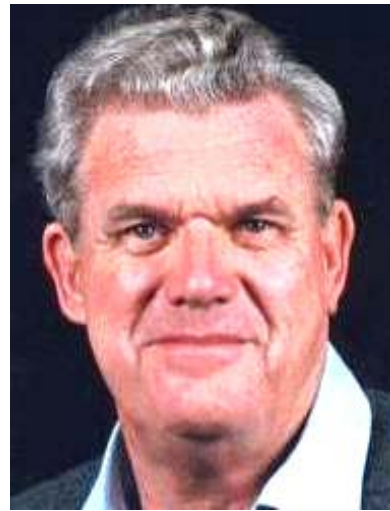


Fig. 5. Prominent Canadian-American experimental physicist Richard Edward Taylor born in 1929, Nobel Prize Laureate in physics for 1990

In the period 1967-1973 J.A. Friedman [6] together with his colleagues H.W. Kendall [7] and R.E. Taylor [8] conducted a complex of important in the field of high energy physics experimental studies on the newly launched into operation (in 1967) the world's largest Stanford electron linear accelerator on energy to 21 GeV at the length of his accelerator vacuum tube of 2 miles (about 3200 m) [2, 5]. The aim of this work was to determine the characteristics of the scattering of electrons accelerated to relativistic speeds beginning with protons in the future related to the breeder. It was assumed that electrons accelerated in the accelerator of charged particles to speeds close to the speed of light in a vacuum, «will» through or the «jump» the said elementary particles [6]. However, in practice it turned out that most of these electrons «bounced» from protons at different angles. And so that these nuclear physicists evolved the belief that the accelerated electrons consist of smaller elementary particles, whereas conventionally called «quarks»[6]. According to modern concepts under the «quark» in the elementary particle physics meant a hypothetical elementary particles with fractional electric charge ( $1/3$  and  $2/3$  of the electron charge  $e_0=1.602 \cdot 10^{-19}$  K) of which may consist of elementary particles (e.g., hadrons, including such heavy particles like baryons with half-integer spin, which the weight of no less than the mass of the proton), involved in strong interactions [9, 10]. As a result of processing results performed pioneering experiments and classifications found particles of the nuclear physicists presented the international scientific community a set of «quark», named [6]: up, down, charm, strange, truth and beauty. Received by them on the Stanford electron linear accelerator experimental data were extremely important for the development of modern physics, the quark structure of elementary particles [2, 6-8].

**2. Opening many similarities of physics of solid matter and the physics of condensed matter.** In 1991, the Nobel Prize in Physics was awarded the French physicist Pierre-Gilles de Gennes (Fig. 6) «for discovering that methods developed for studying order in phenomena in simple systems can be generalized to liquid

*crystals and polymers*» [2, 11]. According to the data given in [11], P.-G. de Gennes in 1968 switched to the study of liquid crystals. Over time, he became a leading physicist in the field of polymer and colloidal systems. In 1977 he published the monograph «The Physics of Liquid Crystals» which is to this day a basic tool in this research field. [11] He is one of the founders of the physics of liquid crystals. Its share had the honor to become a pioneer in the field of physics of soft materials - polymers, surfactants, liquid crystals and colloidal systems. It is with P.-G. de Gennes was opened physico-chemical structure (ferroelectric smectic), marked the beginning of the production of liquid crystal displays for computers, TV-sets and mobile phones [11-13]. For a number of fundamental developments in the field of physics they called him «Newton of our time» [2, 11].

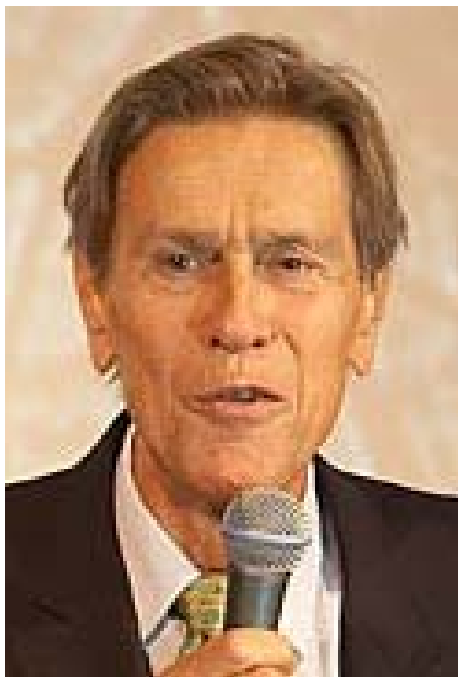


Fig. 6. Prominent French physicist Pierre-Gilles de Gennes (1932-2007), Nobel Prize Laureate in physics for 1991

After receiving the Nobel Prize P.-G. de Gennes became Director of the «École Supérieure de Physique et de Chimie Industrielles de la Ville de Paris» ( ESPCI). [11] At this highest administrative and academic position he remained until 2002. A lot of time and energy he devoted to educational institutions of France, while sharing with the students and the students of his scientific knowledge.

**3. The invention of proportional chamber and particle detectors.** In 1992, «for the discovery and creation of particle detectors, in particular the multiwire proportional chamber» French experimental physicist Georges Charpak (Fig. 7) was awarded the Nobel Prize in physics [14].

Our next winner of the Nobel Prize G. Charpak had difficult for his generation and at the same time bright human destiny. He was born in the Polish village of Dąbrowica (now the city of Dubrovitsa, Ukraine) in a Jewish family of Polish origin. In 1931 his family moved to Paris.



Fig. 7. Prominent Polish-French experimental physicist Georges Charpak (1924-2010), Nobel Prize Laureate in physics for 1992.

During World War II he participated in the resistance movement, fighting against Nazi Germany. In the period of 1944-1945 in difficult conditions he was in a Nazi concentration camp Dachau near Munich [15]. In 1945, after his release, he joined the Parisian École des Mines – one of the most prestigious engineering schools in France (since 1946 he was naturalized French citizen). After receiving the Bachelor degree in 1948, G. Charpak started to work at the National Center for Scientific Research, and later in a scientific laboratory at the «Collège de France» of outstanding nuclear physicist, Nobel Prize Laureate in Chemistry for 1935 (together with his wife Irene Curie - the sister of Eve Curie [4] «for discovery of artificial radioactivity and synthesis of new radioactive elements») Frederic Joliot-Curie [2, 5] (1900-1958). In 1954 he defended his Doctoral Thesis on the results of his work in this laboratory in the field of nuclear physics [15]. In 1959, G. Charpak became a member of the research team at the European Center for Nuclear Research (CERN, Geneva, Switzerland). In this scientific center G. Charpak in 1968 and made his important scientific discovery – he created a multielectrode proportional chamber («Charpak chamber») for the detection of elementary particles [16]. Connection of this camera (this detector) with a computer, according to the inventor of this original physical-technical device, increased the speed of gathering information about the test particles millions of times [16]. At present, none of the experiment in the field of high energy physics is possible without such «Charpak detector». This invention was of revolutionary character in the field of elementary particle physics [2, 16].

**4. The discovery of new pulsars, and new possibilities for the study of gravitation.** In 1993, «for the discovery of a new type of pulsar which gave new possibilities for the study of gravitation» American physicists-astronomers Russell Alan Hulse (Fig. 8) and Joseph Hooton Taylor Jr. (Fig. 9) received the Nobel Prize in physics [17, 18] . Their astronomical discoveries related to the discovery of the universe of double pulsar

PSR B1913+16 R.A. Hulse and J.H. Taylor Jr. made in 1974 carrying out joint astronomy observations on the unique US radio telescope «Arecibo» (Fig. 10), established in Central America (Puerto Rico) having a perforated aluminum parabolic reflector with a diameter of 305 m [17-19].



Fig. 8. Prominent American physicist-astronomer Russell Alan Hulse, born in 1950, Nobel Prize Laureate in physics for 1993



Fig. 9. Prominent American physicist-astronomer Joseph Hooton Taylor Jr., born in 1941, Nobel Prize Laureate in physics for 1993

Recall that under the «pulsars» (this term is from the English word «pulsars» - «pulsed radiation sources» [9]) refers to cosmic sources coming to Earth radio, optical, X-ray and gamma radiation. In radio pulsars, which are rapidly rotating neutron stars, radio pulse periods enclosed in the range (0.03-4) s [9]. In X-ray pulsars which are binary stars where the first neutron star material flows from the second ordinary star, periods of pulses ranging from a few seconds to tens [9]. The first pulsars were discovered in 1967 (such as a radio pulsar CP 1919 with a period of pulsation of its directional radiation in 1.33 s) by astronomers at Cambridge University

(England) Anthony Hewish (born in 1924) with the assistance of his colleague Jocelyn Bell [20]. For this discovery E. Hewish was awarded the 1974 Nobel Prize in physics [2]. In 1991 R.A. Hulse and J.H. Taylor Jr. after 17 years of his careful astrophysical study of said continuously varying in sizes double pulsar, by measuring the declining orbit of the pair of amazing stars found confirmation of general relativity [2, 18]. In addition, in the course of this study the type of the binary pulsar PSR B1913+16, astronomers, these scientists were able to show that they have studied star system may emit gravitational waves [18, 20].



Fig. 10. General view of the unique radio telescope in Arecibo (set in a natural rock basin) managed by Cornell University and a member of the US National Centre for Astronomy and Ionosphere [20]

**5. Creation of neutron spectroscopy and neutron diffraction method.** The Nobel Prize in physics for 1994 was awarded to the Canadian experimental physicist Bertram Neville Brockhouse (Fig. 11) «for the creation of neutron spectroscopy» jointly and in equal shares with American experimental physicist Clifford Glenwood Shull (Fig. 12) «for the creation of the method of neutron diffraction» [21, 22]. Thorny scientific way for the native of a poor family B.N. Brockhouse has served as a volunteer in the Navy in Canada the entire period of the Second World War, it began with his admission in 1945 with the assistance of the Department of Veterans Support to the University of British Columbia [21]. In 1950, B.N. Brockhouse defended his Doctoral Thesis and begins to work in a scientific laboratory Chalk River engaged in the acquisition and use of nuclear energy. In 1955, B.N. Brockhouse together with its employees specializing in the field of neutron physics developed and produced a three-axis neutron spectrometer [21, 23]. After 10 years of fruitful work in the field of nuclear physics, he heads the Department of neutron physics in this large Canadian institution.

Talented Canadian physicist B.N. Brockhouse actually created a new trend in the field of neutron physics associated with the measurement of spectra of fast and slow neutrons and other elementary particles, including the quasi-particles (photons) [21, 23].

C.G. Shull after studying at the US Carnegie Institute of Technology in 1937 was connected to the

work of the research group at the Faculty of Physics, New York University in the field of nuclear physics [22]. Before he and his colleagues were given the task to create a high-voltage generator according to the known scheme Cockcroft-Walton [5] to accelerate deuterons D (nuclei of hydrogen isotopes - deuterium  ${}^2\text{H}$ ) to energy of 200 keV [22]. He participated in the first tests of the generator and the implementation with the help of the form of nuclear experiments D-D - reactions [24]. In 1941, C.G. Shull received the degree of Doctor of Philosophy. From 1946 he switches to the nuclear issue and moved to a secret area near the Tennessee River (United States) to work at the famous Oak Ridge National Laboratory [5, 22]. There he teamed up with the American physicist Ernest Vollan who died in 1984 and is therefore not share inherited C.G. Shull honor of presenting him in 1994 Nobel Prize, creates a simple two-axis spectrometer for neutron diffraction patterns of crystals and other materials [25].



Fig. 11. Prominent Canadian physicist Bertram Neville Brockhouse (1918-2003), Nobel Prize Laureate in physics for 1994



Fig. 12. Prominent American experimental physicist Clifford Glenwood Shull (1915-2001), Nobel Prize Laureate in physics for 1994

C.G. Shull is successfully studying neutron coherent scattering of many chemical elements from the periodic system of elements of D.I. Mendeleev [25]. He explores the dynamic diffraction and neutron waves spread in a variety of crystals. As a result of many years of fruitful work, C.G. Shull actually becomes the founder of structural neutron physics [2, 25]. It is considered to suppose that a time period that has elapsed since the creation in the field of neutron physics of neutron diffraction method to presenting the considered high scientific awards to C.G. Shull together with B.N. Brockhouse is yet the largest in the history of the Nobel Prizes [24].

#### REFERENCES

1. Zektser D.M. *Evrei – laureaty Nobelevskoj premii 1900-2013* [Jewries – Nobel laureates of 1900-2013]. Kharkiv, Printing-house «Madrid», 2014. 448 p. (Rus).
2. Khranov Yu.A. *Istoriia fiziki* [History of Physics]. Kiev, Feniks Publ., 2006. 1176 p. (Rus).
3. Available at: <http://www.biguniverse.ru/posts/nobelevskaya-premiya-po-fizike-2011> (accessed 01 May 2012). (Rus).
4. Curie E. *Mariya Kjuri* [Mariya Curie]. Moscow, Atomizdat Publ., 1979. 320 p. (Rus).
5. Baranov M.I. *Antologija vydaiushchikhsia dostizhenii v nauke i tekhnike: Monografija v 2-kh tomakh. Tom 1.* [An anthology of outstanding achievements in science and technology: Monographs in 2 vols. Vol.1]. Kharkov, NTMT Publ., 2011. 311 p. (Rus).
6. Available at: [http://www.peoples.ru/science/physics/jerome\\_friedman](http://www.peoples.ru/science/physics/jerome_friedman) (accessed 22 July 2014). (Rus).
7. Available at: [https://en.wikipedia.org/wiki/Henry\\_Way\\_Kendall](https://en.wikipedia.org/wiki/Henry_Way_Kendall) (accessed 15 September 2014).
8. Available at: <http://dic.academic.ru/dic.nsf/ruwiki/276481> (accessed 06 June 2015). (Rus).
9. *Bol'shoj illjustrirovannyj slovar' inostrannyh slov* [Large illustrated dictionary of foreign words]. Moscow, Russkie slovari Publ., 2004. 957 p. (Rus).
10. Kuz'michev V.E. *Zakony i formuly fiziki* [Laws and formulas of physics]. Kiev, Naukova Dumka Publ., 1989. 864 p. (Rus).
11. Available at: <http://pomnipro.ru/memorypage11618/biography> (accessed 10 May 2013). (Rus).
12. Available at: [https://en.wikipedia.org/wiki/Pierre-Gilles\\_de\\_Gennes](https://en.wikipedia.org/wiki/Pierre-Gilles_de_Gennes) (accessed 07 January 2014).
13. Gennes P.-G.-G. Myagkie veshchestva. *Uspekhi Fizicheskikh Nauk*, 1992, vol.162, no.9, pp. 125-132. (Rus). doi: 10.3367/ufnr.0162.199209c.0125.
14. Available at: [https://en.wikipedia.org/wiki/Georges\\_Charpak](https://en.wikipedia.org/wiki/Georges_Charpak) (accessed 12 November 2014).
15. Available at: [http://www.peoples.ru/science/physics/georges\\_sharpak](http://www.peoples.ru/science/physics/georges_sharpak) (accessed 18 September 2013). (Rus).
16. Available at: <http://www.profi-forex.org/wiki/george-shlapak.html> (accessed 23 May 2014). (Rus).
17. Available at: [http://obook.ru/биография?n=191783\\_халс-рассел-алан](http://obook.ru/биография?n=191783_халс-рассел-алан) (accessed 31 August 2012). (Rus).
18. Available at: <http://v-kosmose.com/velikie-astrofomiyi/dzhozef-teylor> (accessed 11 May 2010). (Rus).
19. Baranov M.I. *Antologija vydaiushchikhsia dostizhenii v nauke i tekhnike: Monografija v 2-kh tomakh. Tom 2.* [An anthology of outstanding achievements in science and technology: Monographs in 2 vols. Vol.2]. Kharkov, NTMT Publ., 2013. 333 p. (Rus).

20. Hulse R.A. Otkrytie dvoynogo pul'sara. *Uspekhi Fizicheskikh Nauk*, 1994, vol.164, iss.7, pp.743-756. (Rus). doi: **10.3367/ufnr.0164.199407d.0743**.

21. Available at: [http://www.peoples.ru/science/physics/bertram\\_neville\\_brockhouse](http://www.peoples.ru/science/physics/bertram_neville_brockhouse) (accessed 08 October 2012). (Rus).

22. Available at: [http://obook.ru/биография?n=202517\\_шалл-клиффорд](http://obook.ru/биография?n=202517_шалл-клиффорд) (accessed 15 February 2014). (Rus).

23. Brockhouse B.N. Spektroskopiya medlennykh neutronov i Velikii Atlas fizicheskogo mira. *Uspekhi Fizicheskikh Nauk*, 1995, vol.165, no.12, pp. 1381-1397. (Rus). doi: **10.3367/ufnr.0165.199512d.1381**.

24. Available at: <http://www.people.su/123480> (accessed 19 June 2012). (Rus).

25. Shull C.G. Rannee razvitie fiziki neitronnogo rasseyaniya. *Uspekhi Fizicheskikh Nauk*, 1995, vol.165, no.12, p. 1399-1402. (Rus). doi: **10.3367/ufnr.0165.199512e.1399**.

Received 23.02.2016

*M.I. Baranov, Doctor of Technical Science, Chief Researcher, Scientific-&-Research Planning-&-Design Institute «Molniya» National Technical University «Kharkiv Polytechnic Institute», 47, Shevchenko Str., Kharkiv, 61013, Ukraine, phone +38 057 7076841, e-mail: eft@kpi.kharkov.ua*

How to cite this article:

Baranov M.I. An anthology of the distinguished achievements in science and technique. Part 35: Nobel Prize Laureates in Physics for 1990-1994. *Electrical engineering & electromechanics*, 2016, no.6, pp. 3-8. doi: 10.20998/2074-272X.2016.6.01.

G.V. Kulinchenko, A.M. Maslennikov, V.A. Baguta

## RESEARCH OF DYNAMIC PARAMETERS OF THE ELECTRIC DRIVE ON THE BASIS OF ROLLING ROTOR MOTOR

*Purpose. Development and investigation of a dynamic model of electric drive on the base of the rolling rotor motor (RRM) which reflects the positioning of the actuator of the locking and regulating equipment in time. Methodology. Analytical description of electromagnetic and mechanical processes in the electric drive during the RRM shaft movement by using a system of differential equations. Numerical imitation modeling with the processes visualization in the Matlab environment of the RRM rotor displacement with mechanical load in time. Results. It is shown that the degree of influence of the value of the load inertia on the dynamics of the object obtained by the waveform changes the rotation angle of the rotor and motor speed in time. The degree of influence of the value of the electromagnetic time constant of the dynamics of the positioning of the actuator, and the nature of transients during acceleration and fixing position of the rotor with a predetermined moment of inertia for different values of inductance. The effect of the ratio of electromechanical and electromagnetic time constants of the nature of the transition processes accompanying jog mode angular displacement of the drive shaft on the base of RRM. Originality. The lack of technical means to ensure acceptable accuracy time measurement of angular displacement shaft of the actuator in jog mode offset by using a laser meter which gives the opportunity to assess the adequacy of the dynamic model of the RRM. Practical value. The results of investigations allow to create a tool for optimization of structural, technical and hardware and software solutions for the improvement and modernization of the projected electric locking and regulating equipment. The direction for improving the dynamics of the drive on the basis of RRM is indicated providing for an increase in its torque characteristics of the motor by reducing the influence of the parameters of transients. References 10, figures 9.*

*Key words: rolling rotor motor, time constant, positioning control, dynamics.*

*Анализируются динамические параметры электропривода на базе двигателя с катящимся ротором. Точность позиционирования такого мехатронного модуля обеспечивается в результате исследования факторов, определяющих электромеханическую и электромагнитную постоянные времени. Экспериментальная оценка времени переходного процесса при управлении позиционированием модуля позволяет исследовать влияние различных параметров электропривода на его динамику. Библи. 10, рис. 9.*

*Ключевые слова: двигатель с катящимся ротором, постоянная времени, контроля позиционирования, динамика.*

**Introduction.** A certain segment of the electric drive of valves is a mechatronic module combines the control system and executive of electric single-turn actuator (ESA) which consists of an asynchronous motor and gearbox. Tasks of improvement technical and economic performance of these modules require the search for alternative actuators, such as rolling rotor motors (RRM). Besides being able to combine the functions of the motor and the gearbox, which significantly improves the performance characteristics of the module, an additional advantage of the RRM is to achieve a predetermined starting torque at a relatively low starting current.

The main trend in the development of the RRM is to increase the power of these motors as their energy performance indicators are improved with an increase in motor power.

From the perspective of improving the RRM parameters used in the valves a decisive role in research play opportunities torque, which prevents violation of synchronous rotation and slippage of the rotor relative to the stator.

**Problem definition.** Defining the research aspects of dynamic parameters of trees and shrubs, we note that the methods and modeling techniques are determined by the specifics of the simulation object. Specific to the RRM which operates in the valve drive is a universal indicator of the dynamic that characterizes the performance - its response  $\Pi$  [1]:

$$\Pi = M_r^2 / J_r, \quad (1)$$

where  $M_r$  is the RRM torque;  $J_r$  is the RRM rotor moment of inertia.

Evaluation of the dynamic characteristics of the actuator can be made at the time of acceleration and the engine stops at a given position, given the resistance moment and the moment of inertia of the load on the shaft of the RRM.

Such a formulation of the problem is typical for the step [2], induction [3] and DC motors used in mechatronic systems [4].

Features of formation of RRM torque [1] are small angular displacement of the motor shaft at predetermined control actions, not allow the use of the mentioned approaches to assess the dynamic parameters of the electric drive on the basis of RRM in jog mode.

**The relevance of research** results from opportunities to increase torque RRM to values that are implemented in the ESA with the gearbox. This definition of the relevance of the benefit is due to the operating parameters of RRM on the parameters of ESA. The process of an adequate comparison data on the dynamics of the start-stop mode is inhibited imperfection of methods of assessing the dynamic parameters of the drive, especially with the random nature of the positioning valves (valve position control). Results of valves operating modes simulations make it possible to obtain data that are necessary for improving motor control algorithms based on RRM, as well as optimizing its design.

Known mathematical models of RRM based on the equations describing the electromagnetic processes of electric machines [6] allow to improve the design of trees

and shrubs on the analysis of the angular displacement of the rotor at high and low speeds in stationary modes.

At investigations of the influence of stator coils switching modes RRM its torque shown that in conditions of changing load [7] is its dynamic characteristics determine the operational capabilities of the transmitter in various fields. By selecting the settings of switching modes for RRM given design, the desired speed at different points of resistance on the motor shaft.

More effective to assess the dynamic parameters RRM seems a simulation model [8] in which As the result of solution of the equation

$$U(t) = \frac{\partial \Phi(i, v)}{\partial i} \frac{di}{dt} + \frac{\partial \Phi(i, v)}{\partial v} \frac{dv}{dt} + R \cdot i, \quad (2)$$

where  $U(t)$  is the supply voltage;  $i$  is the winding current;  $\Phi$  is the magnetic flux of the stator winding;  $R$  is the winding resistance;  $v$  is the rotor rotation angle, we can obtain electromagnetic torque values  $M_e$  depending on the rotation angle:

$$M_e(i, v) = \frac{\partial \int \Phi(i, v) di}{\partial v}. \quad (3)$$

The position of the rotor which is determined by the angle of rotation  $v$  is calculated by solving the equations of equilibrium of torque on the motor shaft, whose members include the moment of resistance of the rotor movement, the dynamic moment of resistance, depending on the moment of inertia of the rotor and the load. The resulting static electromagnetic torque of this model does not reflect the nature of the transients which accompany switching operation of the rotor movement and depend on the electromechanical parameters of electric drive.

**The goal of the work** is to develop and investigate the drive dynamic model based on RRM which reflects the positioning of the valve actuator mechanism in time.

In addition, the results of the work provided for the formation of the requirements for the hardware and software components of the electric drive control systems on the basis of the RRM which is a tool to optimize the parameters of valve.

DKR transition from synchronous to asynchronous mode depends on the ratio values of the frictional force and the component of force of unilateral magnetic attraction (FUMA) creating a movement of the rotor on the stator bore. In the transition of the RRM in asynchronous mode accompanied by a rotor slippage the task of retaining the executive valve mechanism is in position by the action of the moment of resistance on the drive shaft. In this case, the objective of research is to assess the feasibility of the required value of the electromagnetic torque RRM.

**Influence of magnetic properties of materials of RRM magnetic system on its dynamics.** Since RRM shaft movement occurs as a result of the magnetic field of the stator to the rotor, it is necessary to assess the effect on the electro-dynamic performance parameters RRM its mathematical model. This approach stems from the fact that the absence of mechanical load on the motor corresponds to the idle mode in which the slip does not occur.

Increase of the RRM torque as a necessary condition to improve its dynamic parameters, is focused on achieving the optimal proportions of electromagnetic parameters that characterize the operation modes of the RRM.

The motor torque depends on the angular position of the rotor relative to the stator field and the value corresponding to the angle of magnetic induction in the air gap of the RRM [9]:

$$B_\delta(\varphi) = \frac{2 \cdot F_\delta \cdot \mu_0}{\delta \cdot \text{ch}^n(\varphi)}, \quad (4)$$

where  $F_\delta$  is the MMF of the air gap in radial direction;  $\delta$  is the air gap;  $\varphi$  is the angular coordinate determining radial value of the air gap length;  $\text{ch}$  is hyperbolic cosine;  $n$  is the number depending on the motor design.

Analysis of changes in the values of magnetic induction in the air gap range by changing the angle of rotation of the rotor shows that the change in rotation of the rotor  $B_\delta$  induction are 6%. Accordingly, taking into account the non-linear nature of the FUMA depending on the angle of rotation of the rotor, it is possible to estimate the range of variation for the two extreme values of the angle of rotation.

Using the magnetization curve of the steel rotor (curve 3, Fig. 1) we can calculate the value of the magnetic induction in the air gap between the stator and the rotor, depending on the intensity of the magnetic field for the minimum (0.001 mm) and maximum (0.08 mm) air gap which in Fig. 1 are displayed by lines 1 and 2.

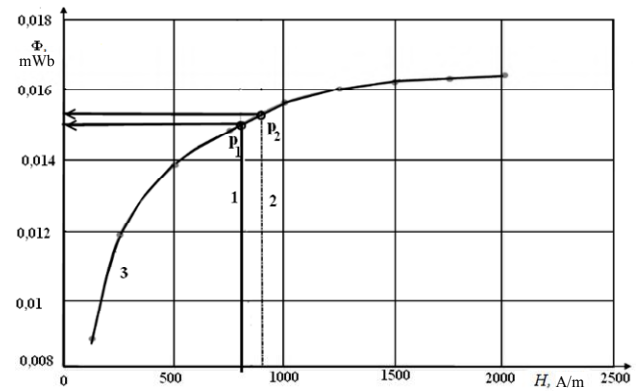


Fig. 1. Depending of the magnetic flux on the magnetic field strength

Two values of magnetic flux (points  $p_1$  and  $p_2$ ) corresponds to two values of magnetic flux  $\Phi_1 = 0.015$  mWb;  $\Phi_2 = 0.0155$  mWb and magnetic flux density  $B_1 = 1.515$  T;  $B_2 = 1.565$  T.

This fact, with sufficient accuracy for practical purposes, enables approximate function flux density in the air gap of the stator and the rotor of the linear dependence of the angle of rotation of the rotor.

The value of the magnetomotive force (MMF)  $F_\delta$  of the stator winding, which causes the value of magnetic induction in the air gap depends on the value of the stator current  $I$  flowing through the  $N$  turns of the coils of the stator winding. Since the coil current when applying a voltage pulse is changed according to the law:

$$I = \frac{U_p}{R_N} (1 - e^{-t/\tau}), \quad (5)$$

where  $U_p$  is the voltage on the winding terminals with resistance  $R_N$ ;  $\tau = L/R_N$  is the time constant;  $L$  is the coil inductance. Under this law, the rate of rise of EMF in the air gap, a change in magnetic flux and magnetic induction will be determined by the time constant which depends on the parameters of the stator winding.

Thus, the desire to increase the torque by increasing the RRM MMF is limited not only design considerations but also increase the inductance coil which together with the winding resistance time constant, and hence the dynamics RRM.

In [9] it is shown that the transition process in the stator winding of much longer rotor rolling, so the influence of electro-mechanical time constant of the process dynamics can be neglected. However, increasing the mass of the rotor, and respectively, its moment of inertia  $J_r$  which is essential for powerful engines disregard electro-mechanical time constant leads to errors in the estimates of the dynamic characteristics of the RRM.

The factors affecting the modes of RRM you should pay attention to the ratio of the electrical and electromechanical time constants, with time winding switching, since these parameters, together with the rotor friction regulate the mode change RRM from synchronous to asynchronous mode or slippage.

**Formalization of the mathematical model of the RRM.** Formulating objectives DKR simulations that determine the structure of the model, we take into account the fact that the investigated object is used in the composition of the gas throttling mechatronic module. This means that in addition to the requirement value of torque and holding torque pipeline throttle position, engine real part of a module must provide the necessary speed and positioning accuracy, that is, the proper control action pickup. Accordingly, model RRM should reflect the connection of said parameters from the control channels.

Specificity of functioning throttle module is the time change in the nature and direction of the mechanical stress. Therefore, developing a model should reflect the speed and mechanical characteristics in different modes of operation of the actuator based on the RRM.

Since the processes occurring in any motor, influence each other, for the study of dynamic modes mechatronic module is necessary to consider the relationship of energy balance equations and electromagnetic torque with the equations of motion of the components of the module. As a result of solving these equations numerically obtained time dependence, reflecting the dynamics of the process of functioning of the module with the RRM. Application of numerical modeling techniques is due to the nonlinear character of the equations describing the state of the trees and shrubs.

The structure of the model mechatronic module based RRM present scheme consisting of 4 blocks:

- block emulation movement of the magnetic field of the stator (BEFS);
- logic block (LB);
- emulation block of  $B_\delta$  magnetic flux density in the air gap of the stator and rotor (BEMI);
- mechanical block (MB).

*Mechanical block* of the model, in accordance with traditional approaches to describing movement, can be represented by the following equations:

$$\frac{d}{dt} \omega_r = \frac{1}{J_m} (T_e - T_f); \quad (6) \quad \frac{d}{dt} \varphi = \omega_r, \quad (7)$$

where  $\omega_r$  is the rotor rotation angular frequency;  $J_m$  is the total reduced moment of inertia of the rotor and the load;  $T_e$ ,  $T_f$  are the electromagnetic torque and the moment of resistance to rotation;  $\varphi$  is the rolling angle of the rotor relative to the stator field.

In the environment of MATLAB Simulink simulation corresponds to a block diagram shown in Fig. 2 corresponds to (7).

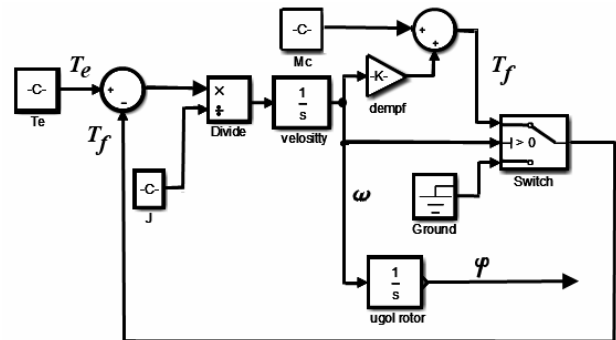


Fig. 2. Block diagram of the modeling MB

A feature of modeling MB RRM is a reflection of fixing the rotor position as a result of the voltage pulse off applied to the stator coil. At the time when the electromagnetic torque  $T_e = 0$  but continues to operate the time  $T_f$  resistance, the rolling speed of the rotor begins to decline. After the rotor speed reaches zero, the circuit pattern using the element MB *Switch* deactivated the moment of resistance.

As can be seen from Fig. 2, in the membrane via the damping factor is taken into account the time dependence of the resistance on the rotor speed.

The *block of emulation of magnetic flux density  $B_\delta$*  reflects the change in the value of the magnetic flux density in the air gap of the stator and rotor rolling. These changes are described by (4).

Work BEMI synchronized switching pulse generator motion control circuit RRM. As a result of applying a voltage pulse in the windings of the stator coils RRM, the current MMF and forming the magnetic induction in the air gap varies exponentially (5). Model changes can represent aperiodic link with a time constant  $\tau$  winding. Actually, it is this constant corresponds to the electromagnetic time constant of the RRM.

For the time varying magnetic flux density values, take into consideration the magnitude of the air gap, which also changes periodically as a result of movement of the rotor. Calculations are performed in the gap  $\delta$  by linear interpolation of  $\delta$  depending on the load angle  $\Theta$  which is connected to the rotor rotation angle  $\varphi$ . BEMI simulation diagram is shown in Fig. 3.

*Emulation block of motion vector of the stator magnetic field* displays discrete changes of the magnetic field vector angle in accordance with a frequency set by external switching pulse generator.

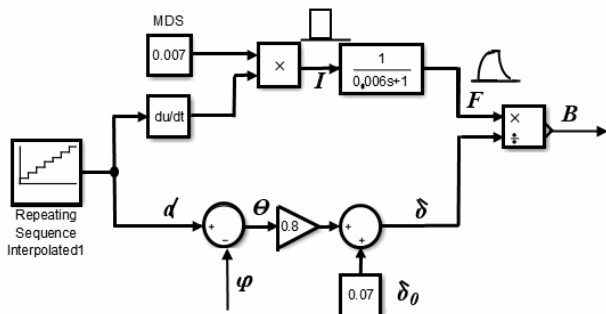


Fig. 3. BEMI diagram

In accordance with the switching rules 8 stator coil RRM angle displacement vector of the magnetic field of the stator is  $\alpha = \pi/4$ . For the rotor in one direction or another *switching pulse generator* (Fig. 3, 4) generates signals which effect movement provides discrete induction vector at an angle  $\alpha = \pi/4$ . Violation of balance of forces acting on the rotor caused by switching the coils of the stator winding sets it in motion, resulting in a change of the current position of the rotor angle  $\varphi$  with the changes and load angle  $\Theta = (\alpha - \varphi)$ .

Electromagnetic RRM time dynamic model by moving the magnetic induction vector associated with the load angle  $\Theta$  calculated by [1]:

$$T_e(\Theta) = \frac{B_{\delta}^2 \cdot S \cdot d_r}{2\mu_0} \cdot \sin \Theta, \quad (8)$$

where  $S$  is the surface area through which the main magnetic flux;  $d_r$  is the rotor diameter.

As a result, the time can create electromagnetic simulation RRM circuit shown in Fig. 4.

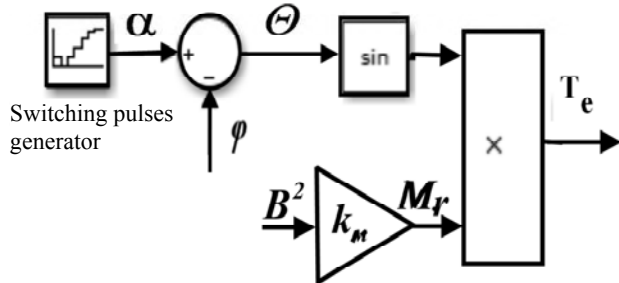


Fig. 4. Diagram of the RM electromagnetic torque modeling

Since the objective of the simulation is to study the dynamics of the parameters of the RRM, the results of modeling should reflect the interaction of acceleration and deceleration processes of the rotor over time. Characteristic of these processes is a change in velocity and acceleration values of the rotor not only in time but also in direction. The logic of the relationships of parameters and ranges of restrictions are implemented in the *logic block (LB)*. LB model allows reflect the direction of rotation of the rotor switch RRM and to exclude the value of the model parameters, which are contrary to the physical meaning of the engine operation. These problems are solved by a combination of logic functions simulation environment Matlab.

LB Interaction with other blocks of the model is reflected in the overall block diagram of the dynamic model RRM shown in Fig. 5.

The input parameters of the model are given by the characteristics of the RRM and the parameters of mechatronic module of valve. The simulation results are obtained in the form of time-varying output dynamic model parameters - the torque and rotational speed of the rotor angle RRM.

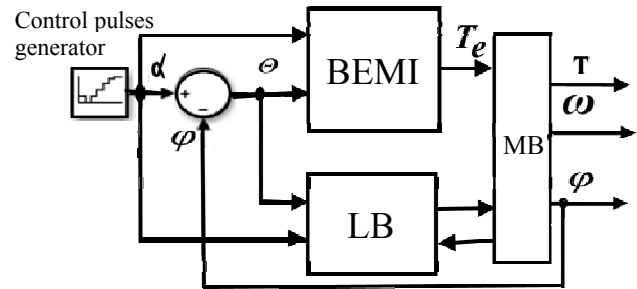


Fig. 5. Block diagram of the RRM dynamic model

These changes are the output parameters are visualized using Matlab user interface environment. The nature of the perturbation modeling object parameter is defined on the basis of the simulation tasks.

**The simulation results.** Exploring the value of the degree of influence of the dynamic moment of inertia of the object, received waveform changes the angle of rotation, trees and shrubs of the rotor speed with time for various values of the moment of inertia  $J_m$  (Fig. 6).

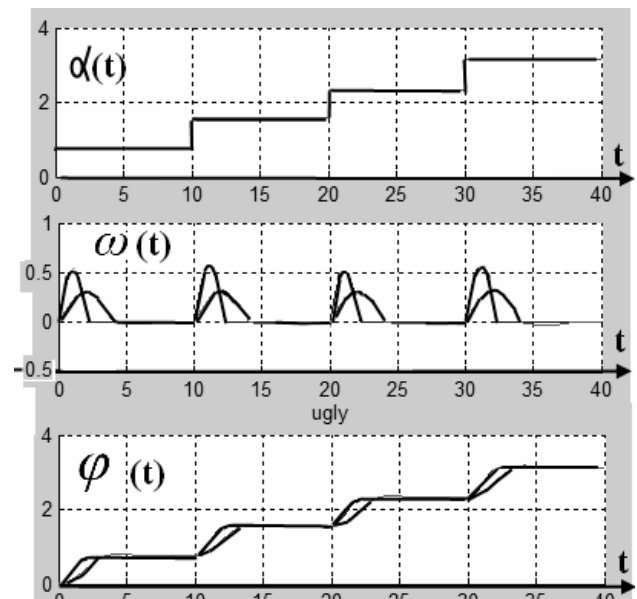


Fig. 6. Waveforms of changes the angular velocity and the angle of rotation of the rotor windings during commutation

Fig. 7,a shows the changes in the angle of rotation of the induction vector control, Fig. 7,b - electromagnetic torque  $T_e$  fluctuations Fig. 7,c - the angular speed variation, Fig. 7,d - the angle of rotation of the rotor for different values of the load torque. From these data it follows that increasing the time constant of the module due to the shaft torque load up to a certain value, it is necessary to limit the switching frequency of the windings. Fig. 7,c,d is evident that under certain loads on the shaft of the RRM control rotor motion is meaningless because there is no fixation of the rotor in the previous position.

To assess the impact of the value of the electromagnetic time constant of the dynamics of the positioning of trees and shrubs, consider the nature of the transients during acceleration and fixing position of the rotor with a predetermined moment of inertia for different inductance values (Fig. 8).

In relative terms in Fig. 8, *a* shows the variation of the electromagnetic moment in time; *b* - the resultant moment, *c* - change of angular velocity, *d* - the angle of rotation of the rotor to the winding time constant  $\tau = 5$  ms and  $\tau = 50$  ms.

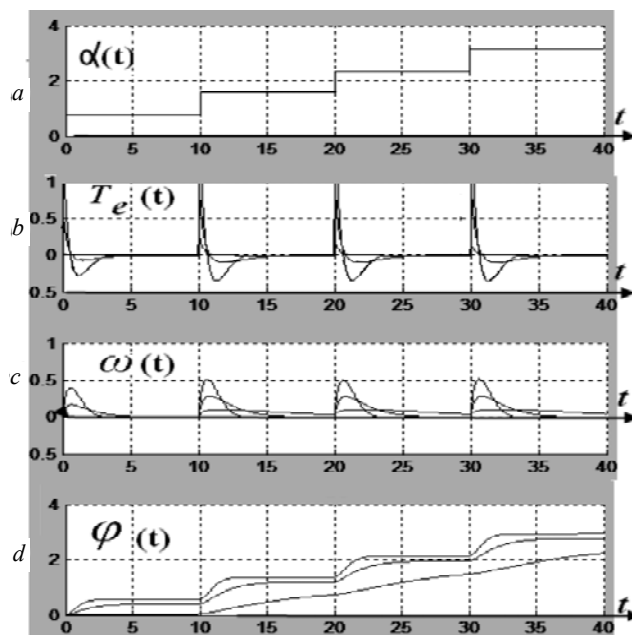


Fig. 7. Waveforms of changes of the torque, the rotor speed angle and rotation angle

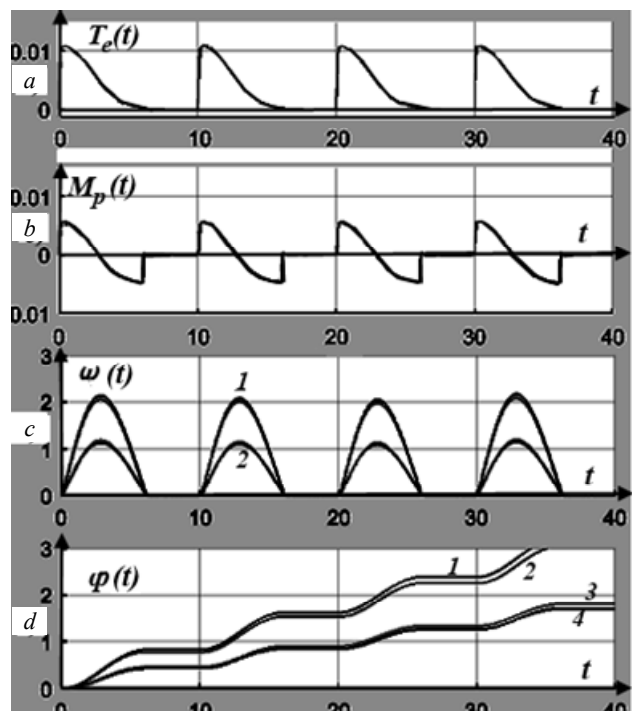


Fig 8. Waveforms of changes of electromagnetic torque, angular velocity and the angle of rotation of the rotor

The curves 1, 2 on the waveform 8, *d* correspond to a change in the angle of rotation for the inertial torque  $J_{m1}$ , and curves 3 and 4 - for the moment of inertia  $J_{m2}$ .

The values of angular velocity for a moment of inertia  $J_{m1}$  (curve 1) and  $J_{m2}$  (curve 2) in Fig. 8 differ appreciably, while, as a result of the difference signals changes inductance value on the order of ( $\tau = 5$  ms,  $\tau = 50$  ms) unobtrusive.

It should be noted that an increase in inductance of RRM more 500 mH (which is no practical necessity) also degrades engine dynamics, particularly in the starting torque / braking.

From the transient analysis implementations obtained shows that the positioning control device of valve in which RRM are used, should be developed taking into account the ratio of electromechanical and electromagnetic electromechanical time constants valve drive. Despite the fact that the value of the inductance of the stator winding in MMF electrical state significantly affects the formation of MDS stator winding RRM increasing the electromechanical constant as a result of increased mechanical load increases the transient driving, up to a loss of accuracy of positioning of the shaft.

To assess the adequacy of the dynamic model RRM used experimental setup diagram is shown in Fig. 9.

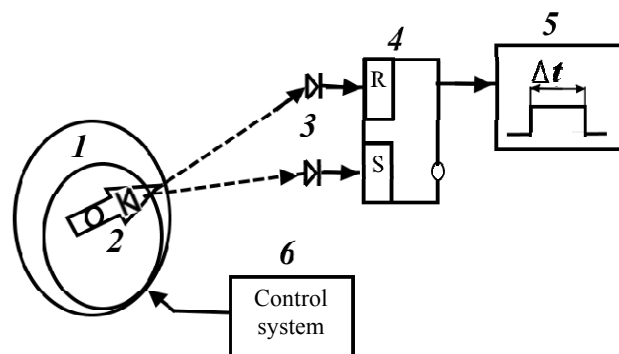


Fig. 9. Diagram of the change of duration of the RRM shaft displacement on the given angle

On the SSR shaft 1 laser emitter 2 is mounted the movement of the beam is perceived laser photodetectors 3. When moving the laser beam, the locking position of the shaft RRM through radiation photodetectors state is changed by trigger 4. Use measuring time intervals 5, which serves as a storage oscilloscope RIGOL SDS 1022DL, estimated travel time from one shaft RRM position to another.

This time clearly depends on the time of the transient change of the rotor position. The values of angular displacement are determined by the coefficient of reduction of the RRM, respectively, RRM design features. The need to use the laser measuring instrument is the difficulty of measuring small values of angular shaft displacements RRM feeding unit of the switching pulse.

With the help of the described installation (Fig. 9) to assess the impact of different windings switching modes RRM on the nature of transient electric [10] is carried out. The results of the time correction of the transition process, which takes into account the ratio of the electrical and electromechanical time constants, indicate the possibility

of improving the dynamic parameters of the drive and increase its torque. Continued use of the results of modeling the dynamics of jog mode electric drive on the basis of the RRM opens the possibility of using energy-efficient control algorithms.

**Conclusions.** A dynamic model of the electric drive on the basis RRM reflecting the positioning of the drive shaft at the time taking into account the influence of the valve parameters on the parameters transients is developed.

Data obtained as a result of the simulation provide an opportunity to formulate the requirements for the hardware and software components of the electric drive control system based on the RRM.

Experimental evaluation of the time of transients in the management of valve positioning modules allow us to state that the improvement of the electric drive on the basis of the dynamics of RRM aimed at increasing its torque, it is advisable to carry out on the basis of hardware and software systems that provide reducing the influence of the characteristics of RRM on the parameters of transients.

#### REFERENCES

1. Nanij V.V., Miroshnichenko A.G., Juhimchuk V.D. Egorov A.V., Dunev A.A., Maslennikov A.M., Pototskiy D.V. Aspects of the design and testing of engines with a rolling rotor. *Bulletin of NTU «KhPI». Series: Problems of electrical machines and apparatus perfection. The theory and practice*, 2010, no.55, pp. 84-88. (Rus).
2. Sokolov A.V. Dynamic models of stepper motors. *Bulletin of the South Ural State University*, 2012, no.16, pp. 116-119. (Rus).
3. Palpankar P.M., Ghanmare R.U., Makade N. A generalized dynamic model of induction motor using Simulink. *ITSI Transactions on Electrical and Electronics Engineering*, 2013, Vol.1, Iss.5, pp. 118-122.
4. Farhan A. Salem. Dynamic modeling, simulation and control of electric machines for mechatronics applications. *International journal of control, automation and systems*, 2013, Vol.1, no.2, pp. 30-42.

#### How to cite this article:

Kulinchenko G.V., Maslennikov A.M., Baguta V.A. Research of dynamic parameters of the electric drive on the basis of rolling rotor motor. *Electrical engineering & electromechanics*, 2016, no.6, pp. 9-14. doi: 10.20998/2074-272X.2016.6.02.

5. Eyhab E.-K. Design and analysis of rolled rotor switched reluctance motor. *Journal of Electrical Engineering & Technology*, 2006, Vol.1, No.4, pp. 472-481. doi: 10.5370/jeet.2006.1.4.472.

6. Bock U. A novel approach of modeling SR motor systems. *ICEM 2002. 15th International Conference on Electrical Machines*. Bruges, Belgium. 2002. p. 338.

7. Ungureanu C., Rata M., Graur A. PLC control of an electromechanical converter with rolling rotor and axial air-gap. *ACTA Electrotehnica*, 2015, Vol.56, No.4, pp. 137-142.

8. Arkkio A., Biernat A., Bucki B., Kaminski G., Smak A., Staszewski P. Simulation model and laboratory test of switched reluctance motor with rolling rotor. *Prace Naukowe Instytutu Maszyn, Napędów i Pomiarów Elektrycznych Politechniki Wrocławskiej*, 2008, no.28, pp. 52-57.

9. Nanij V.V., Lykah V.A., Maslennikov A.M. Rotor motion in the rolling-rotor electrical machine. *Transactions of Kremenchuk Mykhailo Ostrohradskyi National University*, 2014, no.3(86), pp. 9-13. (Rus).

10. Baguta V. A., Kulinchenko G. V. Evaluation of characteristics of mechatronic module based on a stepper motor. *Bulletin of NTU «KhPI». Series: Problems of electrical machines and apparatus perfection. The theory and practice*, 2013, no.51(1024), pp.43-53. (Rus).

Received 10.09.2016

G.V. Kulinchenko<sup>1</sup>, Candidate of Technical Science, Associate Professor,

A.M. Maslennikov<sup>2</sup>, Candidate of Technical Science, Associate Professor,

V.A. Baguta<sup>1</sup>, Engineer,

<sup>1</sup> Sumy State University,

2, Rymyskogo-Korsakova Str., Sumy, 40007, Ukraine,

e-mail: heorhy@yandex.ua, viktrbaguta@gmail.com

<sup>2</sup> National Technical University «Kharkiv Polytechnic Institute»,

21, Kyrpychova Str., Kharkiv, 61002, Ukraine,

e-mail: x-maslennikov@yandex.ua

A.V. Matyuschenko

## ANALYSIS OF THERMAL STATE OF TRACTION BRUSHLESS PERMANENT MOTOR FOR MINE ELECTRIC LOCOMOTIVE

**Purpose.** The study was conducted to analyze thermal state of the traction permanent magnet synchronous motor for mine electric battery locomotive when operating in continuous and short-time duty modes. These operating modes are selected for study, as they are typical for mine electric locomotives. **Methodology.** Thermal calculation was performed by means of FEM in three-dimensional formulation of problem using Jmag-Designer. **Results.** The modeling results of thermal state of the PMSM in continuous and short-time duty operation modes showed good agreement with experimental results. The results showed that the temperature of PM is higher than temperature of the stator winding in continuous operation mode. It was found that PM temperature might reach excessive values because of the high presence of eddy current losses in neodymium PM. Therefore, special attention in the design and testing of PMSM should be paid to the temperature of PM in various operation modes. **Practical value.** It was recommended to use high temperature permanent magnets in traction PMSM to avoid demagnetization of PM and performance degradation. References 7, tables 2, figures 10.

**Key words:** brushless motor, heat generation, temperature, losses, permanent magnet, coil, current, resistance, mathematical model, FEM.

*Выполнен поверочный тепловой расчет тягового вентильного двигателя с постоянными магнитами посредством конечно-элементной цепно-полевой математической модели на платформе JMAG-Designer в трехмерной постановке задачи. Получено распределение температуры и графики нагрева деталей двигателя. Проведен сравнительный анализ расчетных и экспериментальных данных теплового состояния двигателя в часовом и длительном режимах работы. Библ. 7, табл. 2, рис. 10.*

**Ключевые слова:** вентильный двигатель, нагрев, температура, потери, постоянный магнит (ПМ), катушка, математическая модель, метод конечных элементов.

**Introduction.** It is known that the traction motors for mine locomotives are experiencing high electromagnetic and thermal loads in difficult environments for different operating modes. This imposes certain requirements for performance since, cooling system and materials used in the engine to provide desired performance. Therefore, an important objective in the design of the traction brushless motor with permanent magnets (BMPM) is an evaluation of its thermal state which provides information on the duration of the motor operation at various modes and, if necessary, adjusts the design to ensure that the necessary requirements met [1-4].

In [5] the results of «Electrical Engineering - New Technologies» LLC (Odessa) is presented to develop and test BMPM for a mine locomotive. Overheating of the stator windings were noted during continuous operation of the BMPM as a part of the laden locomotive weight of 70.5 tons. This load corresponds to the BMPM hour mode of operation.

**The goal of the paper** is control thermal calculation and analysis of the thermal state of the traction BMPM [5] for mine electric battery locomotive when operating in hour and long-term modes. This analysis serves as a basis for recommendations to improve the design of the traction BMPM.

**Object of investigations** is the traction BMPM for a mine battery electric locomotive designed by the «Electrical Engineering - New Technologies» LLC the design of which is shown in Fig. 1. Basic geometric dimensions and winding data of BMPM are presented in Table 1. Parameters of studied operation modes are presented in Table 2.

**Method of investigations.** The most detailed and accurate picture of the temperature distribution it is possible to obtain by numerical methods based on the Finite Element Method. These methods make it possible to per-

form the thermal calculation of the steady or transient mode of heat exchange process in the three-dimensional formulation of the problem and determine the temperature of any part of the motor [3, 4].

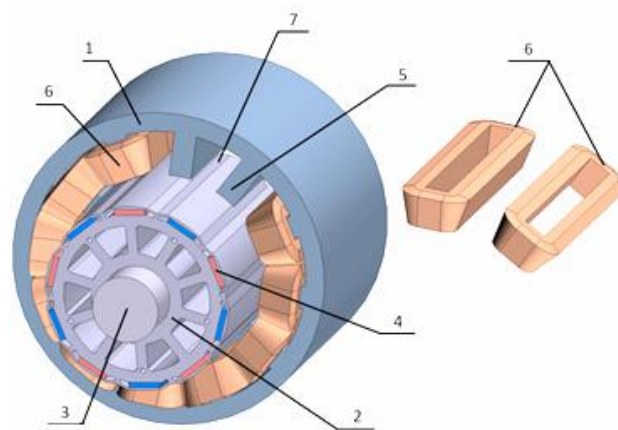


Fig. 1. Salient-pole BMPM with concentrated stator winding: 1 – stator; 2 – rotor; 3 – shaft; 4 – PM; 5 – stator pole; 6 – stator winding coils; 7 – stator slot

We present control thermal calculation of the considered BMPM in the software package for numerical computations Jmag-Designer as well as the analysis and comparison of the calculated and experimental data.

The first step of the thermal calculation is to develop a BMPM 3D model which is to be detailed enough to adequately describe the structure and properties of BMPM than should include not only the active part but the housing, shaft and slot insulation.

Table 1  
Geometrical dimensions and winding data of the motor

| Name                                | Value        |
|-------------------------------------|--------------|
| Stator external diameter, mm        | 360          |
| Stator internal diameter, mm        | 217          |
| Number of teeth of stator,          | 12           |
| Active part length, mm              | 240          |
| Number of poles of rotor            | 10           |
| Number of stator winding coil turns | 10           |
| Dimensions of magnets (NdFeB), mm   | 240×35.5×6.3 |
| Air gap, mm                         | 2.5          |

Table 2  
Parameters of the BMPM operation modes

| Mode                | Torque, N·n | Rotation frequency, RPM | Consumption current, A | Feeding voltage, V |
|---------------------|-------------|-------------------------|------------------------|--------------------|
| Hour                | 210         | 600                     | 130                    | 120                |
| Long-term (2 hours) | 100         | 760                     | 70                     | 120                |

Fig. 2 shows the prepared for calculations 3D model of the BMPM. Its parts are modeled in such a way that their sizes were close to real. It should be noted that the shape of the housing parts and the shaft is simplified but their volume equal to the real volume of parts of the BMPM investigated. This simplification allows to reduce the time spent on the creation of a 3D model at retaining the basic structure's properties for thermal calculation.

The second step is to determine the electric and magnetic losses in the motor parts. For this electromagnetic calculation of the BMPM at hour and long-term modes has been made modes taking into account losses due to eddy currents in the steel and PM.

To account the losses due to eddy currents, rotor stator and PM have been assigned the appropriate electrical resistivity.

To perform the electromagnetic calculation to the stator winding coils (SW) of the field model of the BMPM in JMAG-Designer chains editor we connected electrical circuit consisting of a constant voltage source, an inverter with pulse width modulation, voltmeters and ammeters (Fig. 3). Inverter keys control is performed using a model that implements vector BMPM control [6].

As the initial data of operation modes of the BMPM model we set voltage, rotation speed and load torque.

As a result of the electromagnetic calculation BMPM data were obtained on the losses in the stator, rotor, SW coils and PM. Loss calculation results are shown in Fig. 4 and Fig. 5.

From Fig. 4 and Fig. 5 one can see that the ratio of losses in the SW coils and PM is different for the investigated modes of the BMPM operation. At the long-term operation mode losses in PM are greater than the losses in the SW.

The third stage is proper calculation of the thermal state of the BMPM where we calculate transient motor heating process at the investigated operation modes.

For the calculation of each part corresponding heat capacity and thermal conductivity was appointed. On the

outer surface of the housing the boundary condition (the 3rd kind) of the heat transfer was set with the heat transfer coefficient of  $12 \text{ W/m}^2 \cdot ^\circ\text{C}$  which is the average for natural convective cooling of similar motors' structures under normal conditions [7].

For each part, which is a heating source we set losses calculated earlier. Furthermore, at the calculation the dependence of electrical losses in SW on temperature has been accounted.

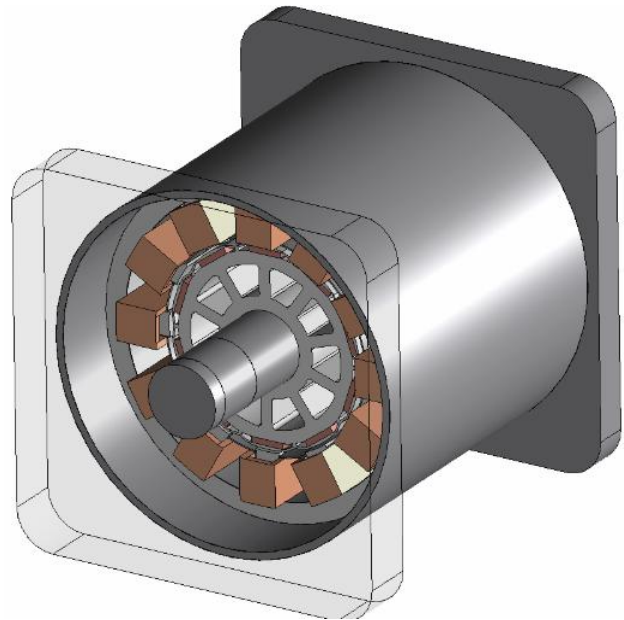


Fig. 2. 3D BMPM model with simplified housing

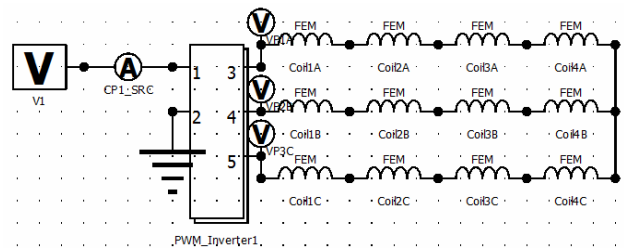


Fig. 3. Electrical circuit of the circuit-field BMPM model

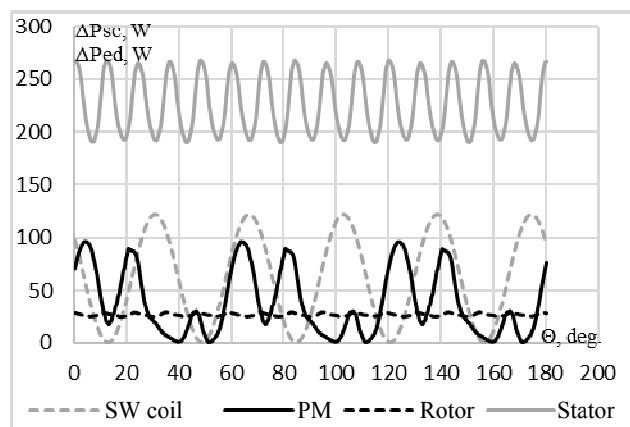


Fig. 4. Electrical ( $\Delta P_{sc}$ ) and magnetic ( $\Delta P_{ed}$ ) losses in the BMPM (hour mode)

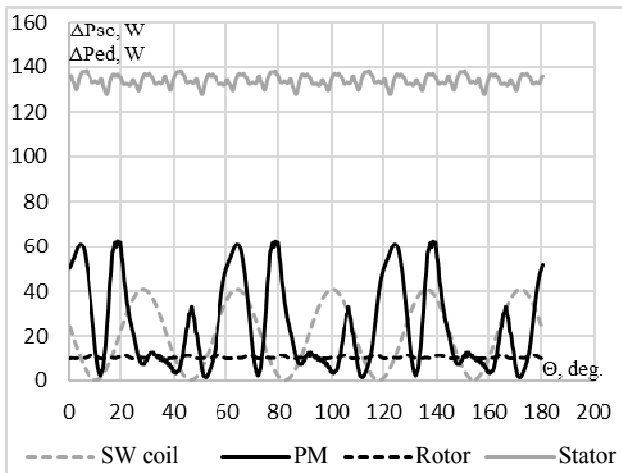


Fig. 5. Electrical ( $\Delta P_{sc}$ ) and magnetic ( $\Delta P_{ed}$ ) losses in the BMPM (long-term mode)

### Results of investigations.

Fig. 6, 7 show the results of thermal calculation as the temperature distribution and heat flux vector for the hour operation mode of the BMPM. It is evident that the heat generated by the rotor and PM is removed through the stator, and the heat of SW coils is removed through the stator and housing to the environment. This distribution of the heat flow is typical for such electric motors, which indicates the correct formulation of the problem.

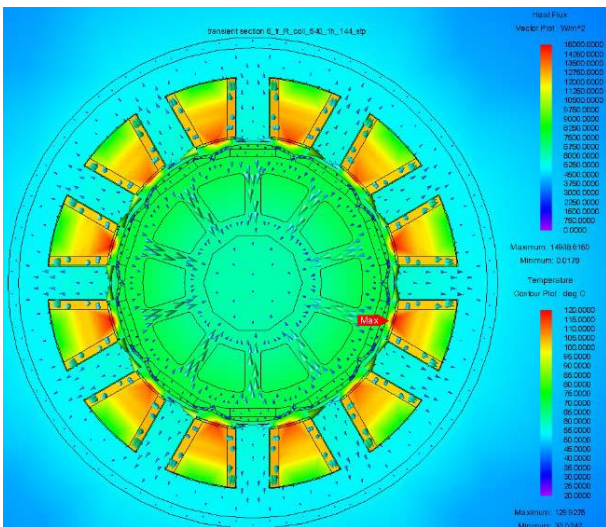


Fig. 6. Temperature and heat flux distributions (BMPM cross-section)

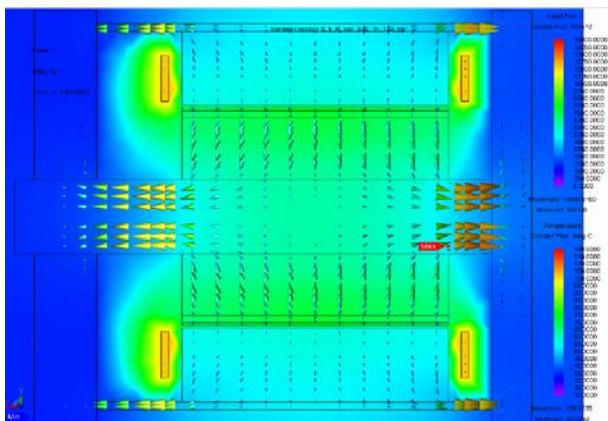


Fig. 7. Temperature and heat flux distributions (BMPM longitudinal section)

Fig. 8 compares the experimental and computational graphics of BMPM coil heating at the hour and long-term operation modes. BMPM tests were carried out on the stand of the «Energy» [5] Company.

Fig. 8 shows good agreement between the results of calculation and experiment for long-term operation. In this case the difference between the calculation and experiment does not exceed 9 %.

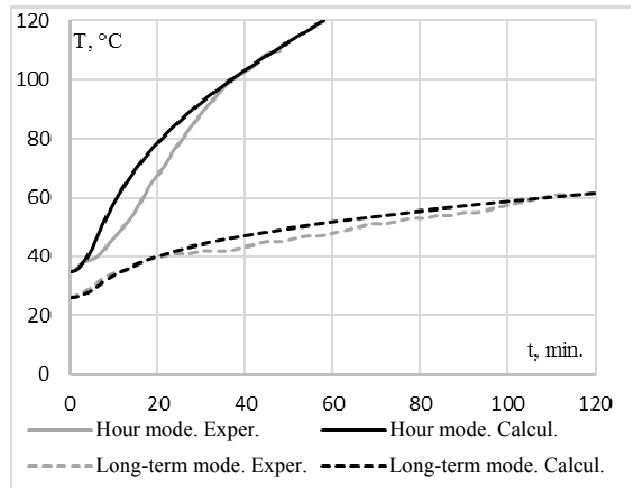


Fig. 8. SW coils heating at hour and long-term operation modes

As a result of the experiment, it was found that in 47th minutes of operation at the hour mode of the BMPM the overheating protection tripped. In this case the winding temperature reaches 110 °C. This fact is also confirmed by the results of calculation. The maximum difference between calculation and experiment is 25 %. This difference can be explained by the uneven load on the duration of the experiment.

Fig. 9, 10 shows graphs of heating of the BMPM components in the hour and long-term operation. It is evident that the process of heating is different at these modes. For example, the temperature of the PM at the long-term operation during most of the estimated time exceeds the temperature of the SW coils. This can be explained by the fact that at the long-term mode, the current consumption is smaller and the rotation rate is greater than at the hour mode. As is known, the value of the magnetic losses is proportional to the frequency of magnetic reversal, and the value of the electric losses is proportional to the square of the current.

It should also be noted that at the hour operation mode the PM temperature reached 82 °C which exceeds the maximum permissible operating temperature of the low-temperature neodymium PM. Therefore, in order to avoid losing the properties of the PM and worsening performance for the investigated BMPM it is recommended to use PM with operating temperature of 120 °C and higher.

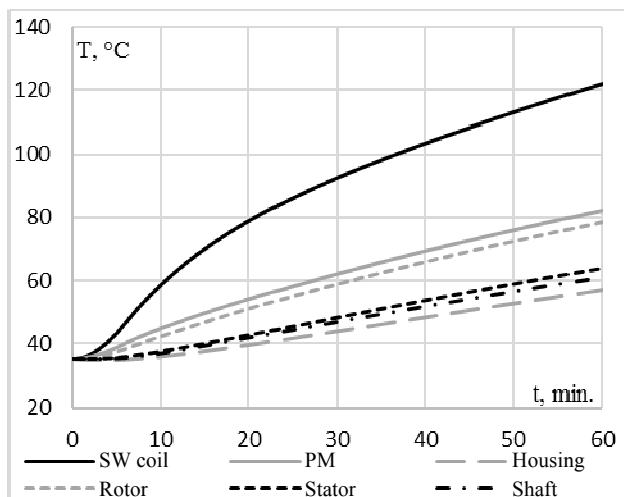


Fig. 9. BMPM parts heating (hour mode)

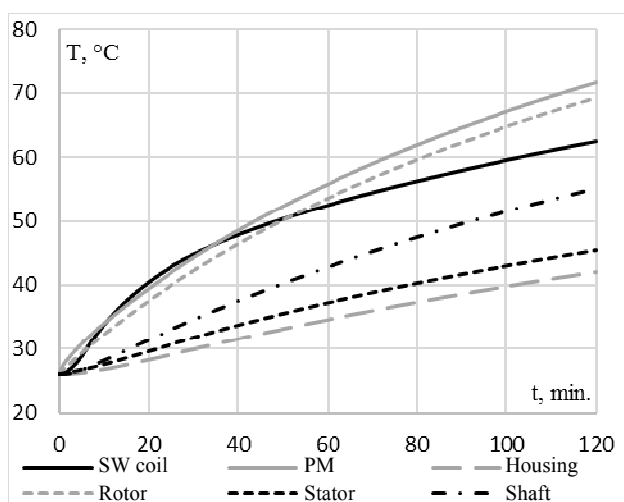


Fig. 10. BMPM parts heating (long-term mode)

### Conclusions.

1. The results of the modeling of the thermal state of the BMPM at hour and long-term operation modes shown good agreement with experimental results. The difference between the calculations and experiments for the long-term mode does not exceed 9 %, and the maximum divergence of the calculated results and the experiment for the hour mode is 25 %.

### How to cite this article:

Matyushenko A.V. Analysis of thermal state of traction brushless permanent motor for mine electric locomotive. *Electrical engineering & electromechanics*, 2016, no.6, pp. 15-18. doi: 10.20998/2074-272X.2016.6.03.

2. As a result of calculations it was determined that the PM temperature may reach high values because of the presence in the PM significant eddy current losses. Therefore, special attention in the design and testing of the BMPM should be paid to the temperature of the PM at various operation modes.

### REFERENCES

1. Lee S.-T., Kim H.-J., Cho J.-H., Joo D.-S., Kim D.-K. Thermal Analysis of Interior Permanent-Magnet Synchronous Motor by Electromagnetic Field-Thermal Linked Analysis. *Journal of Electrical Engineering and Technology*, Nov.2012, vol.7, no.6, pp. 905-910. doi: 10.5370/jeet.2012.7.6.905.
2. Mynarek P., Kowol M. Thermal analysis of a PMSM using fea and lumped parameter modeling. *Czasopismo Techniczne*, 2015, no.1-E(8), pp. 97-107. doi: 10.4467/2353737XCT.15.031.3831.
3. Chin Y.K., Staton D.A. Transient thermal analysis using both lumped-circuit approach and finite element method of a permanent magnet traction motor. *2004 IEEE Africon. 7th Africon Conference in Africa (IEEE Cat. No.04CH37590)*. doi: 10.1109/africon.2004.1406847.
4. Kefalas T.D., Kladas A.G. Finite element transient thermal analysis of PMSM for aerospace applications. *XXth International Conference on Electrical Machines, Sep. 2012*. doi: 10.1109/icelmach.2012.6350246.
5. Rimsha V.V., Radimov I.N., Guliy M.V., Matyushenko A.V. Brushless motor for mining battery-electric locomotive. *Electrotechnic and computer systems*, 2016, vol.22(98), pp. 134-138. (Rus).
6. Matyushenko A.V. Calculation of characteristics of permanent magnet synchronous motor and their comparative analysis. *Electrotechnic and computer systems*, 2015, vol.19(95), pp. 101-105. (Rus).
7. Borisenko A.I. *Ohlazhdenie promyshlennykh jelektricheskikh mashin* [Cooling of industrial electric machinery]. Moscow, Energoatomizdat Publ., 1983. 296 p. (Rus).

Received 07.10.2016

A.V. Matyushenko, Postgraduate Student,  
Odessa National Polytechnic University,  
1, Shevchenko Avenue, Odessa, 65044, Ukraine,  
e-mail: sparkam@rambler.ru

V.I. Milykh

## A TURBO-GENERATOR DESIGN SYNTHESIS BASED ON THE NUMERICAL-FIELD CALCULATIONS AT VARYING THE NUMBER OF STATOR SLOTS

*Purpose.* The work is dedicated to the presentation of the principle of construction and implementation of an automated synthesis system of the turbo-generator (TG) electromagnetic system in the case of its modernization. This is done on the example of changing the number of the stator core slots. *Methodology.* The basis of the synthesis is a TG basic construction. Its structure includes the mathematical and physical-geometrical models, as well as the calculation model for the FEMM software environment, providing the numerical calculations of the magnetic fields and electromagnetic parameters of TG. The mathematical model links the changing and basic dimensions and parameters of the electromagnetic system, provided that the TG power parameters are ensured. The physical-geometrical model is the geometric mapping of the electromagnetic system with the specified physical properties of its elements. This model converts the TG electromagnetic system in a calculation model for the FEMM program. *Results.* Testing of the created synthesis system is carried out on the example of the 340 MW TG. The geometric, electromagnetic and power parameters of its basic construction and its new variants at the different numbers of the stator slots are compared. The harmonic analysis of the temporal function of the stator winding EMF is also made for the variants being compared. *Originality.* The mathematical model, relating the new and base parameters of TG at the changing of the number of the stator slots is created. A Lua script, providing the numerical-field calculations of the TG electromagnetic parameters in the FEMM software environment is worked out. Construction of the constructive and calculation models, the numerical-field calculations and delivery of results are performed by a computer automatically, that ensures high efficiency of the TG design process. *Practical value.* The considered version of the TG modernization on the example of changing the number of the stator core slots provided an opportunity for the presentation of the principle of construction and implementation of design synthesis system. For the practical use in the TG designing process, the developed and presented system can be more detailed with specifying the individual components of the mathematical model and expanded for varying other parameters of TG and optimizing its design. References 11, tables 2, figures 7.

**Key words:** turbo-generator, modernization, design synthesis, mathematical model, Lua script, FEMM program, numerical-field calculations, electromagnetic parameters.

*Представлен пример проектного синтеза электромагнитной системы турбогенератора (ТГ) при его модернизации. Создана математическая модель, связывающая новые и базовые параметры ТГ при изменении числа пазов статора. Разработан скрипт Lua, обеспечивающий численно-полевые расчеты электромагнитных параметров ТГ в программной среде FEMM. Построение конструктивной и расчетной моделей, численно-полевые расчеты и выдача результатов выполняются компьютером автоматически, что обеспечивает высокую эффективность процесса проектирования ТГ. Аprobация системы синтеза проведена на примере ТГ мощностью 340 МВт. Библи. 11, табл. 2, рис. 7.*

**Ключевые слова:** турбогенератор, модернизация, проектный синтез, математическая модель, скрипт Lua, программа FEMM, численно-полевые расчеты, электромагнитные параметры.

**Introduction.** Powerful turbo-generators (TG) are the most complicated, expensive and effective in operation electric machines [1]. Design and the subsequent creation of new models take months and even years.

Therefore, the process of improving the TG is often reduced to modernize their samples after long test operation [2]. At the same time seeking to improve the parameters of the TG with minimum changes as the global innovations in the complex can lead to unpredictable consequences and require long experimental refinement which requires large capital investments.

One option to speed up the modernization of TG is reduction of terms of computational and design works. They require a significant amount of time due to the complexity of classical methods of calculation as such because of the complexity of TG themselves. These methods are often adapted to specific design elements of standard sizes and need to be improved after their changes.

Numerical methods for calculating magnetic fields [3, 4] coupled with high-speed computers and efficient software provide new opportunities for improving the design system of the TG. This contributed to the novelty of the results provided, as an example of created on this basis an automated design synthesis system of the TG electromagnetic system in the case of their modernization

at the change of certain key elements of the design is considered.

**The goal of the work.** The work is dedicated to the presentation of the principle of construction and implementation of an automated system of electromagnetic TG system synthesis in the case of its modernization that is being done on the example of changing the number of slots of the stator core.

Structure of synthesis is based on the basic design of the TG available and includes a mathematical model, a physical and geometrical model, a calculation model in conjunction with the program environment FEMM [5] which provides the numerical calculations of the magnetic field and electromagnetic parameters of the TG. The mathematical model relates the changing sizes and parameters of the electromagnetic system with its basic dimensions and parameters with the condition for the output power parameters of the TG. Physical and geometric model is a geometric mapping of the electromagnetic system with given properties of its components - the windings and cores. This model converts the electromagnetic system of the TG and the results of the mathematical model operation to the calculation model for the FEMM program.

Creation of the physical and geometric model, its transformation into a calculation model, providing the FEMM program operation, the definition of the electromagnetic and power parameters based on numerical calculation of the magnetic field, output results of the synthesis of the updated TG electromagnetic system to a text file - all is done automatically by the control program written in the Lua language integrated in the FEMM [5].

Universalism of created models of available and developed software is that they are adapted to the typical structural shapes of TG as a whole and their elements. Numerical methods for the calculation of the magnetic field remove restrictions on the account of real constructive shapes of electric machines as a whole and their elements, on account of the magnetic saturation.

Largely developed software is based on investigations that have presented earlier in papers by the author [4, 6-10] and others.

**Object of investigations.** Demonstration of calculation results is carried out on a three-phase TG [2] the basic electromagnetic system of which is shown in Fig. 1. It has a rated: power  $P_N=340$  MW; phase voltage  $U_{sN}=11547$  V and current  $I_{sN}=11547$  A; power factor  $\cos\phi_{sN}=0.85$ ; frequency  $f_s=50$  Hz. Its number of pole pairs  $p=1$ ; active length  $l_a=5.308$  m; non-magnetic gap  $\delta=77.5$  mm; radius of the rotor surface  $r_{re}=0.56$  m; number of turns of its phase winding  $N_s=10$ , relative shortening  $\beta_s=0.8$ ; number of effective conductors of the stator winding rod  $N_{cs}=1$ ; number of turns of the rotor winding  $N_r=126$ .

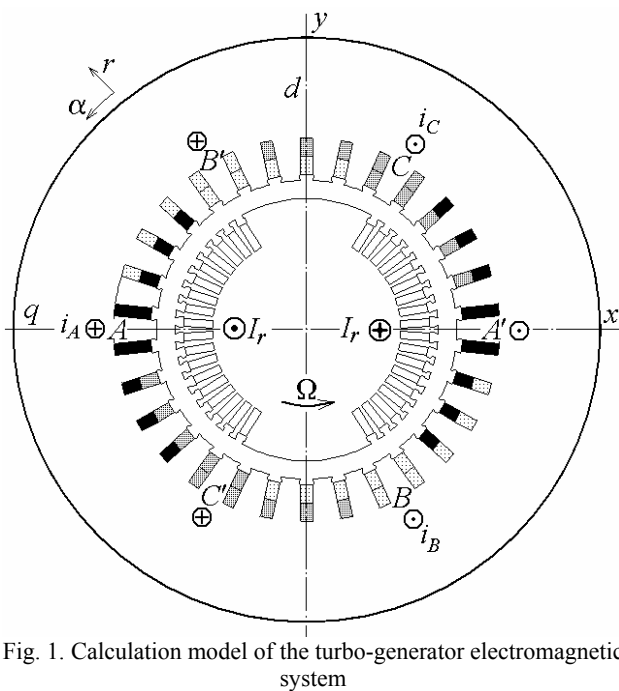


Fig. 1. Calculation model of the turbo-generator electromagnetic system

**The basic values of the TG conserved in its modernization.** Fig. 2 shows the TG structure with the indication of main dimensions of the cores of the stator and rotor. Taking into account the decisive role in the formation of the magnetic fields of the tooth-slot stator structure, it is shown by fragments with required dimensions marked in Fig. 3.

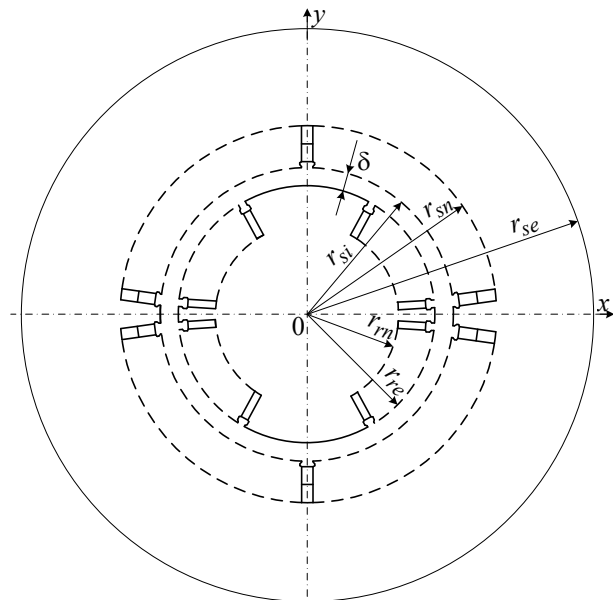


Fig. 2. Geometrical model of the turbo-generator

In order to in visualized form evaluate changes in the TG at the change of the number of stator slots, the presented TG output parameters are reserved: power, phase voltage and current, power factor. Also given in the long history of the TG design values of magnetic field strength in the gap, teeth and the back of the stator core as well as a gap characterized for the TG of corresponding power level are conserved.

Assuming the continuation of the stator current and the distributed current density in the conductors of its winding, sections of its rods must be preserved. Since the stator winding voltage is conserved, the insulating gaps in the slot are conserved, too (Fig. 3).

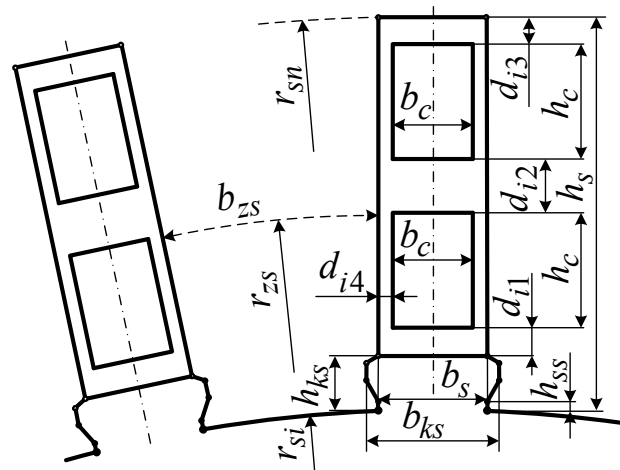


Fig. 3. Tooth-slot structure of the stator

When conserving the TG voltage, EMF of the phase stator winding should be conserved, too

$$E_s = \pi\sqrt{2} \cdot f_s \cdot N_s \cdot \Phi_s \cdot K_{ws}, \quad (1)$$

where  $\Phi_s$  is the magnetic flux in the gap;  $K_{ws}$  is the stator winding factor.

For convenience, hereinafter we refer to the same indications of the same base and new values but for the first ones the letter  $b$  in the indexes is added everywhere.

Stator rods are characterized by their height  $h_c$  and width  $b_c$ , the surrounding insulation in the slots – by thicknesses  $d_{i1}$ ,  $d_{i2}$ ,  $d_{i3}$  and  $d_{i4}$ . In the basic design of the cross-sectional area of the stator winding rod  $S_{cb}=h_{cb} \cdot b_{cb}$ . Taking into account the conditions set, at varying of  $h_c$  and  $b_c$  the following must be provided:  $h_c \cdot b_c = S_{cb}$ .

This variation accompanies the change in the size of the stator slots - their height  $h_s$  and width  $b_s$ . Here, we must preserve the height of the spline  $h_{ss}$  and the depth of the wedge  $h_{ks}$  as well as two-way wedge recess in the wall of the slot  $d_{ks} = b_{ksb} - b_{sb}$ . The width of the grooves under the wedge should change and be  $d_{ks} = b_{ksb} - b_{sb}$ .

Note that in the basic design the following conditions must be satisfied:  $b_c = b_s - 2d_{i4}$ ;  $h_c = (h_s - d_{hs})/2$ , where the constant addition by the height of the stator slot

$$d_{hs} = h_{ks} + d_{i1} + d_{i2} + d_{i3}.$$

### Mathematical model of the TG electromagnetic system synthesis.

First of all, we consider what changes need to occur in the stator and its slot and when the number of its slots is changed from the base value  $Q_{sb}$  to the new one  $Q_s$  which will be characterized by the coefficient of change in the number of stator slots:

$$k_{Qs} = Q_s / Q_{sb}. \quad (2)$$

We assume that the ratio of number of turns of the winding of the stator core of the base and the new design corresponds to the ratio of slots, i.e.  $N_s = k_{Qs} N_{sb}$ .

Then, from the condition of conservation of the EMF of the phase stator winding (1), the new value of the magnetic flux in the pole pitch  $\Phi_s = \Phi_{sb} / k_{Qs}$ .

By the magnetic flux, the magnetic flux density in the gap to the bore of the stator core (in this case, the average value) is determined

$$B_\delta = \frac{\Phi_s}{\tau_p \cdot l_a}, \quad (3)$$

where we know the expression of the pole pitch on the radius of the stator bore  $r_{si}$ :

$$\tau_p = \frac{\pi \cdot r_{si}}{p}. \quad (4)$$

As already stated, the value of  $B_\delta$  should remain as one of the fundamental quantities of TG and other electric machines.

The expression (3) includes two values, which, in principle, can be changed to conserve in the TG the previous value  $B_\delta$ , namely, the active length  $l_a$  and the radius of the stator bore  $r_{si}$ .

In this paper we restrict ourselves to the second option - to change the radius of the stator bore  $r_{si}$  as more complicated in the analysis. Active length  $l_a$  is preserved such it was in the TG basic design.

*Modernization of the TG electromagnetic system with changing the radius of the bore of the stator core.* From a combination of the above relations a new value of this radius is obtained

$$r_{si} = r_{sib} / k_{Qs}. \quad (5)$$

To preserve the value of the magnetic flux density in the teeth of the stator core with the new number of slots, respectively the total width of the teeth changes

$$b_{zss} = b_{zssb} / k_{Qs}, \quad (6)$$

Basic total width of all the stator teeth in their average radius of location  $r_{zsb}$  (Fig. 3)

$$b_{zssb} = 2 \cdot \pi \cdot r_{zsb} - b_{sb} \cdot Q_{sb}, \quad (7)$$

where  $r_{zsb} = r_{sib} + h_{sb}/2$ ;  $r_{sib}$  is the radius of the bore of the stator core;  $h_{sb}$  is its slot height.

With the new value of the radius  $r_{si}$  by (5), we carry out a number of preparatory transformations of TG stator parameters for the new number of its teeth  $Q_s$  in order to obtain the new value of the average radius of stator teeth  $r_{zs}$ , and then the other quantities.

The width of the new slot at the new value  $Q_s$

$$b_s = \frac{2 \cdot \pi \cdot r_{zs} - b_{zss}}{Q_s}. \quad (8)$$

The width and height of the stator winding rod

$$b_c = b_s - 2 \cdot d_{i4}; \quad h_c = S_{cb} / b_c. \quad (9)$$

The height of the slot

$$h_s = 2 h_c + d_{hs}. \quad (10)$$

For expressing the average radius of the tooth-slot structure we make substitutions based on relationships of written values above:

$$\begin{aligned} r_{zs} &= r_{si} + h_s/2 = r_{si} + (2 h_c + d_{hs})/2 = r_{si} + h_c + d_{hs}/2 = \\ &= r_{si} + S_{cb}/b_c + d_{hs}/2 = r_{si} + S_{cb}/(b_s - 2 d_{i4}) + d_{hs}/2 = \\ &= r_{si} + \frac{S_{cb}}{2 \cdot \pi \cdot r_{zs} - b_{zss} - 2 \cdot d_{i4}} + \frac{d_{hs}}{2} = e + \frac{Q_s \cdot S_{cb}}{2 \cdot \pi \cdot r_{zs} - d}, \end{aligned}$$

where the notations are introduced for brevity  $d = b_{zss} + 2 \cdot d_{i4} \cdot Q_s$ ;  $e = (r_{si} + d_{hs}/2)$ .

In fact, an equation is obtained from which, after incremental transformations we obtain the quadratic equation with respect to  $r_{zs}$ :

$$r_{zs}^2 - r_{zs} [d/(2 \cdot \pi) + e] + [d e - S_{cb} \cdot Q_s] / (2 \cdot \pi) = 0. \quad (11)$$

Its solution gives two roots, the meaning of which has an option with a plus sign before the radical:

$$r_{zs} = -\frac{b}{2} \pm \sqrt{\frac{b^2}{4} - c}, \quad (12)$$

where  $b = -e - d / (2 \cdot \pi)$ ;  $c = (d \cdot e - S_{cb} \cdot Q_s) / (2 \cdot \pi)$ .

After obtaining  $r_{zs}$  we determine for the new TG design values  $b_s$ ,  $b_c$ ,  $h_c$ ,  $h_s$  by (8)-(10).

Besides, we obtain the new values of the width of the stator wedge

$$b_{ks} = b_s + d_{ks}, \quad (13)$$

stator core backrest height

$$h_{as} = h_{asb} / k_{Qs}, \quad (14)$$

outer radius of the stator core

$$r_{se} = r_{si} + h_s + h_{as} \quad (15)$$

number of serial turns of the two-layer stator windings is verified

$$N_s = N_{cs} \cdot Q_s / m_s, \quad (16)$$

where  $N_{cs}$  is the number of effective conductors in the rod;  $m_s$  is the number of TG phases.

In the process of calculating TG electromagnetic parameters we use stator phase winding active resistance  $R_s = R_{sb} \cdot k_{Qs}$  and reactance of frontal scattering  $X_v = X_{vb} \cdot k_{Qs}^2$  [4, 7] which are recalculated for the changes in the number of turns (16) by the same quanti-

ties of the basic model.

With the change of the radius of the bore of the stator core it is necessary to correct the rotor structure (Fig. 2). In this regard, we consider two options: retaining and changing its dimensions of its slots which are separately designated in Fig. 4.

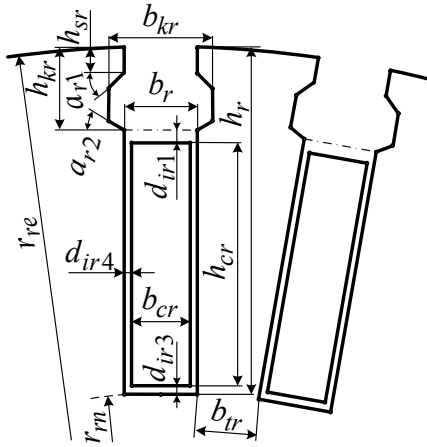


Fig. 4. Tooth-slot structure of the rotor

*Correction of the rotor with maintaining its slots dimensions.* With the new value of the radius of the bore of the stator core, the new radius of the rotor surface

$$r_{re} = r_{si} - \delta. \quad (17)$$

Therefore, correction of the number of rotor slots is need so as not to reduce the critical values of a rotor core - the width of the base of the rotor teeth

$$b_{tr} = \frac{2 \cdot \pi \cdot r_{rm} - b_r}{Q_{ru}} - b_r, \quad (18)$$

where  $Q_{ru}$  is the conditionally total number of rotor slots;  $b_r$  is the rotor slot width;  $r_{rm} = r_{re} - h_r$ , is the location radius of the rotor teeth base (Fig. 4).

When choosing the number of actual rotor slots  $Q_r$  we conserve about the filling ratio of the rotor surface by the slots

$$k_{Qr} = Q_r / Q_{ru}. \quad (19)$$

By these formulas (18), (19) for the base version of the TG we must take basic values  $Q_{rub}$ ,  $Q_{rb}$ ,  $b_{rb}$ ,  $h_{rb}$ , and then we obtain the values of the parameters  $k_{Qrb}$ ,  $b_{trb}$  which further by varying the rotor sizes should be about conserved.

To transform the rotor design the following formulas are used.

New conditionally total number of rotor slots

$$Q_{ru} = 4 \cdot \text{ceil} \left( \frac{0,5 \cdot \pi \cdot r_{rm} - 0,99}{b_{rb} + b_{trb}} \right), \quad (20)$$

where the symbol *ceil* means rounded to the nearest whole number in the direction of greater value of the argument in parentheses.

The new number of coiled rotor slots

$$Q_r = 4 \cdot \text{ceil} (0,25 \cdot Q_{ru} \cdot k_{Qrb} - 0,99). \quad (21)$$

Number of serial turns of the rotor winding

$$N_r = N_{cr} \cdot Q_r / 2, \quad (22)$$

where  $N_{cr}$  is the number of effective conductors in the rotor slot, for the base variant it was  $N_{crb} = 2 N_{rb} / Q_{rb}$ .

*Correction of the rotor with a change in its slots dimensions.* For more detailed correction of the rotor design we can change the basic dimensions of its slot (Fig. 4).

At the correction of the rotor we conserve:

- cross-sectional area of the rotor winding rod

$$S_{crb} = h_{crb} \cdot b_{crb}; \quad (23)$$

where  $h_{crb}$ ,  $b_{crb}$  are the height and width of its winding rod;

- insulation gaps in the slot  $d_{ir1}$ ,  $d_{ir3}$  and  $d_{ir4}$ , height of the wedge with spline  $h_{kr}$ ;

- constant addition to the height of the rotor rod

$$d_{hr} = h_{kr} + d_{ir1} + d_{ir3}; \quad (24)$$

- two-side wedge deepening to the slot wall  $d_{kr} = b_{kr} - b_{rb}$ , where  $b_{rb}$  is the width of the rotor base slot;

- width of the base of the rotor teeth  $b_{trb}$  (18);

- base filling factor of the surface of the rotor slots  $k_{Qrb}$  determined by (19).

To keep the magnetic flux density in the base of the rotor teeth at the change of the number of stator slots, we change the radius of the location of the bottom of rotor slots proportionally to the magnetic flux change

$$r_{rm} = r_{rnb} / k_{Qs}. \quad (25)$$

By formulas (21) and (22) we calculate values  $Q_{ru}$  and  $Q_r$ .

Keeping base value  $b_{trb}$  calculated by the formula like (18) we obtain new rotor slot width

$$b_r = \frac{2 \cdot \pi \cdot r_{rm} - b_{trb}}{Q_{ru}} - b_{trb}. \quad (26)$$

New values of rotor rod dimensions

$$b_{cr} = b_r - 2 \cdot d_{ir4}; \quad h_{cr} = S_{crb} / b_{cr}. \quad (27)$$

New values of the slot height and width in the area under the wedge recess

$$h_r = h_{cr} + d_{hr}; \quad b_{kr} = b_r + d_{kr}. \quad (28)$$

The radii of the rotor surface and the stator core bore

$$r_{re} = r_{rm} + h_r; \quad r_{si} = r_{re} + \delta. \quad (29)$$

Taking into account this new value of the radius  $r_{si}$  after that by (12) we calculate  $r_{zs}$  for the new number of its teeth  $Q_s$  and then other new values  $h_s$ ,  $b_s$ ,  $h_c$ ,  $b_s$  by the above formulas (12), (8) - (10) as well as the new values of the stator wedge width

$$b_{ks} = b_s + d_{ks}, \quad (30)$$

outer radius of the stator core

$$r_{se} = r_{si} + h_s + h_{as}. \quad (31)$$

As a result as before, the corresponding geometric model of the TG is formed

The presented set of formulas from (2) to (31) together with intermediate formulas and is a mathematical model of the TG electromagnetic system synthesis at the changing the number of its stator slots.

**The structure of an automated synthesis system of the TG electromagnetic system.** The basis for the use of a mathematical model, as stated above, are the parameters of the TG basic design and the new value of the number of stator slots. Since then the automated program complex synthesis of a new TG electromagnetic system synthesis begins. A block diagram of the synthesis program is shown in Fig. 5.

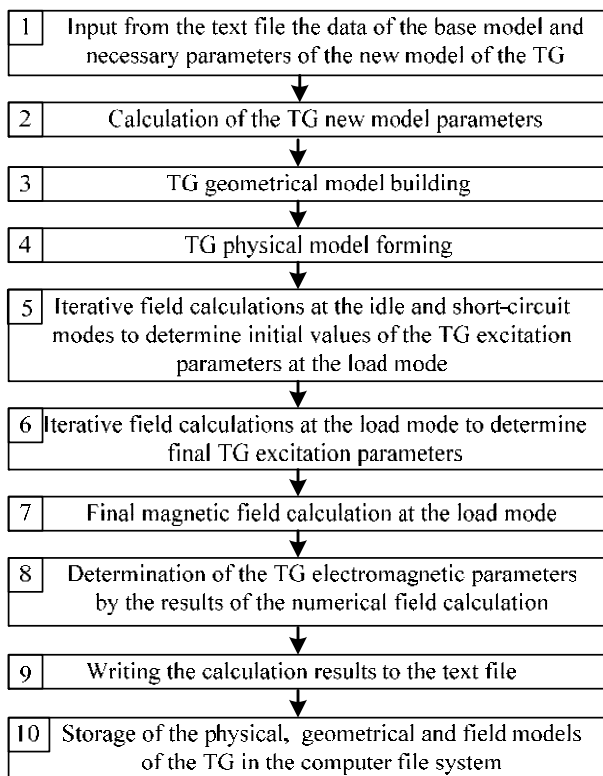


Fig. 5. A block diagram of the program for the TG electromagnetic system synthesis

All steps shown in Fig. 5 are organized and executed by the program written on the algorithmic language Lua-script. The program starts and runs in the FEMM software environment [5] performing numerical calculation of the magnetic field by the finite element method.

The meaning of the blocks 1, 2, 7, 8, 9 and 10 in Fig. 5, in principle, obvious by given in these texts. However, for the remaining blocks we give explanations.

The essence and software implementation of the blocks 3 and 4 are presented in [9]. In them on the base of the input and calculated information on the geometrical dimensions of TG the geometrical model of the TG is built as shown in Fig. 2, Fig. 3 and Fig. 4. For the parts of this model magnetic and current properties are defined - a physical model is formed. And in general a physical and geometric model of the TG for the magnetic field in the software environment FEMM is obtained.

Power parameters of the TG are set by values of power, phase voltage and current, power factor. And to achieve them in each new version of the TG we need to know the parameters of the excitation of the magnetic field at the load mode. These parameters include excitation current in the rotor winding  $I_r$  and phase shift  $\beta$  of the stator winding EMF relative to the rotor windings EMF.

Theory and principle of their determination are described in [7] and they are based on iterative calculations of magnetic fields at the idle, short-circuit and the load modes. All this is done in blocks 5 and 6 (Fig. 5), and software implementation is presented in [10]. Besides, in them necessary electromagnetic parameters of the TG are determined that corresponds to the block 8 in Fig. 5 in which also harmonic analysis of the angle function of the magnetic flux linkage the temporal function of EMF of

the phase stator winding in accordance with the theory presented in [8] is carried out.

#### Results of operation of the software complex for the TG electromagnetic system synthesis.

First of all, the developed software system has been tested on the base model with the number of TG stator slots  $Q_{sb}=30$ . That is based on the basic model, the same one is synthesized. Next, the synthesis of new models with slot numbers  $Q_s$  equal to 24 and 36 has been carried out. They are closest to basic model minimal and greater values of  $Q_s$  taking into account that

$$Q_s = 2 \cdot p \cdot m_s \cdot q_s, \quad (32)$$

where the number of slots per pole and phase  $q_s$  must be an integer.

Step of the stator winding by slots  $y_s$  is calculated in the program on the condition of ensuring the coefficient of relative shortening  $\beta_s$  nearest or equal to 0.833 which gives the most suitable harmonic structure of the stator winding EMF [1].

Each of the TG models with their values  $Q_s$  is synthesized in two considered above rotor correction variants: 1) while maintaining its slot dimensions; 2) changing them. Further number of these options added to the values of the numbers of stator slots.

It should be noted that the calculation of one variant on a computer of sufficiently high level taken about 10 minutes, with the number of nodes of the finite element structure according to the variant was 30-40 thousand, the number of triangles 60-80 thousand.

A geometrical model of the TG base variant was already presented in Fig. 1 and is repeated in Fig. 6 together with the calculated magnetic field distribution. Models of synthesized electromagnetic systems are shown in Fig. 7 – each one by fourth cross-section with the corresponding parts of the picture of the magnetic field at the load mode.

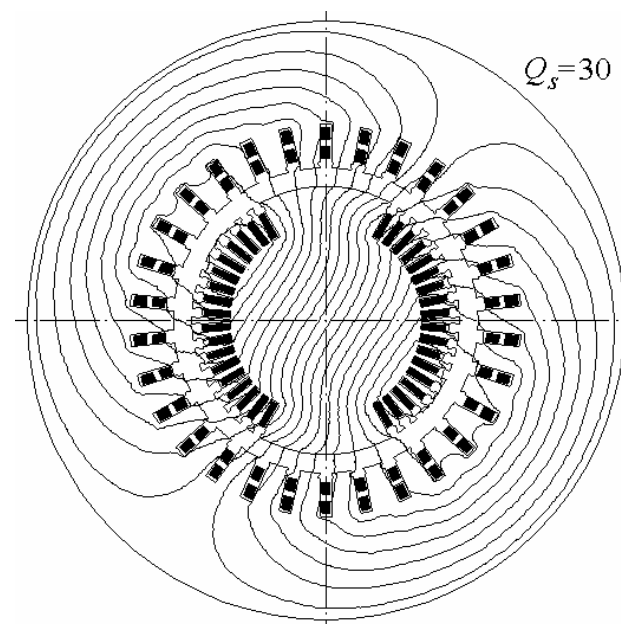


Fig. 6. Base electromagnetic system of the TG

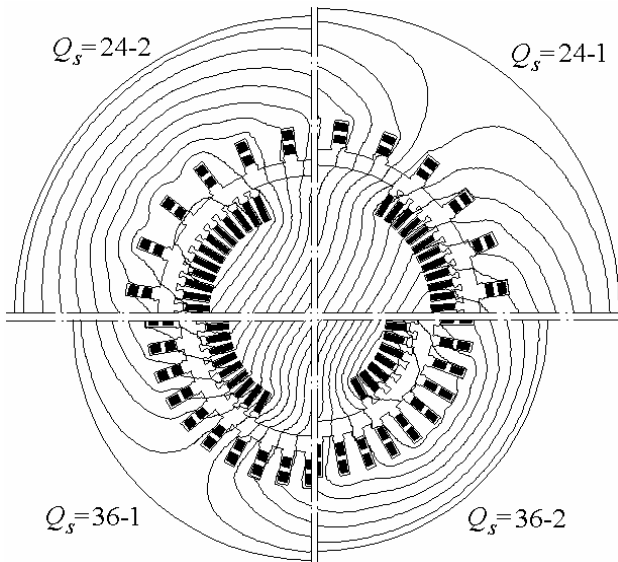


Fig. 7. Variants of the TG electromagnetic system

In the numeric form part of information about these models is presented in Table 1.

Table 1  
Parameters of the TG electromagnetic system in various its variants

| $Q_s$                | 24-1    | 24-2    | 30      | 36-1    | 36-2    |
|----------------------|---------|---------|---------|---------|---------|
| $y_s$                | 10      | 10      | 12      | 15      | 15      |
| $\beta_s$            | 0.833   | 0.833   | 0.8     | 0.833   | 0.833   |
| $Q_r$                | 48      | 48      | 36      | 36      | 36      |
| $N_r$                | 168     | 168     | 126     | 126     | 98      |
| $N_s$                | 8       | 8       | 10      | 12      | 12      |
| $r_{s1}$ , mm        | 797     | 749     | 637.5   | 637.50  | 570     |
| $r_{s2}$ , mm        | 1482    | 1451    | 1250    | 1167    | 1126    |
| $h_s$ , mm           | 148     | 165     | 183     | 171     | 199     |
| $b_s$ , mm           | 68.8    | 58.5    | 50.8    | 55.5    | 46.0    |
| $h_c$ , mm           | 36.1    | 44.4    | 53.5    | 47.6    | 61.4    |
| $b_c$ , mm           | 55.4    | 45.1    | 37.4    | 42.1    | 32.6    |
| $h_r$ , mm           | 160     | 171.5   | 160     | 160     | 158.7   |
| $b_r$ , mm           | 33.9    | 34.     | 33.9    | 33.9    | 37.9    |
| $I_{r0}$ , A         | 715     | 840     | 1028    | 847     | 1269    |
| $I_r$ , A            | 1896    | 2121    | 3159    | 3419    | 5020    |
| $\beta$ , degree     | -158.56 | -156.98 | -160.42 | -166.13 | -162.78 |
| $F_r$ , kA           | 319     | 356     | 398     | 431     | 492     |
| $F_s$ , kA           | 196     | 196     | 245     | 294     | 294     |
| $AW_s$ , kA          | 277     | 277     | 346     | 416     | 416     |
| $k_{Mm}$             | 1.748   | 1.820   | 1.712   | 1.548   | 1.666   |
| $P_{ems}$ , MW       | 343.5   | 340.9   | 341.2   | 342.3   | 342.1   |
| $\Delta P_{rs}$ , kW | 851     | 851     | 1064    | 1277    | 1277    |
| $\Phi_{s0}$ , Wb     | 1.339   | 1.328   | 1.102   | 0.920   | 0.919   |
| $\Phi_s$ , Wb        | 1.459   | 1.475   | 1.248   | 1.065   | 1.080   |
| $B_\delta$ , T       | 1.309   | 1.224   | 1.306   | 1.139   | 1.260   |
| $B_{zr}$ , T         | 1.682   | 1.809   | 1.910   | 1.773   | 2.018   |
| $B_{yr}$ , T         | 1.393   | 1.597   | 1.771   | 1.563   | 1.978   |
| $B_{zs}$ , T         | 1.629   | 1.512   | 1.635   | 1.738   | 1.703   |
| $B_{ys}$ , T         | 1.604   | 1.607   | 1.639   | 1.699   | 1.668   |

Here, in addition to already represented values we present:  $I_{r0}$  - rotor current at the idle mode;  $F_r = N_r \cdot I_r$  - EMF of the rotor winding under load;  $F_s = 1.5 \sqrt{2} \cdot I_s \cdot N_s$  - EMF amplitude of the stator windings;  $AW_s = m_s \cdot I_s \cdot N_s$  - ampere-turns of the stator winding which in contrast to  $F_s$  characterize not electromagnetic nature but just design

filling of the winding like  $F_r$ ;  $k_{Mm}$  - TG overload capacity;  $P_{ems}$  - electromagnetic power determined by the electromagnetic torque;  $\Delta P_{rs}$  - electric power loss in the stator winding;  $\Phi_{s0}$ ,  $\Phi_s$  - magnetic fluxes in the gap on the pole division at modes of idle and load; maximum values of the magnetic flux density at the load mode in the center points by parts of the magnetic system:  $B_\delta$  - in the gap;  $B_{zr}$ ,  $B_{yr}$  - in the teeth and the yoke of the rotor core;  $B_{zs}$ ,  $B_{ys}$  - in the teeth and the yoke of the stator core.

In more detail the meaning and procedure for determining the values presented can be found in the works, which list is in [11].

Table 2 presents a harmonic composition of the temporal function of EMF of the phase winding which is determined in accordance with [8]. Here we present the amplitude of the first harmonic  $E_{m,1}$  in absolute terms, as well as the amplitudes of the odd harmonics with numbers  $\nu$  - in relative form  $E_{m,\nu,*} = E_{m,\nu} / E_{m,1}$ .

Table 2

Harmonic composition of the stator winding EMF at various variants of the TG electromagnetic system

| $Q_s$         | 24-1   | 24-2   | 30     | 36-1   | 36-2   |
|---------------|--------|--------|--------|--------|--------|
| $E_{m,1}$ , V | 16715  | 16715  | 16930  | 17198  | 17196  |
| $E_{m3*}$     | 0.0564 | 0.1112 | 0.0647 | 0.0745 | 0.0719 |
| $E_{m5*}$     | 0.0087 | 0.0044 | 0.0048 | 0.0125 | 0.0125 |
| $E_{m7*}$     | 0.000  | 0.0024 | 0.0069 | 0.0024 | 0.0051 |
| $E_{m9*}$     | 0.0038 | 0.000  | 0.0083 | 0.0061 | 0.0063 |
| $E_{m11*}$    | 0.0205 | 0.0166 | 0.0192 | 0.0191 | 0.0221 |
| $E_{m13*}$    | -      | -      | 0.0105 | 0.0181 | 0.0209 |
| $E_{m15*}$    | -      | -      | -      | 0.0024 | 0.0037 |
| $E_{m17*}$    | -      | -      | -      | -      | 0.0052 |
| $d_{distE}$   | 0.9982 | 0.9937 | 0.9976 | 0.9968 | 0.9968 |

The total content of series is characterized by the distortion factor

$$d_{dist} = \frac{E_{m,1}}{\sqrt{\sum_{\nu=1,3,5,\dots}^{N_g} E_{m,\nu}^2}}, \quad (33)$$

where  $N_g$  is the number of accounted harmonics equal  $Q_s/2$ .

This ratio (33) for «pure» sine wave is equal to one, and its reduction indicates increase the role of higher harmonics. Although, in principle, obtained harmonic compositions for considered options of the TG electromagnetic systems are quite acceptable in terms of quality of generated electricity, the more that the main higher harmonic - the third, which at the connection of the stator windings in a «star» in the three-phase system of line voltages theoretically disappears.

Presented in Tables data and models in Fig. 6, 7 give a clear picture of developments during the modernization of the TG electromagnetic system. However, their detailed analysis is beyond the scope of this paper. Their role is to demonstrate the capabilities and efficiency of the developed system of the TG electromagnetic system synthesis on the example of changing the number of slots of the stator core.

### Conclusions.

1. A synthesis system for the TG electromagnetic system is made possible by numerical methods for calculat-

ing magnetic fields in conjunction with high-speed computers and efficient software.

2. Considered variant of synthesis as an example of the TG modernization by changing the number of the stator core slots provided an opportunity for the implementation of principles of construction and implementation of the design synthesis system, in general, and can be, in particular, expanded for the possibility of variation and other parameters of the TG in order to optimize its design.

3. For the practical use in the design of TG the developed and presented synthesis system can be more detailed, specifying the individual components of the mathematical model at maintaining the principles of design and implementation of such a system.

#### REFERENCES

1. Izvekov V.I., Serihin N.A., Abramov A.I. *Proektirovanie turbogeneratorov* [Planning of turbogenerators]. Moscow, MEI Publ., 2005. 440 p. (Rus).
2. Yu.V. Zozulin, O.Ye. Antonov, V.M. Bychik, A.M. Borychevs'kyi, K.O. Kobzar, O.L. Livshyts', V.H. Rakohon, I.Kh. Rohovyy, L.L. Khaymovych, Cherednyk V.I. *Stvorennja novykh typiv ta modernizacija dijuchyh turbogeneratoriv dlja teplovykh elektrychnykh stancij* [Creation of new types and modernization of the existing turbogenerators for the thermal electric stations]. Kharkiv, PF Kolehium Publ., 2011. 228 p. (Ukr).
3. Bianchi Nicola. *Electrical Machine Analysis Using Finite Elements (Copyrighted Material)*. CRC Press, Taylor & Francis Group, University of West Florida, 2005. 276 p.
4. Milykh V.I., Polyakova N.V. Determination of electromagnetic parameters of electric machines based on numerical calculations of magnetic field. *Electrical engineering & electromechanics*, 2006, no.2, pp. 40-46. (Rus). doi: 10.20998/2074-272X.2006.2.09.
5. Meeker D. *Finite Element Method Magnetics. FEMM 4.2 32 bit 11 Oct 2010 Self-Installing Executable*. Available at: [www.femm.info/wiki/OldVersions](http://www.femm.info/wiki/OldVersions) (accessed 10 March 2014).
6. Milykh V.I., Polyakova N.V. A system of directions and phase relationships for electromagnetic parameters at numerical calculations of magnetic fields in a turbogenerator. *Electrical engineering & electromechanics*, 2011, no.5, pp. 33-38. (Rus). doi: 10.20998/2074-272X.2011.5.07.
7. Milykh V.I., Polyakova N.V. Organization of numerical calculation of turbogenerator magnetic field under load with specified output parameters control. *Electrical engineering & electromechanics*, 2012, no.1, pp. 36-41. (Rus). doi: 10.20998/2074-272X.2012.1.08.
8. Milykh V.I., Polyakova N.V. Harmonious analysis of electromagnetic sizes three-phase winding of stators of turbogenerator on basis classic and numeral field methods. *Tekhnichna elektrodynamika*, 2013, no.3, pp. 40-49. (Rus).
9. Milykh V.I., Polyakova N.V. Automated formation of calculation models of turbogenerators for software environment FEMM. *Electrical engineering & electromechanics*, 2015, no.4, pp. 7-14. (Rus). doi: 10.20998/2074-272X.2015.4.02.
10. Milykh V.I., Polyakova N.V. Determination of electromagnetic parameters and phase relations in turbo-generators by the automated calculation of the magnetic field in the software environment FEMM. *Electrical engineering & electromechanics*, 2016, no.1, pp. 26-32. (Rus). doi: 10.20998/2074-272X.2016.1.05.
11. Milykh V.I., Polyakova N.V. Numerically-field calculations of the electromagnetic parameters of turbogenerators. *Bulletin of NTU «KhPI». Series: «Electric machines and electromechanical energy conversion»*, 2014, no.38(1081), pp. 3-18. (Rus).

Received 18.08.2016

V.I. Milykh, Doctor of Technical Science, Professor,  
National Technical University «Kharkiv Polytechnic Institute»,  
21, Kyrpychova Str., Kharkiv, 61002, Ukraine.  
phone +38 057 7076514, e-mail: mvikemkpi@gmail.com

#### How to cite this article:

Milykh V.I. A turbo-generator design synthesis based on the numerical-field calculations at varying the number of stator slots. *Electrical engineering & electromechanics*, 2016, no.6, pp. 19-25. doi: 10.20998/2074-272X.2016.6.04.

B.I. Kuznetsov, T.B. Nikitina, A.V. Voloshko, I.V. Bovdyj, E.V. Vinichenko, B.B. Kobilyanskiy

## SYNTHESIS OF AN ACTIVE SHIELDING SYSTEM OF THE MAGNETIC FIELD OF POWER LINES BASED ON MULTIOBJECTIVE OPTIMIZATION

*Purpose.* The synthesis of the active shielding systems by technogenic magnetic field generated by the different types of high voltage power lines in a given region of space using various cables of controlled magnetic field sources. *Methodology.* The initial parameters for the synthesis of active shielding system parameters are the location of the high voltage power lines with respect to the protected transmission line space, geometry and number of cables, operating currents, as well as the size of the protected space and normative value magnetic field induction, which should be achieved as a result of shielding. The objective of the synthesis of the active shielding system is to determine their number, configuration, spatial arrangement, wiring diagrams and compensation cables currents, setting algorithm of the control systems as well as the resulting value of the induction magnetic field at the points of the protected space. Synthesis of active shielding system is reduced to the problem of multiobjective nonlinear programming with constraints in which calculation of the objective functions and constraints are carried out on the basis of Biot – Savart – Laplace law. The problem is solved by a stochastic multi-agent optimization of multiswarm of particles which can significantly reduce the time to solve it. *Results.* Active screening system synthesis results for the various types of transmission lines and with different amounts of controlled cables is given. The possibility of a significant reduction in the level of induction of the magnetic field source within a given region of space. *Originality.* For the first time carried out the synthesis of the active shielding systems, by magnetic field generated by the different types of high voltage power lines within a given region of space controlled by a magnetic field sources with different amounts of controlled cables. *Practical value, Practical recommendations on reasonable choice of the number and spatial arrangement of compensating cables of active shielding systems for different types of high voltage power lines in order to ensure the effectiveness of a given shielding of the magnetic field high voltage power lines.* References 13. figures 6.

*Key words:* power lines, power frequency magnetic field, active shielding system, multiobjective synthesis, stochastic multi-agent optimization, particle multiswarm.

*Проведен синтез систем активного экранирования техногенного магнитного поля, создаваемого различными воздушными линиями электропередачи внутри заданной области пространства, с помощью управляемых источников магнитного поля. Синтез сводится к решению задачи многокритериального нелинейного программирования с ограничениями, в которой вычисления целевых функций и ограничений выполняются на основании закона Био - Савара - Лапласа. Задача решается методом стохастической мультиагентной оптимизации мультироем частиц, что позволяет существенно сократить время решения. Приведены результаты синтеза систем активного экранирования для различных типов ЛЭП и с различным количеством управляемых обмоток. Показана возможность существенного снижения уровня индукции исходного магнитного поля внутри заданной области пространства. Библ. 13, рис. 6.*

*Ключевые слова:* воздушные линии электропередачи, магнитное поле промышленной частоты, система активного экранирования, многокритериальный синтез, стохастическая мультиагентная оптимизация, мультирой частиц.

**Introduction.** Many residential buildings and structures are located in the vicinity of overhead power lines so that the level of the magnetic flux density inside them exceeds the current sanitary standards. In addition, due to the constant rise in price of land, the construction of residential, administrative and other public buildings in the places where the existing overhead power lines. One possible way of operation of such buildings is the use of active shielding systems.

**Analysis of existing active shielding systems.** The research and implement a variety of active shielding system of man-made magnetic field of industrial frequency currently underway intensively [1-9]. In such systems special coil are used as the executive body of the active shielding system - active cables, the number of which is determined by the specifics of the problem being solved. The most widely used active shielding system with a single coil. [1] To improve the efficiency of the system using two, three, six, twenty-four or more windings [9]. To control these windings can be used a different num-

ber of magnetic field meters - magnetometers: one, two, three, six, twenty-four or more. Number magnetometers, usually equals to the number of controlled winding or number of windings pairs. Specifically, when six type coils Helmholtz coils may be used three magnetometers disposed at the center of the magnetic field shielding region and oriented orthogonally with respect to controlled windings [9].

**The goal of the work** is synthesis and study of systems of active shielding of the magnetic field of industrial frequency generated by a variety of transmission lines with different numbers of magnetic windings of the executive bodies and assessment of the effectiveness of the synthesized systems.

**The formulation of the optimal control problem on the basis of multiobjective optimization.** We consider the solution of the problem of synthesis of systems of active shielding of man-made magnetic field of industrial frequency generated by overhead lines within a given region of space, on the basis of multi-criteria approach.

[12] Technogenic magnetic field is generated by a three-phase overhead power line. Active shielding of the magnetic field sensor system comprises a magnetic field control system, power source and controllable magnetic field source - controlled current windings installed in the zone where it is necessary to maintain the internal magnetic field parameters within specified limits.

At given structure of the system of active magnetic field shielding task active shielding system synthesis in a given space is reduced to the determination of the vector spatial location and geometric dimensions compensated coils, as well as the controller parameters  $X$  at which the maximum value of the magnetic field at selected points  $P_i$  of the considered space  $P$  takes a minimum value

$$X^* = \arg \min_{X \in X} \max_{P_i \in P} B(X, P_i). \quad (1)$$

In minimizing the magnetic flux density  $B(X, P_i)$  at the point  $P_i$  induction values at other points of the space situated in the vicinity of this point is greater than this minimum value, or by undercompensation or by overcompensation level source magnetic field induction using active shielding system. Moreover, as we approach the point in question to the value of the control winding induction becomes significantly greater induction of the initial level of the magnetic field due to overcompensation. Therefore, the problem (13) can not be reduced to the solution of  $m$  local minimize magnetic flux density problems  $B(X, P_i)$  in  $m$  points  $P_i$

$$X_i^* = \arg \min_{X \in X} B(X, P_i), \quad i = \overline{1, m}, \quad (2)$$

and then to the choice of such a solution  $X^*$  from the set of  $m$  local optima  $X_i^*$ ,  $i = \overline{1, m}$  at which the maximum value of the magnetic flux density  $B(X, P_i)$  in all the points  $P_i$  is minimal

$$X^{**} = \arg \min_{i=1, m} \max_{j=1, m} B_{ij}^*(X_i^*, P_j), \quad (3)$$

where  $B_{ij}^*(X_i^*, P_j)$  is the magnetic flux density in the point  $P_j$  calculated at the optimal value of the vector of the desired parameters of regulators  $X_i^*$  found one that minimizes (3) the level of the induction at the point  $P_i$ .

In general, the problem (1) the synthesis of a system of active magnetic shielding power frequency field generated by overhead lines within a given region of space, can be formulated in the form of multi-criteria optimization problem following the vector criterion

$$B(X) = [B(X, P_1), B(X, P_2), \dots, B(X, P_m)]^T, \quad (4)$$

whose components  $B(X, P_i)$  is the vector of induction modules  $m$  points  $P_i$  of the considered space. This, of course, need to be considered limitations on vector control and state variables as a vector and the inequality may equality

$$G(X) \leq G_{\max}, \quad H(X) = 0. \quad (5)$$

Note that the components of the vector criterion (4) and limitations (5) is a nonlinear function of the vector of the desired parameters of regulators  $X$  and their calcula-

tion is performed on the basis of the law of Biot-Savart-Laplace [10, 11].

**A method of solving the problem of multiobjective optimization.** The problem of finding a local minimum of (4) at one point  $P_i$  of the space, as a rule, is multiextremal containing local minima and maxima, therefore, to solve it is advisable to use multi-agent algorithms stochastic optimization [12]. Consider the algorithm for finding the set of Pareto-optimal solutions multicriteria problems of nonlinear programming based on multi-agent stochastic optimization. To date, we developed a large number of particle swarm optimization algorithms - PSO algorithms based on the idea of collective intelligence particle swarm like gbest PSO algorithms and lbest PSO [13]. Application of multi stochastic optimization methods for solving multicriteria problems today raises certain difficulties and this trend continues to grow rapidly [12, 13]. To solve the original multiobjective nonlinear programming problem (4) with constraints (5) construct an algorithm for stochastic optimization of multi-agent based on multiple swarms of particles, the number of which equals the number of components of the vector optimization criterion. In the standard particle swarm optimization algorithm changes velocities of the particles is carried out in a linear fashion. [13] To increase the speed of finding the global optimum algorithm used nonlinear stochastic optimization of multi-agent [12].

With the help of individual  $j$ -th swarms solved the problem of optimizing the scalar criteria  $B(X, P_j)$  which are components of the vector optimization criterion (4). In order to find a global solution to the original multiobjective problem (4) in the search for optimal solutions to local criteria individual swarms exchange information with each other. At the same time to calculate particle swarm speed information is used on a global optimum, received particles of another swarm that allows you to select all of the potential Pareto optimal solutions. To this goal, at each step  $t$  of  $i$ -motion of the particles of the  $j$ -th swarm functions swarm binary preferences of local solutions, received all the swarms. The solution  $X_j^*(t)$  obtained during the optimization objective function  $B(X(t), P_j)$  using the  $j$ -th swarm is preferred relative to the solution  $X_k^*(t)$  resulting in the optimization of the objective function  $B(X(t), P_k)$  with the help of  $k$ -th swarm, i.e.  $X_j^*(t) \succ X_k^*(t)$  if the following condition is correct

$$\max_{i=1, m} B(P_i, X_j^*(t)) < \max_{i=1, m} B(P_i, X_k^*(t)). \quad (6)$$

At the same time as the global optimal solution  $X_k^*(t)$  of the  $k$ -th swarm the global solution  $X_j^*(t)$  is used, the resulting by  $j$ -th swarm which is more advantageous with respect to a global solution  $X_k^*(t)$  of the  $k$ -th swarm on the basis of preference relation (6).

In fact, this approach is implemented the basic idea of the method of successive narrowing of the field of trade-offs - from the initial set of potential solutions based

on the information about the relative importance of local solutions consistently removed all Pareto-optimal solutions, which can be selected according to the available information about the preferences of respect. Removal is carried out until the globally optimal solution. The application of this approach in each step is not the restriction is removed, no potentially optimal solution.

**Results of computer modeling.** We consider the synthesis of the active shielding system of the magnetic field generated by overhead lines of various design, within a given region of space controlled by a magnetic field sources with different amounts of compensating windings and various designs. At the beginning of the active system, consider shielding the magnetic field generated by double-circuit overhead lines having six conductors. As it has been shown by many researchers [3, 5], the magnetic field produced by such a line has an elliptical polarization, which allows to build active shielding system with one compensation winding. It should be noted that such systems are most widely in the world [1, 6, 8]. As an example, Fig. 1 shows the lines of equal levels of magnetic flux density with enabled active magnetic field shielding system with a single executive body of the magnetic coil. As can be seen from this Figure, in this space, where it is necessary to shield the magnetic field, while the system is active shielding level magnetic field does not exceed  $0.4 \mu\text{T}$ , while the level of the source of the magnetic field varies in the range of  $1.8 \mu\text{T}$  to  $0.5 \mu\text{T}$ .

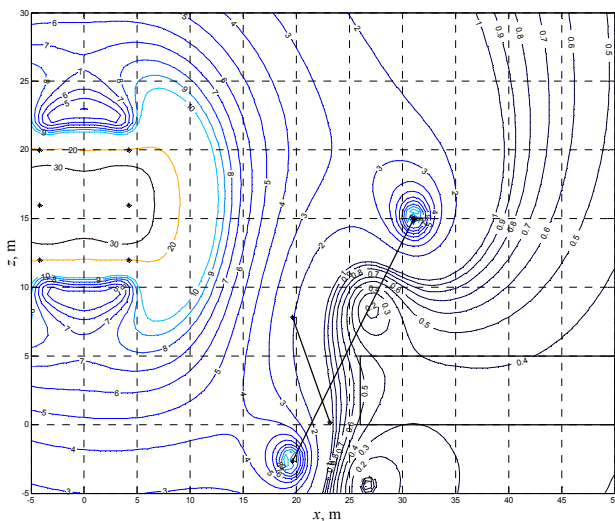


Fig. 1. The lines of equal level of magnetic flux density with enabled active shielding system with one winding

To improve the efficiency of the system will add a further winding, as shown in Fig. 2. In this system, the active layer shielding the magnetic field does not exceed  $0.2 \mu\text{T}$ , while the level of the magnetic field in a system with only one winding is reduced to  $0.4 \mu\text{T}$ .

In the world practice of building systems in addition to the shielding of active single-phase three-phase windings are used as windings, allowing to create a rotating magnetic field, as shown in Fig. 3.

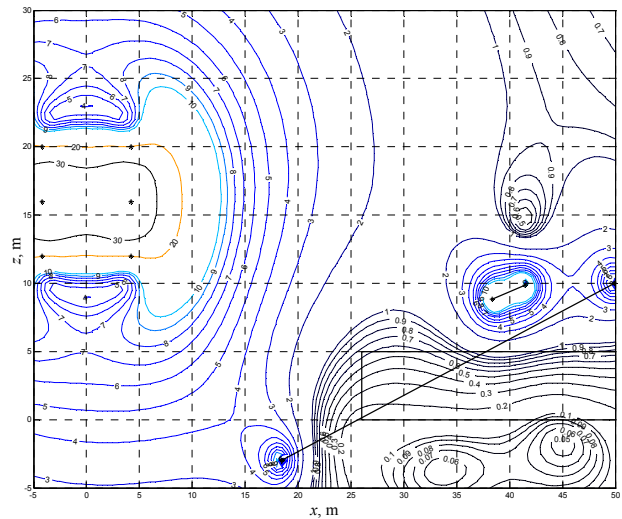


Fig. 2. The lines of equal level of magnetic flux density with enabled active shielding system with two windings

In this system, the magnetic field does not exceed the level of  $0.4 \mu\text{T}$ , so that the system provides the same effectiveness as the system with a single winding, as shown in Fig. 1. However, in this case, three phase winding occupies less space than a single-phase winding at the same efficiency of the system.

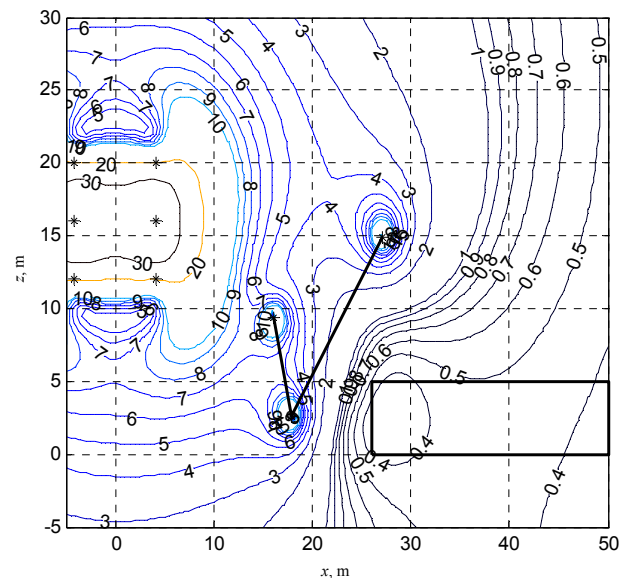


Fig. 3. The lines of equal level of magnetic flux density with enabled active shielding system with three-phase winding

Fig. 4 shows the lines of equal levels of magnetic flux density with enabled active shielding system using a three-phase and single-phase windings. The level of the magnetic field in such a system does not exceed  $0.3 \mu\text{T}$ .

Let us now consider the synthesis of the active shielding system of the magnetic field generated by the single circuit overhead lines having three current-carrying wires. The magnetic field produced by such a line has a substantially circular polarization [3, 5], so that for the construction of active shielding system must use at least two compensation winding.

Fig. 5 shows the lines of equal levels of magnetic flux density with enabled active shielding system with two windings.

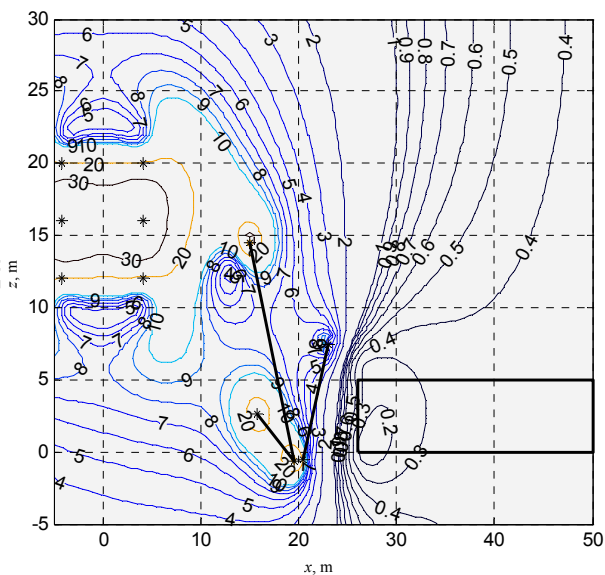


Fig. 4. The lines of equal level of magnetic flux density with enabled active shielding system with three-phase and one-phase windings

As it shown in Fig. 5, in this space, where it is necessary to shield the magnetic field, while the system is active shielding level magnetic field does not exceed  $0.4 \mu\text{T}$ , while the level of the source of the magnetic field varies in the range of  $1.8 \mu\text{T}$  to  $0.5 \mu\text{T}$ .

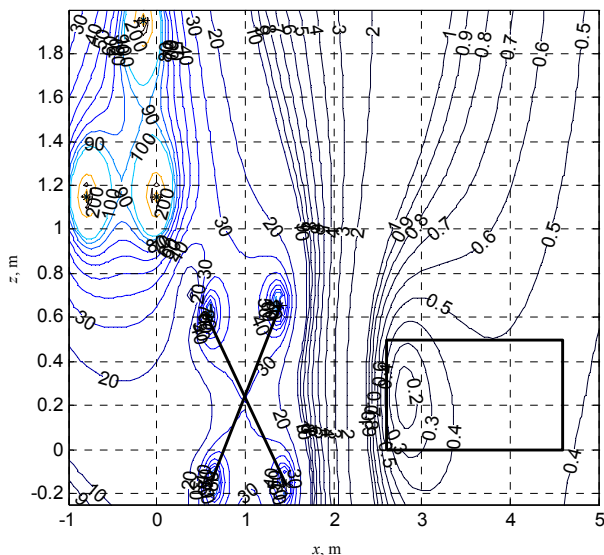


Fig. 5. The lines of equal level of magnetic flux density with enabled active shielding system with two windings

The magnetic field of the circular polarization can also create and use a three-phase winding, as shown in Fig. 6. The level of the magnetic field in such a system does not exceed  $0.4 \mu\text{T}$ .

### Conclusions.

1. It is shown that the problem of the synthesis of the active shielding system is reduced to the problem of multiobjective linear programming with restrictions in which

calculation of the objective functions and constraints are carried out on the basis of the Biot-Savart-Laplace law.

2. It is proposed to implement the solution of the synthesis problem based on constructing Pareto optimal solutions using multi-agent algorithms of stochastic optimization by a particle multiswarm which reduces the time for solving the problem.

3. The possibility of reducing the level of the magnetic flux density inside a given region of space using the synthesized active shielding system four times is confirmed.

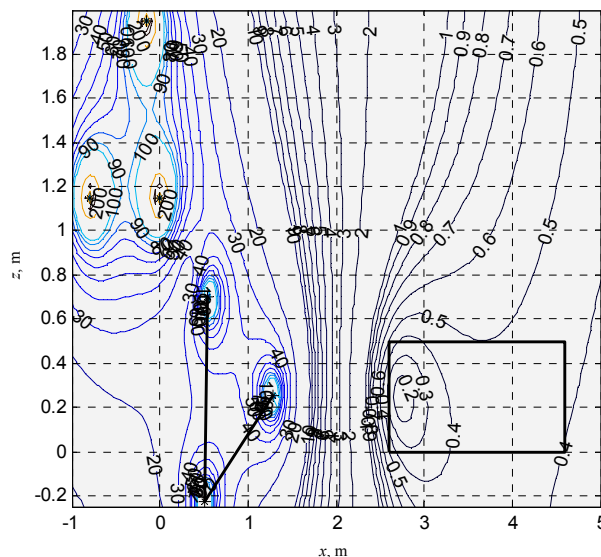


Fig. 6. The lines of equal level of magnetic flux density with enabled active shielding system with three-phase winding

### REFERENCES

1. Active Magnetic Shielding (Field Cancellation). Available at: <http://www.emfservices.com/afcs.html> (accessed 10 September 2012).
2. Beltran H., Fuster V., García M. Magnetic field reduction screening system for a magnetic field source used in industrial applications. *9 Congreso Hispano Luso de Ingeniería Eléctrica (9 CHLIE)*, Marbella (Málaga, Spain), 2005, pp. 84-99.
3. Celozzi S., Garzia F. Active shielding for power-frequency magnetic field reduction using genetic algorithms optimization. *IEE Proceedings – Science, Measurement and Technology*, 2004, Vol.151, no.1, pp. 2-7. doi: 10.1049/ip-smt:20040002.
4. Ter Brake H.J.M., Wieringa H.J., Rogalla H. Improvement of the performance of a mu -metal magnetically shielded room by means of active compensation (biomagnetic applications). *Measurement Science and Technology*, 1991, Vol.2(7), pp. 596-601. doi: 10.1088/0957-0233/2/7/004.
5. Yamazaki K., Kato K., Kobayashi K. MCG Measurement in the environment of active magnetic shield. *Neurology and Clinical Neurophysiology*, 2004, Vol. 40, pp. 1-4.
6. Celozzi S. Active compensation and partial shields for the power-frequency magnetic field reduction. *Conference Paper of IEEE International Symposium on Electromagnetic Compatibility*. Minneapolis (USA), 2002, Vol.1, pp. 222-226. doi: 10.1109/isemc.2002.1032478.
7. Shenkman A., Sonkin N., Kamensky V. Active protection from electromagnetic field hazards of a high voltage power line. *HAIIT Journal of Science and Engineering. Series B: Applied Sciences and Engineering*, Vol. 2, Issues 1-2, pp. 254-265.
8. Ter Brake H.J.M., Huonker R., Rogalla H. New results in active noise compensation for magnetically shielded rooms.

*Measurement Science and Technology*, 1993, Vol. 4, Issue 12, pp. 1370-1375. doi: **10.1088/0957-0233/4/12/010**.

9. Kazuo Kato, Keita Yamazaki, Tomoya Sato, Akira Haga, Takashi Okitsu, Kazuhiro Muramatsu, Tomoaki Ueda, Masahito Yoshizawa. Shielding effect of panel type active magnetic compensation. *IEEEJ Transactions on Fundamentals and Materials*, 2005, Vol. 125, Issue 2, pp. 99-106. doi: **10.1541/ieejfms.125.99**.

10. Rozov V.Yu., Reutsky S.Yu. Pyliugina O.Yu. The method of calculation of the magnetic field of three-phase power lines. *Tekhnichna elektrodynamika*, 2014, no.5, pp. 11-13. (Rus).

11. Nikolova N.K., Bakr M.H. *Electromagnetics I. Matlab Experiments Manual for EE2FH3*. Department of Electrical and Computer Engineering McMaster University, 2012. 96 p.

12. Clerc M. *Particle Swarm Optimization*. London, ISTE Ltd., 2006. 244 p. doi: **10.1002/9780470612163**.

13. Gazi V., Passino K.M. *Swarm Stability and Optimization*. Springer, 2011. 318 p. doi: **10.1007/978-3-642-18041-5**.

B.I. Kuznetsov<sup>1</sup>, Doctor of Technical Science, Professor,

T.B. Nikitina<sup>2</sup>, Doctor of Technical Science, Professor,

A.V. Voloshko<sup>1</sup>, Candidate of Technical Science,

I.V. Bovdyj<sup>1</sup>, Candidate of Technical Science,

E.V. Vinichenko<sup>1</sup>, Candidate of Technical Science,

B.B. Kobilyanskiy<sup>1</sup>, Candidate of Technical Science, Associate Professor,

<sup>1</sup> State Institution «Institute of Technical Problems of Magnetism of the NAS of Ukraine»,

19, Industrialna Str., Kharkiv, 61106, Ukraine,

phone +38 050 5766900, e-mail: bikuznetsov@mail.ru

<sup>2</sup> Kharkov National Automobile and Highway University,

25, Petrovskogo Str., Kharkov, 61002, Ukraine,

e-mail: tatjana55555@gmail.com

Received 15.09.2016

#### How to cite this article:

Kuznetsov B.I., Nikitina T.B., Voloshko A.V., Bovdyj I.V., Vinichenko E.V., Kobilyanskiy B.B. Synthesis of an active shielding system of the magnetic field of power lines based on multiobjective optimization. *Electrical engineering & electromechanics*, 2016, no.6, pp. 26-30. doi: 10.20998/2074-272X.2016.6.05.

D.V. Tugay

## THE PHASE REACTOR INDUCTANCE SELECTION TECHNIQUE FOR POWER ACTIVE FILTER

**Purpose.** The goal is to develop technique of the phase inductance power reactors selection for parallel active filter based on the account both low-frequency and high-frequency components of the electromagnetic processes in a power circuit. **Methodology.** We have applied concepts of the electrical circuits theory, vector analysis, mathematical simulation in Matlab package. **Results.** We have developed a new technique of the phase reactors inductance selection for parallel power active filter. It allows us to obtain the smallest possible value of THD network current. **Originality.** We have increased accuracy of methods of the phase reactor inductance selection for power active filter. **Practical value.** The proposed technique can be used in the design and manufacture of the active power filter for real objects of energy supply. References 12, figures 11.

**Key words:** power active filter, coefficient of harmonic distortion, phase reactors inductance, frequency modulation, Matlab-model of a three-phase energy supply system.

**Цель.** Целью статьи является разработка методики выбора индуктивности фазных реакторов параллельного силового активного фильтра, основанной на учете как низкочастотной так и высокочастотной составляющих электромагнитных процессов в силовой схеме. **Методика.** Для проведения исследований использовались положения теории электрических цепей, векторный анализ, математическое моделирование в пакете Matlab. **Результаты.** Разработана новая методика выбора индуктивности фазных реакторов параллельного силового активного фильтра, позволяющая получить минимально возможное значение коэффициента нелинейных искажений сетевого тока. **Научная новизна.** Повышена точность методов выбора индуктивности фазных реакторов силового активного фильтра. **Практическое значение.** Предложенная методика может использоваться при проектировании и изготовлении силовых активных фильтров для реальных объектов электроснабжения. Библ. 12, рис. 11.

**Ключевые слова:** силовой активный фильтр, коэффициент нелинейных искажений, индуктивность фазных реакторов, частота модуляции, Matlab-модель трехфазной системы электроснабжения.

**Introduction.** Electromagnetic compatibility of electrical consumers with the supply of industrial network is one of the key factors considered in the selection and installation of electrical equipment designed for a large installed capacity. Stringent standards for power quality [1, 2] impose obligations both producers and customers of electrical equipment to take additional measures to comply with them, which affects the characteristics of the end product, its cost, and certification opportunities.

In the industrial and municipal power systems, electric transport the main segment of powerful consumers of electricity consumers up with non-linear characteristics [1-3]. Joint connection to industrial consumers such network causes an increase in emission level of higher harmonic components of the current network, the distortion of the supply voltage circulating in conductors linear reactive currents and, as a consequence, leads to increased energy losses in the power supply system [1-3]. Exclude or partially reduce the listed effects it is possible with the help of modern filter-devices, one of which is power active filter (PAF). PAF of parallel type the simplest diagram of power circuits is shown in Fig. 1 have the greatest popularity.

The power part of the PAF identical scheme of autonomous voltage inverter and executed on the power transistor, diode modules, forming a three-phase bridge shoulders. DC converter unit included a storage capacitor  $C$ , the voltage at which the automatic control system is supported by PAF above the line supply voltage amplitude

$$U_0 = k \cdot \sqrt{3} \cdot U_{sm}, \quad (1)$$

where  $U_{sm}$  is the network phase voltage amplitude;  $k = 1.2-1.6$ .

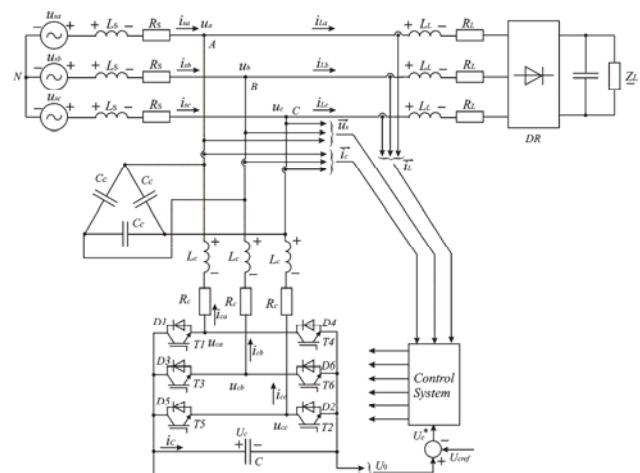


Fig. 1. Diagram of parallel PAF power circuits

In the input circuit of the PAF a three-phase reactor is connected with the parameters of the inductance  $L_c$  and resistance  $R_c$ . To reduce high-frequency noise in the supply voltage at the input of the converter is connected in parallel with a three-phase filter of small capacity  $C_c$ . Despite the simplicity of the power circuit and its power relative small element active filter is a complex dynamic device in which electromagnetic processes and parameters of circuit elements, depending on the mode and parameters of the load and the mains. Along with others, these factors complicate the calculation and selection of parameters of elements of power PAF scheme. The greatest difficulties arise when selecting the input inductance of  $L_c$  reactors, simplified method of calculation which is mainly linked to the taking into account the current growth rate through the reactor

winding commutations with transistor-diode keys, i.e. only the high-frequency component of the electromagnetic processes in a power scheme PAF [5-11]. As was shown in [12], this approach does not allow one to choose the parameters of the input reactor, so you need a new technique based on the specific operating conditions of the power compensator.

**The goal of the paper** is the development of a method of selecting values of phase power inductance of reactors of parallel power active filter based on the account as low-frequency and high-frequency components of the electromagnetic processes in the power circuit.

**Features of the PAF operation.** To analyze the characteristics of the PAF operation we will use a concrete example it is connected in parallel non-linear load, shown in Fig. 1. For the three-phase system with symmetrical sinusoidal voltage source  $u_{sa}, u_{sb}, u_{sc}$  whose parameters  $L_s$  and  $R_s$  are uniquely defined, connected six-pulse uncontrolled rectifier  $DR$  working on  $R-L$  load. To restrict network rectifier ripple current last networked via an inductive reactor  $L_L, R_L$  parameters. PAF is connected to terminals ABC, where there are voltages  $u_a, u_b, u_c$ .

The principle of parallel PAF operation is based on generating compensation currents, which subtracts from the load current allows to obtain the desired shape of network currents. In this example, after connecting the PAF form of line current to be sinusoidal and instant network current should be in phase with the corresponding phase voltage.

Load current vector can be represented by a three-component vector, each component of which is a vector that stores information about the three current values of the respective phase currents

$$\vec{i}_L = [\vec{i}_{1a} \quad \vec{i}_{1r} \quad \vec{i}_{\Sigma l}]^T, \quad (2)$$

where  $\vec{i}_{1a}$  is the vector of the fundamental harmonic active current three-phase system, which coincides with the direction of voltage vector  $\vec{u}_s$  (see Fig. 1);  $\vec{i}_{1r}$  is the vector of the fundamental wave reactive power three-phase system orthogonal to vector  $\vec{i}_{1a}$ ;  $\vec{i}_{\Sigma l}$  is the vector of total current harmonic load three-phase system.

PAF current vector can also be represented by a three-component vector

$$\vec{i}_C = [c_1 \cdot \vec{i}_{1r} \quad c_2 \cdot \vec{i}_{\Sigma l} \quad \vec{i}_{\Sigma h}]^T, \quad (3)$$

where  $\vec{i}_{\Sigma h}$  is the vector total current harmonics whose frequencies are multiples of side-frequency PWM;  $c_1$  is the level of compensation of the primary harmonic of the reactive current ( $0 < c_1 \leq 1$ );  $c_2$  is the level of compensation of the total load current of higher harmonics ( $0 < c_2 \leq 1$ ). The first two components of the vector  $\vec{i}_C$  describing the low-frequency component of the electromagnetic processes in PAF related to the characteristics of the load, and the third component - the high-frequency component, the appearance of which is associated with a feature of the compensator when switching of power semiconductor modules.

According to Fig. 1 and relations (2), (3) the line current vector at the working PAF may comprise four components

$$\vec{i}_S = [\vec{i}_{1a} \quad (1-c_1) \cdot \vec{i}_{1r} \quad (1-c_2) \cdot \vec{i}_{\Sigma l} \quad \vec{i}_{\Sigma h}]^T. \quad (4)$$

Quality compensation will depend on the values of the coefficients  $c_1, c_2$  vector  $\vec{i}_{\Sigma h}$ . Under ideal conditions  $c_1 \approx 1, c_2 \approx 1$ , and  $|\vec{i}_{\Sigma h}| \approx 0$ . To achieve full compensation is virtually impossible in real installations. The quality of the PAF can be estimated value of the distortion factor  $THD_i$  line current. In accordance with (4)  $THD_i$  can be expressed as the sum of two components - a low-frequency ( $THD_{il}$ ) and high-frequency ( $THD_{ih}$ )

$$THD_i = THD_{il} + THD_{ih} = \frac{\sqrt{(1-c_2)^2 \cdot I_{\Sigma l}^2 + I_{\Sigma h}^2}}{\sqrt{I_{1a}^2 + (1-c_1)^2 \cdot I_{1r}^2}}, \quad (5)$$

where  $I_{\Sigma l}^2$  is the the sum of the squares of the rms values of higher harmonic components of the load current;  $I_{\Sigma h}^2$  is the sum of the squares of the rms values of higher harmonic components whose frequencies are multiples of side-frequency PWM.

With an increase in the inductance of the input reactor PAF  $THD_{il}$  low-frequency component is increased, and high-frequency component  $THD_{ih}$  decreases. Thus, there is an optimal value of inductance  $L_{opt}$  corresponding to the minimum possible value  $THD_i$ . To find the value  $L_{opt}$  necessary to examine separately the electromagnetic processes in the PAF on the low and high frequency.

Consider the work of one phase of the PAF in the circuit according to Fig. 1. In the circuit in the open state are alternately transistor diode and one group of the same group opposite phase. For example, with a negative reference current compensator  $i_{ca^*}$  in working condition will be the transistor  $VT1$  and diode  $VD4$  circuit as shown in Fig. 2. The term repeatability mains voltage in accordance with the nature of the non-linear load are three possibilities of joint work with the transistor  $VT1$  transistor other two phases: 1 -  $VT1, VT3, VT2$ ; 2 -  $VT1, VT6, VT5$ ; 3 -  $VT1, VT6, VT2$ . Fig. 1 illustrates the first option. Depending on the duration of the conduction intervals of transistors employed and the current values of the phase voltages on the PAF input for the described embodiment are possible 8 states of the circuit shown in Fig. 3. At the time interval when the transistor  $VT1$ , the energy stored in the capacitor  $C$  is transmitted through the reactor  $L_c$  in the network (Fig. 3,a,b) or stored in a capacitor through the reactors of the other two phases (Fig. 3,c). When transistor  $VT1$  is closed in the open state is  $VD4$  diode, and the energy stored in the reactor is transferred to the condenser, together with additional energy network (Fig. 3,e,g) is either returned to the network (Fig. 3,f). The time intervals in a conducting state when there are three groups of one semiconductor device (Fig. 3,d and Fig. 3,h) the reactor is charged by the network.

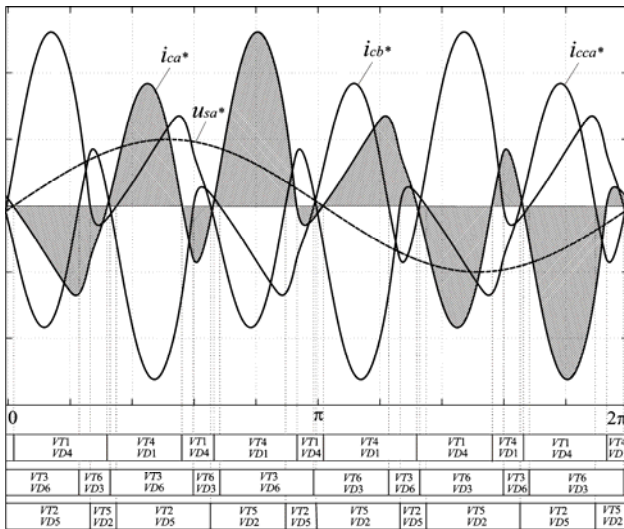


Fig. 2. Phase A operation of the circuit with PAF

**Account of the low-frequency component of the electromagnetic processes in the selection phase inductance reactors.** In accordance with Fig. 1, 2, and by (3) a low-frequency component of the PAF current can be represented as the sum of the reactive component of the first harmonic current, and harmonics of the order  $6n \pm 1$  due to the spectral composition of the input current six-pulse uncontrolled rectifier.

Let us evaluate the effectiveness of the PAF at the frequency of the mains voltage. Fig. 4 shows an equivalent circuit of one phase of the PAF for the fundamental harmonic voltage and current.

The first harmonic voltage, the current at the input rectifier bridge PAF is shown in the equivalent circuit source  $u_{ca1}$  and the load impedance phase - equivalent resistance  $Z_{L1}$ .

Fig. 5,a and shows a vector diagram of the voltages and currents corresponding to the equivalent circuit of Fig. 4. The diagram shows that the instantaneous value of the first harmonic voltage at the input rectifier bridge  $u_{ca1}$  practically in phase with the instantaneous mains voltage  $u_{sa}$ . The amplitude of the fundamental harmonic voltage at the input rectifier bridge ( $U_{mca1}$ ) PAF will always be larger than the amplitude-phase mains voltage ( $U_{mca}$ ) on the value of the voltage drop across the phase reactor  $U_{mcLa1}$

$$U_{mca1} \approx U_{ma} + U_{mcLa1} \quad (6)$$

If we taking into account the orthogonal of vectors of current fundamental harmonic of the network  $\vec{I}_{sa1}$  and fundamental harmonic PAF  $\vec{I}_{ca1}$ , the parameters of the source and the load to take the same, it is possible to prove the existence of the optimal value of inductance phase reactor  $L_{opt1}$  ensuring the fulfillment of the above conditions.

In the vector diagram in Fig. 5,b shows that by increasing the inductance of the phase of the reactor there is a shift of the fundamental harmonic line current with respect to the supply voltage on the light angle  $\varphi$  thereby deteriorating the quality of the PAF compensation.

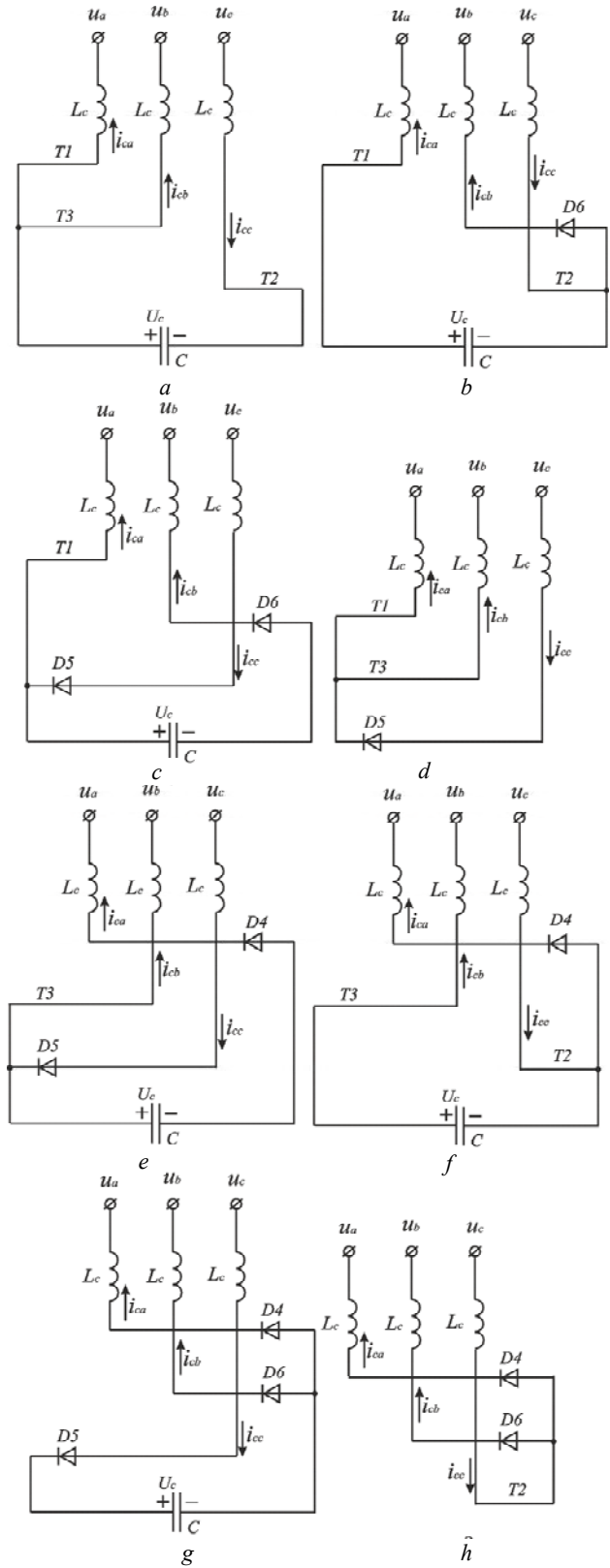


Fig. 3. Possible states of the PAF circuit at transistor  $V_{T1}$  and diode  $V_{D4}$  operation

Using a superposition method according to the equivalent circuit of Fig. 4 write ratio to calculate an integrated value of the fundamental harmonic load current.

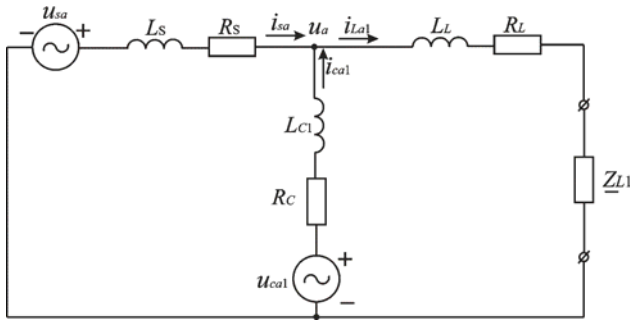


Fig. 4. Equivalent circuit of the PAF one the phase on the network voltage frequency

$$I_{La1} = U_{ma} \cdot \frac{\frac{Z_C}{Z_{11} \cdot (Z_L + Z_C)} - \frac{1}{Z_{11}} + \frac{1}{Z_{22}}}{1 - \frac{Z_C}{Z_{22}}}, \quad (7)$$

where  $Z_C = R_c + j\omega L_{c1}$ ;  $Z_L = R_L + j\omega L_L + Z_{L1}$ ;  $Z_{11} = Z_s + Z_L \cdot Z_C / (Z_L + Z_C)$ ;  $Z_{22} = Z_C + Z_L \cdot Z_s / (Z_L + Z_s)$ ;  $Z_s = R_s + j\omega L_s$ .

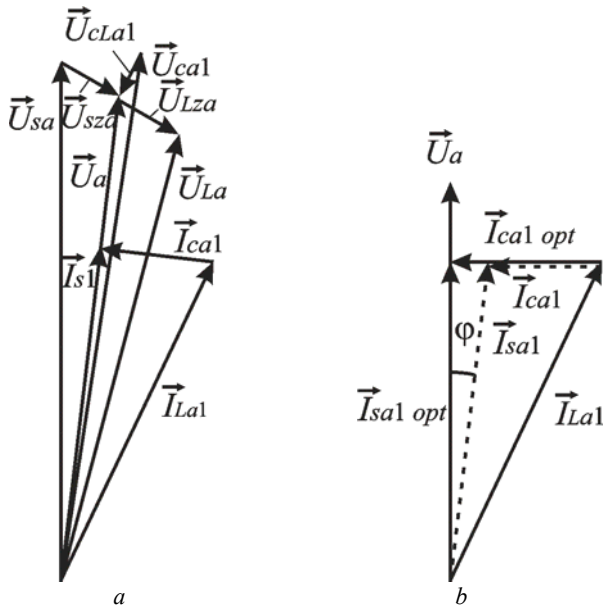


Fig. 5. Vector diagrams of voltages and currents of the equivalent circuit on the network voltage frequency

The real part of the complex values of the fundamental harmonic load current  $\text{Re}(I_{La1})$  corresponds to the optimum value of the fundamental harmonic current network  $I_{sa1 \text{ opt}}$ , and the imaginary part  $\text{Im}(I_{La1})$  – optimal value of the fundamental harmonic current PAF  $I_{ca1 \text{ opt}}$ .

Complex value of the fundamental harmonic voltage at the input of the rectifier bridge PAF

$$\underline{U}_{ca1} = U_a + j \cdot \text{Im}(I_{La1}) \cdot Z_C. \quad (8)$$

From the equivalent circuit (Fig. 4) we express the imaginary part of the complex values of the fundamental harmonic current PAF

$$I_{ca1} = \text{Im} \left( \frac{U_{ca1}}{Z_{22}} - \frac{U_a \cdot Z_L}{Z_{11} \cdot (Z_L + Z_C)} \right). \quad (9)$$

Fig. 6,a and shows the dependence of the fundamental harmonic current PAF on the relative values

(in the total inductance of the load shares  $L_L \Sigma = L_L + \text{Im}(Z_{L1})/\omega$ ) phase inductance PAF reactor at different values of relative total inductance of the load and a fixed value of the network relative inductance  $L_s/L_L \Sigma = 0.065$ . Dependencies are constructed with the following parameters of the equivalent circuit elements:  $U_{ma} = 311.13 \text{ V}$ ,  $R_c = R_L = 0.002 \Omega$ ,  $R_s = 0.00036 \Omega$ ,  $L_L = 75 \mu\text{H}$ ,  $Z_{L1} = 0.438 + j0.358 \Omega$ .

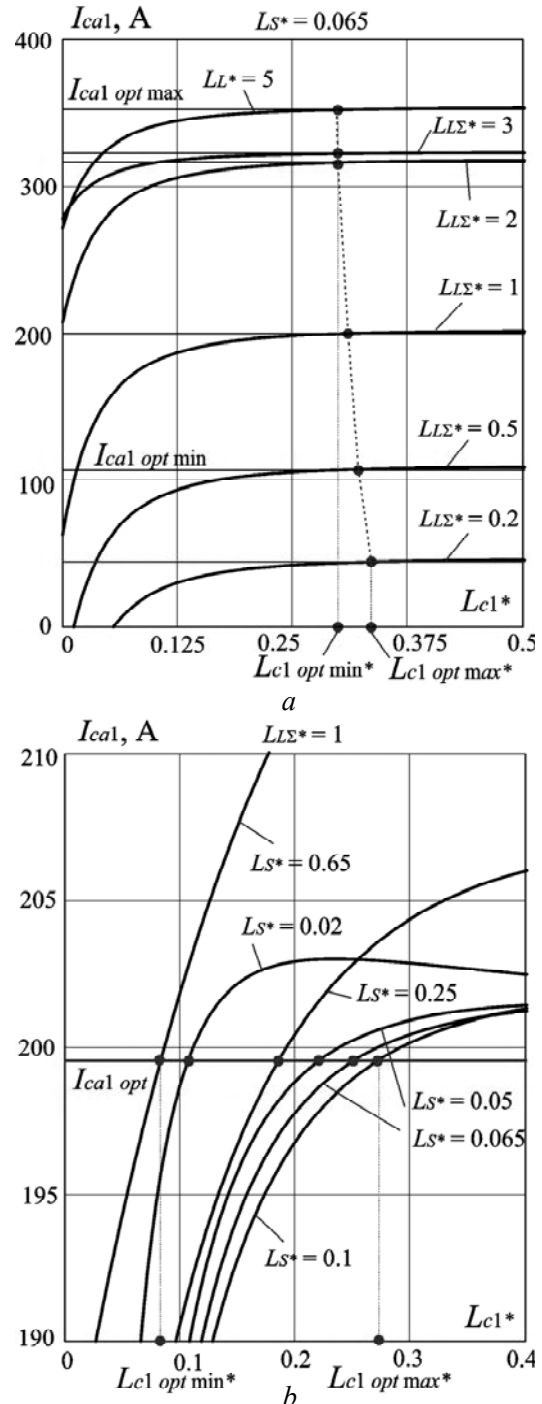


Fig. 6. Dependencies  $I_{ca1} = f(L_{c1}^*)$

Fig. 6,b shows the dependence of the fundamental harmonic current SAF on the relative values of the inductance of the phase reactors SAF for different values of the network inductance and fixed value relative total inductance load  $L_L \Sigma = 1$ .

At the intersection built in Fig. 6 curves with curves corresponding optimal value of current fundamental harmonic PAF  $I_{ca1\ opt}$  are point abscissa are equal to the optimum values of the phase inductance reactors  $L_{opt1}$ .

From a comparison of Fig. 6,a and Fig. 6,b it can be concluded that the optimum value of the phase inductance reactors PAF largely depends on the inductance of the network than the load inductance. If the total inductance of the load changes from  $0.2L_{L\Sigma^*}$  to  $3L_{L\Sigma^*}$  optimum value of the phase inductance reactors PAF decreased from  $0.275L_{L\Sigma^*}$  to  $0.261L_{L\Sigma^*}$ . If you change the network inductance of  $0.02L_{L\Sigma^*}$  to  $0.65L_{L\Sigma^*}$  range of the optimum load inductance is much wider from  $0.083L_{L\Sigma^*}$  to  $0.273L_{L\Sigma^*}$ . Moreover, by increasing the inductance of first optimum network inductance increases, and after a certain  $L_{s^*}$  value decreases.

From the vector diagram in Fig. 6 we obtain the ratio to calculate the angle of the shift of the fundamental harmonic phase current with respect to the appropriate voltage

$$\varphi = \arctan\left(\frac{\text{Im}(I_{La1}) - \text{Im}(I_{ca1})}{\text{Re}(I_{La1})}\right). \quad (10)$$

Fig. 7 shows the dependence of the angle  $\varphi$  of the relative phase inductance reactors  $L_{c1^*}$  for various values of a combination of the relative inductance of the network and relative total inductance of the load.

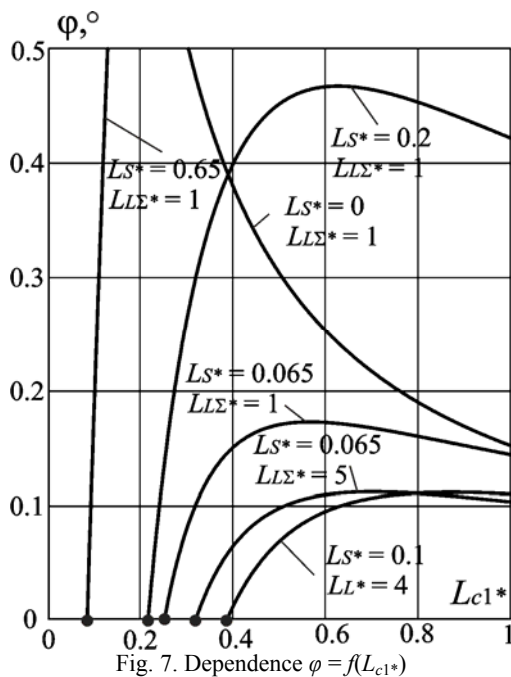


Fig. 7. Dependence  $\varphi = f(L_{c1^*})$

The optimal values of the inductance of the phase reactors correspond to points of intersection of plotting with the horizontal axis ( $\varphi = 0$ ). If the inductance of the network is unknown or tends to zero, the point of intersection of the graph with the x-axis will be absent (see. Fig. 7 at  $L_{s^*} = 0, L_{L\Sigma^*} = 1$ ). In such a case it is necessary to limit the range of variation of inductance values PAF phase reactors, in which the angle  $\varphi$  will not vary by more than  $1^\circ$ . In this example, the corner  $\varphi = 1^\circ$  value corresponds to the inductance of the relative phase reactors  $L_{c1^*} = 0.15$ .

**Account of the high-frequency component of the electromagnetic processes in the selection phase inductance reactors.** We consider the work of one PAF when alternately switched transistor  $VT1$  and diode  $VD4$ . According to Fig. 2 and Fig. 3 in the first working interval  $VT1$  and  $VD4$  alternate conductivity four options PAF circuit state (Fig. 3,a, Fig. 3,d, Fig. 3,f, Fig. 3,h). Fig. 8 shows SAF current shape in the first valve  $VT1$  and  $VD4$  working conduction interval corresponding to one period of modulation  $T_{mod}$ .

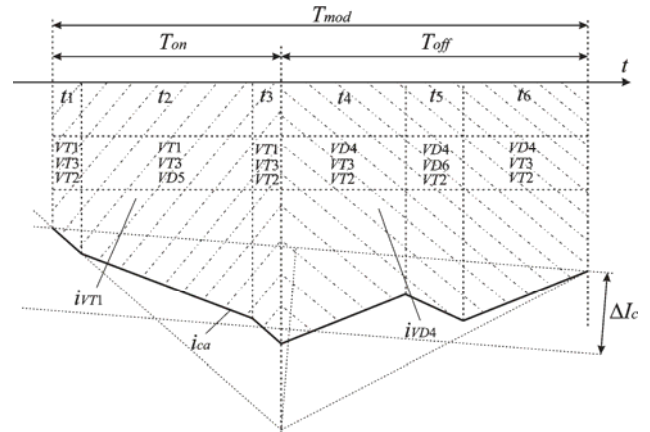


Fig. 8. Current shape of the PAF in the conduction interval  $VT1$  and  $VD4$  corresponding to one period of modulation  $T_{mod}$

The short time intervals  $t1$  and  $t3$  (see. Fig. 3,a) when in the open condition of the transistors  $VT1, VT3, VT2$  the energy stored in the capacitor is transmitted into the network. The time intervals  $t2$  and  $t5$  when in a conducting state at the same time the valves are three phases of one group (see. Fig. 3,d and Fig. 3,h)  $L_c$  reactor stores energy from the network. At time intervals  $t4$  and  $t6$  along with transistors  $VT3, VT2$  involved diode  $VD4$  (Fig. 3, f) the energy stored in the reactor is returned to the network.

From Fig. 8 it can be seen that in the period of modulation  $T_{mod}$  greatest slope of the curve corresponds to the current instant network time intervals  $t1$  and  $t3$ , when open transistors  $VT1, VT3, VT2$ . For Fig. 3,a the following relation is correct

$$\frac{di_{ca}}{dt} L_c = u_{sa} + \frac{U_C}{3}, \quad (11)$$

and for Fig. 3,d

$$\frac{di_{ca}}{dt} L_c = u_{sa}. \quad (12)$$

Using auxiliary constructions shown in Fig. 8, it is easily to determine the maximum angle of PAF current [6]

$$\frac{\Delta i_{ca}}{\Delta t} = \frac{2 \cdot \Delta I_c}{T_{mod}/2} = 4 \cdot \Delta I_c \cdot f_{mod}, \quad (13)$$

where  $\Delta I_c$  is the maximum deviation of the instantaneous current of the current PAF set,  $f_{mod}$  is the frequency pulse width modulation. Let us consider the case when  $f_{mod} = \text{const}$ .

Substituting the relation (1), (13) in (11) we obtain the equation for determining the minimum inductance phase reactor PAF

$$L_{c\min 2} = \frac{U_m \cdot \left(1 - \frac{k}{\sqrt{3}}\right)}{4 \cdot f_{\text{mod}} \cdot \Delta I_{c^*} \cdot \text{Re}(Z_{L1})}, \quad (14)$$

where

$$\Delta I_{c^*} = \frac{\Delta I_c}{I_{s1}} = \frac{\Delta I_c}{\text{Re}(Z_{L1})}. \quad (15)$$

With a high degree of accuracy (14) can be replaced by a simplified relationship

$$L_{c\min 2} = \frac{R_{L\Sigma} \cdot \left(1 - \frac{k}{\sqrt{3}}\right)}{4 \cdot f_{\text{mod}} \cdot \Delta I_{c^*}}. \quad (16)$$

where  $R_{L\Sigma} = R_L + \text{Re}(Z_{L1})$  is the total resistance of the load phase.

From Fig. 3,d in a similar manner to obtain the ratio of the maximum value of PAF inductance phase reactor, substituting (1), (13) in (12) and bearing in mind that the maximum voltage at the time of switching transistor reaches half the phase voltage amplitude  $u_{sa} \approx 0.5U_m$  (see Fig. 2)

$$L_{c\max 2} = \frac{R_{L\Sigma}}{8 \cdot f_{\text{mod}} \cdot \Delta I_{c^*}}. \quad (17)$$

The relative value of the average inductance of the reactor phase

$$L_{c2^*} = \frac{L_{c\min 2} + L_{c\max 2}}{2 \cdot L_{L\Sigma}} = \frac{1.5 - \frac{k}{\sqrt{3}}}{8 \cdot f_{\text{mod}} \cdot \Delta I_{c^*} \cdot \tau_L}, \quad (18)$$

where  $\tau_L = L_{L\Sigma}/R_{L\Sigma}$  is the time constant of the load phase.

Fig. 9 shows the dependence of the relative values of the inductance of the phase reactors by PAF parameter  $\Delta I_{c^*}$  for various values of the modulation frequency  $f_{\text{mod}}$  for these parameters earlier scheme.

**Method of choosing PAF inductance.** On the basis of the material presented above describe the steps to select inductance phase reactors PAF. Consider a specific example of the application of the scheme PAF with the previous settings of its elements.

1. We determine total load inductance  $L_{L\Sigma} = L_L + \text{Im}(Z_{L1})/\omega$ . In the example  $L_{L\Sigma} = 0.433$  mH.

2. From the known parameters of the scheme, using the relation (7) expect to complete the value of the first harmonic of the load current. In the example  $I_{L1} = 645.4 - j199.5$  A.

3. Using (8) we obtain the relation for the calculation of the first harmonic current SAF in the form (9).

4. By (10) we build dependence  $\varphi = f(L_{c1^*})$  (see Fig. 7).

5. At the intersection of the curve  $\varphi = f(L_{c1^*})$  with the  $x$ -axis determines the point coordinate which corresponds to the optimum value of the relative phase of the reactor inductance PAF. In the example  $L_{c1\text{ opt}^*} = 0.249$  ( $L_{c1\text{ opt}} = 0.108$  mH).

6. The obtained value of inductance is substituted in equation (18) and determines the relative value of the maximum deviation of the instantaneous current of the given current PAF  $\Delta I_{c^*}$ . In the example  $\Delta I_{c^*} = 0.059$ .

7. If the value  $\Delta I_{c^*}$  more than 5 % from the first harmonic amplitude of the current network, we make adjustments of parameters. In the example, you can slightly increase the modulation frequency to the value  $f_{\text{mod}} = 7045$  Hz, and  $\Delta I_{c^*} = 0.05$ .

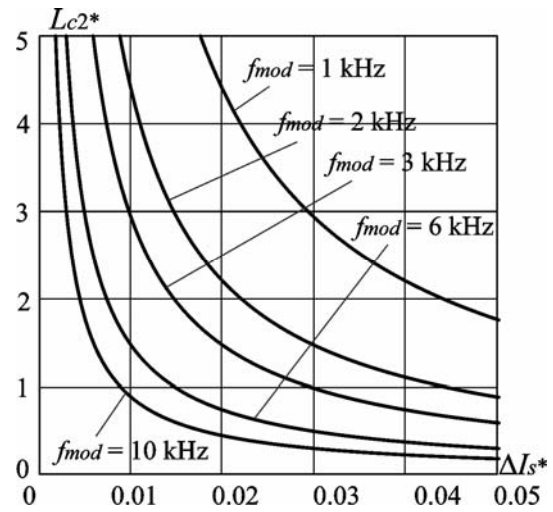


Fig. 9. Dependencies  $L_{c2^*} = f(\Delta I_{s^*})$

**Experimental verification of the theoretical results.** To test the proposed methodology has been developed Matlab-model of a three-phase power supply system with a non-linear load and parallel active filter shown in Fig. 10.

Matlab-model consists of 5 groups of blocks:

1. Power circuit (Us – three-phase voltage source with definable parameters; DR – three-phase uncontrolled rectifier; Load – rectifier load; PAF – inverter bridge of PAF; C – DC link capacitor of PAF; Rc – charging resistor; LL – load current smoothing reactor; Lpaf1, Lpaf2 – PAF phase reactor divided into two sections; Cpaf – PAF input capacitor filter; SA\_PAF, SA\_C – three-phase contactors of PAF and capacitor filter, respectively).

2. Currents and voltages sensors (blocks Is, IL, Ipaf, U, UL, Upaf, UC).

3. Control system (Control System – PAF control system; Gate\_Paf, Gate\_G, Gate\_C, Gate\_R – power circuit control blocks).

4. Measuring subsystem (Measurements – subsystem for calculating total harmonic distortion and operating currents).

5. Virtual instrumentation (Multimeters – multimeters; Us\_Is, Upaf\_Ipaf, Uc – oscilloscopes).

For computer simulation the same parameters elements of the power circuit, as for the calculation of the phase inductance reactors PAF were chosen. In the experiment, the input capacitor filter PAF has been disconnected.

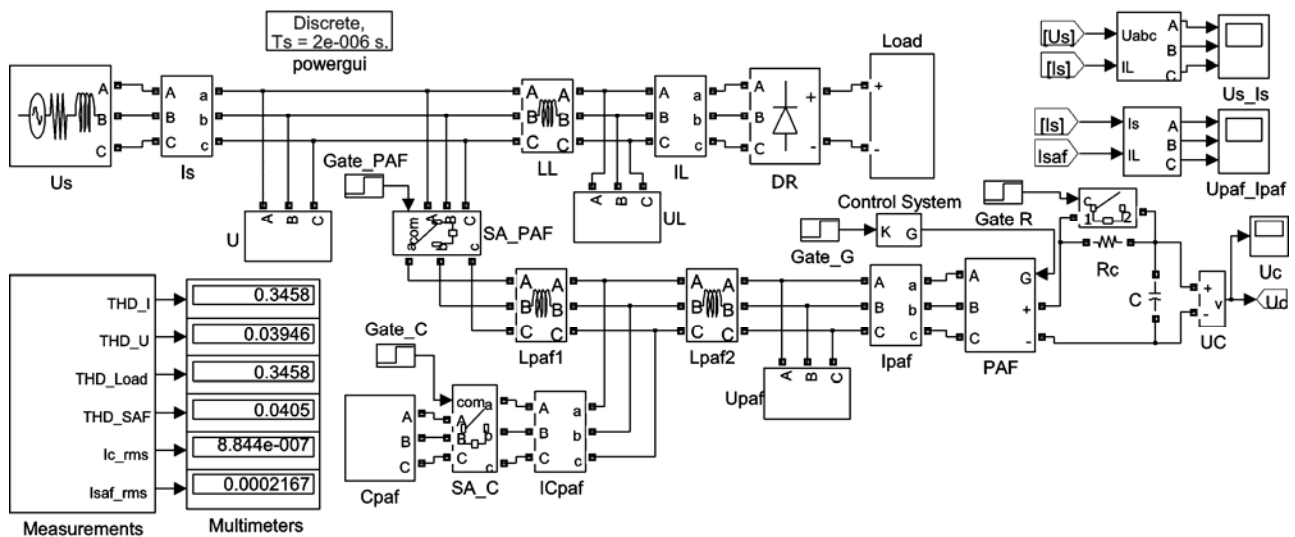


Fig. 10. Matlab-model of the three-phase power supply system with PAF

Fig. 11 shows the current waveform of phase A for three values of the relative phase inductance reactors PAF:  $L_{c^*} = L_{opt} = 0.249$  - Fig. 11,a;  $L_{c^*} = 0.577$  - Fig. 11,b;  $L_{c^*} = 0.093$  - Fig. 11,c. In the figures also indicate the values of the line current THD. The experiment confirmed that the minimum possible value of the line current THD for given circuit parameters corresponding to the selected value of the inductance of the phase reactors PAF. Further studies have shown that when the input PAF C-filter (see Fig. 1) THD line current can be reduced by 1% (i.e., up to 5%).

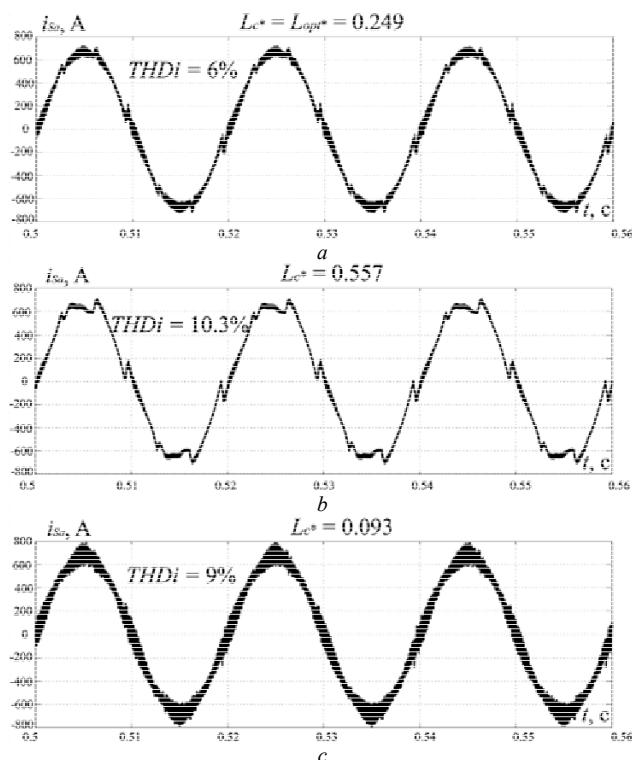


Fig. 11. Waveforms of the network current of the phase A at three values of the PAF phase reactors inductance

### Conclusions.

1. The correct choice of inductance of PAF should be based on the account of the two components of the electromagnetic processes in the power circuit - the low-

frequency one related with compensation of reactive power and harmonic load current and high frequency one associated with the processes of «pumping» of energy in phase reactor of PAF.

2. It is proved that the optimal value of inductance of phase reactors corresponds to the smallest possible THD of the line current.

3. The method of selecting inductance of PAF phase reactors taking into account the parameters of elements of the supply network and the load, i.e., the specific operating conditions of the PAF in the power supply system is developed. The proposed method can be used in the design and manufacture of PAF for installation on concrete objects.

### REFERENCES

1. EN 50160:2010 Voltage characteristics of electricity supplied by public distribution networks.
2. IEC 61000-3-4 Electromagnetic compatibility (EMC) – Part 3-4: Limits – Limitation of emission of harmonic currents in low-voltage power supply systems for equipment with rated current greater than 16 A.
3. Hafner J., Aredes M., Heumann K. A shunt active power filter applied to high voltage distribution lines. *IEEE Transactions on Power Delivery*, 1997, vol.12, no.1, pp. 266-272. doi: 10.1109/61.568249.
4. Bhattacharya S., Frank T., Divan D., Banerjee B. Parallel active filter system implementation and design issues for utility interface of adjustable speed drive systems. *IAS '96. Conference Record of the 1996 IEEE Industry Applications Conference Thirty-First IAS Annual Meeting*, 1996, pp. 1032-1039. doi: 10.1109/ias.1996.560208.
5. Moran L.A., Dixon J.W., Wallace R.R. A three-phase active power filter operating with fixed switching frequency for reactive power and current harmonic compensation. *IEEE Transactions on Industrial Electronics*, 1995, vol.42, no.4, pp. 402-408. doi: 10.1109/41.402480.
6. Aburto V., Schneider M., Moran L., Dixon J. An active power filter implemented with a three-level NPC voltage-source inverter. *PESC97. Record 28th Annual IEEE Power Electronics Specialists Conference. Formerly Power Conditioning Specialists Conference 1970-71. Power Processing and Electronic Specialists Conference 1972*, 1997, vol.2, pp. 1121-1126. doi: 10.1109/PESC.1997.616889.
7. Al-Zamil A.M., Torrey D.A. A passive series, active shunt filter for high power applications. *IEEE Transactions on Power*

*Electronics*, 2001, vol.16, no.1, pp. 101-109. doi: **10.1109/63.903994**.

8. Asiminoaei L., Eddy A., Prasad N.E., Blaabjerg F. Shunt active-power-filter topology based on parallel interleaved inverters. *IEEE Transactions on Industrial Electronics*, 2008, vol.55, no.3, pp. 1175-1189. doi: **10.1109/TIE.2007.907671**.

9. Bento A.A.M., da Silva E.R.C., Praça P.P. Integrated one-cycle control for three-leg universal active power filter. *2008 IEEE Power Electronics Specialists Conference*, June, 2008, pp. 3974-3980. doi: **10.1109/PESC.2008.4592575**.

10. Ivanets S.A., Gusev O.O., Chub A.I. Methods of elements selection for parallel filter-compensating converter. *Journal of Chernihiv State Technological University. Series: Engineering*, 2009, no.40, pp. 223-232. (Ukr).

11. Stepenko S.A., Gusev O.O., Ivanets S.A., Veligorskyi O.A. Comparative analysis of methods for control of filter-compensating devices. *Bulletin of the Kyiv National University of Technologies and Design*, 2012, no.1, pp. 82-88. (Ukr).

12. Zhemerov G.G., Krylov D.S., Tugay D.V. Verification of the calculation elements and high-quality performance of the power supply system with a parallel power active filter. *Bulletin of NTU «KhPI»*, 2015, no.12, pp. 394-397. (Rus).

*Received 27.10.2016*

*D.V. Tugay, Candidate of Technical Science, Associate Professor,*

*O.M. Beketov National University of Urban Economy in Kharkiv,*

*12, Revolution Str., Kharkiv, 61002, Ukraine.*

*phone +38 057 7073111, e-mail: tugaydv@yandex.ua*

*How to cite this article:*

Tugay D.V. The phase reactor inductance selection technique for power active filter. *Electrical engineering & electro-mechanics*, 2016, no.6, pp. 31-38. doi: 10.20998/2074-272X.2016.6.06.

E.A. Yushkov

## MODELING OF OPERATION MODES OF SHIP POWER PLANT OF COMBINED PROPULSION COMPLEX WITH CONTROL SYSTEM BASED ON ELECTRONIC CONTROLLERS

*Purpose. Designing of diagrams to optimize mathematic model of the ship power plant (SPP) combined propulsion complexes (CPC) for decreasing operational loss and increasing fuel efficiency with simultaneous load limiting on medium revolutions diesel generator (MRDG) by criterion reducing of wear and increasing operation time between repairs. Methodology. After analyzing of ship power plant modes of CPC proposed diagrams to optimize mathematic model of the above mentioned complex. The model based on using of electronic controllers in automatic regulation and control systems for diesel and thruster which allow to actualize more complicated control algorithm with viewpoint of increasing working efficiency of ship power plant at normal and emergency modes. Results. Determined suitability of comparative computer modeling in MatLab Simulink for building of imitation model objects based on it block diagrams and mathematic descriptions. Actualized diagrams to optimize mathematic model of the ship's power plant (SPP) combined propulsion complexes (CPC) with Azipod system in MatLab Simulink software package Ships\_CPC for decreasing operational loss and increasing fuel efficiency with simultaneous load limiting on medium revolutions diesel generator (MRDG) by criterion reducing of wear and increasing operation time between repairs. The function blocks of proposed complex are the main structural units which allow to investigate it normal and emergency modes. Originality. This model represents a set of functional blocks of the components SPP CPC, built on the principle of «input-output». For example, the function boxes outputs of PID-regulators of MRDG depends from set excitation voltage and rotating frequency that in turn depends from power-station load and respond that is a ship moving or dynamically positioning, and come on input (inputs) of thruster rotating frequency PID-regulator models. Practical value. The results of researches planned to use in creation of software package Ships\_CPC, in Mat Lab/Simulink was developed under the state budget project «Concepts, technologies and ways of improving ship plants combined propulsion complexes» at the Department of Electromechanics and Electrical Engineering of National University «Odessa Maritime Academy» (State registration number 0114u000340). References 9, figures 6.*

*Key words: ship power plants, combined propulsion complex, mathematical modeling, electronic controller, thruster, diesel, dynamic positioning.*

*В результате анализа режимов работы судовой энергетической установки комбинированного пропульсивного комплекса предложены схемы оптимизации математической модели указанного комплекса. Модель основана на применении электронных регуляторов в системах автоматического регулирования и управления дизелем и подруливающим устройством, которые позволяют реализовать более сложные алгоритмы управления с точки зрения повышения эффективности работы судовой энергетической установки при нормальных и аварийных режимах. Библ. 9, рис. 6.*

*Ключевые слова: судовой энергетической установка, комбинированный пропульсивный комплекс, математическое моделирование, электронный регулятор, подруливающее устройство, дизель, динамическое позиционирование.*

**Introduction.** In recent years rowing power plants (RPP) are the best solutions for certain types of ships. The so-called combined propulsive systems (CPS) with electric propulsion motors on shaft line are variable speed throughout the range of coordinates with direct control moment and powered on based on many tire designs flexible systems AC uneven distribution impedance [1, 2] which are the only ones with multiple power grids diesel-generators or turbo-generators which have found many advantages in several areas of shipbuilding. Fuel savings, reduced maintenance costs, improved flexibility, high reliability, reduced noise and vibration - this is the main thing that marks these systems on the market today. An additional start-up costs associated with the increase in the number of components does not negate these advantages, because such systems are very flexible in terms of operation, management and placement on board. Electrical equipment also shows high efficacy in a large range of operational modes. But to take advantage of such systems today require study of existing models of RPP SPC, developing new models and management strategies, analysis and optimization of marine vessels operating in various operating conditions [3], particularly on hold position (DP).

**Problem definition.** Detailed mathematical models of RPP SPC are presented and studied very carefully cont recent years [4], where the emphasis is given to medium-torque diesel generators (MTDG). We know that ship power systems that have stringent requirements for voltage and frequency so that MTDG models developed from this review have no prospects for change. They differ in power and consumption of power.

Frequency converters (FC), thruster (T) and other internal load include functional blocks of the power consumption of the overall distribution of active and reactive power. PID-controllers of MTDG, T and automatic voltage regulators (AVR) checked in terms of performance [5], and it turned out that it is enough for simulations that cover the main indicators of supply ship power plant (SPP) CPS but not enough to account degradation effects occurring on lines shaft [6, 7].

At present the technical operation of such systems are the following problems:

- compliance with the requirements of quality management (*Failure modes and effects analysis - FMEA*) encountered during operation;

© E.A. Yushkov

- unification of power distribution management system (*Power Management System - PMS*) in combination functions in relation to other similar;
- independence components of *PMS* from each other, even to the level sensors;
- not only reduce power in the calculation of the total estimated load, but also load single generator;
- conformity of the conditions of increased pressure in terms of adequacy to ensure the normal operation depending on any abnormal situation and reloading ship power system (*SPS*) in general.

To solve the above problems it is necessary, based on theoretical assumptions regarding electronic controllers and models of heat engines and maneuvering propulsion device, design a circuit optimization mathematical SPP SPC which would allow to implement more complex control algorithms in terms of improving the efficiency of SPP for the entire range load.

**The goal of the paper** is the development of schemes of optimization mathematical model of SPP SPC with screw-type Azipod steering installation to reduce operating costs and improve fuel efficiency while loading restriction on the criterion MTDG reduce wear and increase turnaround time.

MTDG are generally designed for short-term overload up to 115 % of nominal. Power generation units

located on three in two engine rooms (ER). Each ER has an independent system of support mechanisms that include fuel system, air pressure and low cooling water that are able to cross-connect. Two groups of three MTDG are connected to the two main sections of tires of high voltage. Section interconnected sectional switch.

From the main switchboard (MSB) by reducing the high voltage transformers will supply switchboards (SSB) of own needs and transformers for power supply to electric technology inherent in this type of vessel. Low voltage distribution system consists of two main tires left and right sides at the main deck, which are fed from the main transformer high-voltage interconnected switches that interlocked with the transformer feeder breakers.

Each MTDG is equipped by independent system of control and regulation of power (Fig. 1). Complete switching SODH include: relays generator, digital module synchronization and load distribution, *PLC* with interface I/O, power converters and remote control panel with alarm. MTDG are staffed by management system (*Electro-Motive Diesel Engine Control system - EMDEC*) which provides speed control with closed loop, injection, start/stop function and alarm. EMDEC MTDG is operating from the 24/48 V DC dedicated battery/charger.

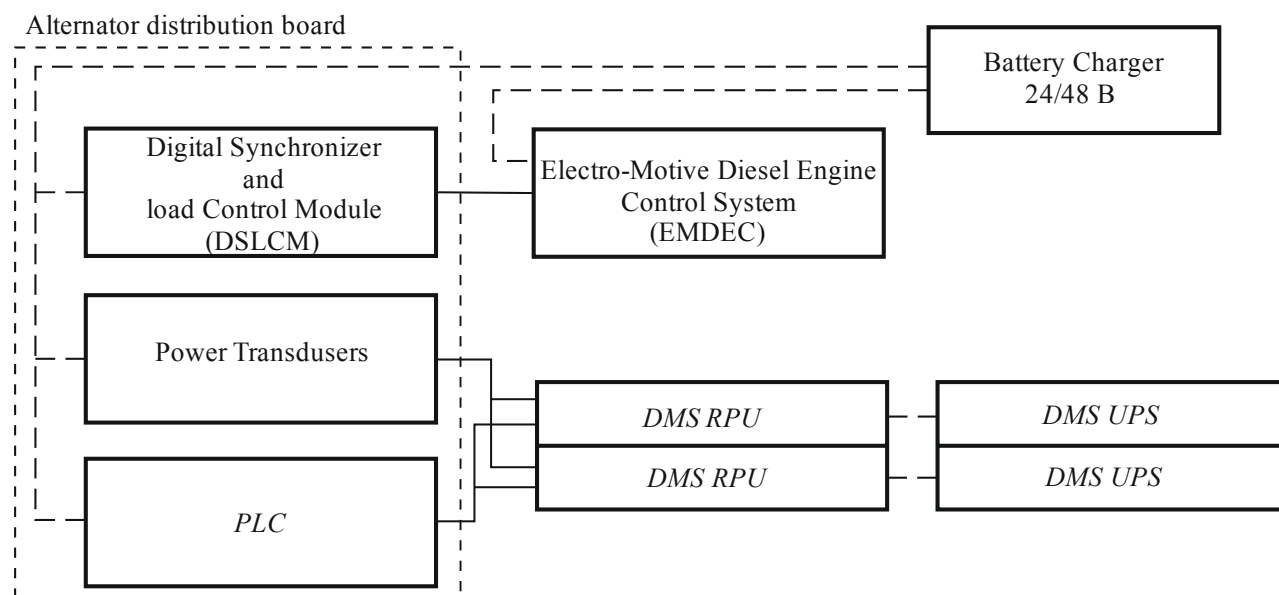


Fig. 1. MTDG control system configuration: *PLC* – programmed logic controller; *DMS* – data management system; *RPU* – reserve power unit; *UPS* – uninterruptible power supply

MTDG can be run from the front panel in manual mode or remote mode «Auto» by the system *DMS*. Distribution *PLC* controls the functions of the engine, and the digital module synchronization and load control *DSLCCM* controls the timing and distribution of power.

*DP* system is double-redundant (Fig. 2). Two main operator consoles (*ASK1*, *ASK2*) contain control processors, keyboards, control and display. *DP* system can control up to eight engines *T*, as usual - to four. Control console located in the chassis scars, which also has three signal processing devices (*SPU1*, *SPU2*, *SPU3*), which are the devices I/O signals from the power position sen-

sors, gyroscopes, sensors and wind movement. Each individual unit has an independent channel of communication with the main central control computer.

Two signal processing units (*SPU4* and *SPU5*) located at the MSB carry out signal processing function power management on two backup devices interface I/O.

As sources of electricity in handheld power plant salient-pole brushless synchronous generators (SG) of high voltage with diesel- or turbo-drive are used. The most convenient form of mathematical models of these machines is machines in the form of an orthogonal coordinate system *d*, *q* which is rigidly connected to the rotor

and rotates with it with a synchronous speed [8]. This coordinate system has advantages over a fixed coordinate system  $a, b, c$  in which, during rotation of the rotor axis of the rotor and stator windings mutually moved because phase AC voltage, current and flux expressed in periodic variables. Vectors voltage, current and flux in the perpendicular arranged axes  $d, q$  are constant and relatively fixed

axes, which excludes mutual between them and simplifies the analysis model. The disadvantages of modeling in axes  $d, q$  include the inability to study asymmetric modes. In order to improve clarity and simplify the simulation results analysis more convenient to use equations in relative units.

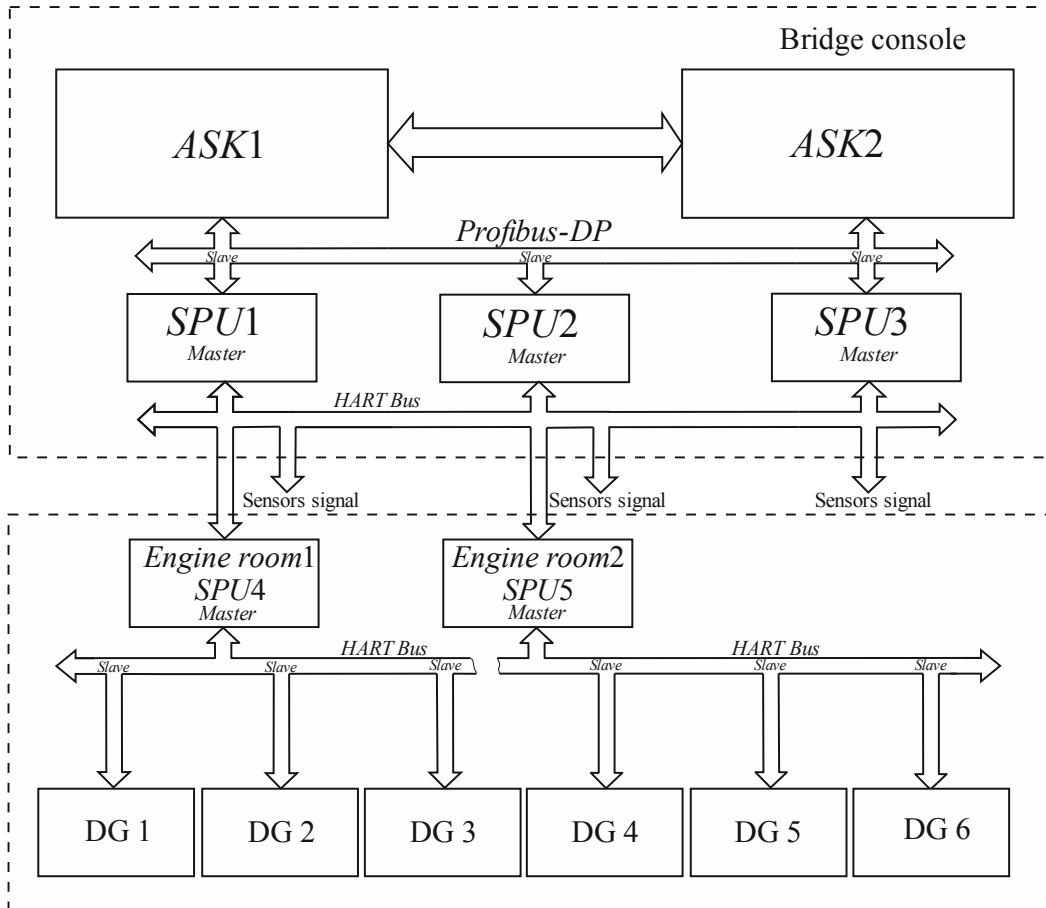


Fig. 2. DP system structure: ASK – Automatic Station Keeping; SPU – Signal Processing Unit; HART – Highway Addressable Remote Transducer Protocol

For rigid framework of fixed voltage and frequency for the MSB and SSB used for standard voltage and power factor on modular tires. Ship power system is isolated and models presented in this article, a rotor speed SG chosen as the base, and viewing other power generators are calculated in relation to it. The angle of the base power generator and the voltage on the tire load module is calculated according to the current generator.

For each of the SG model of the 7th order is used, and the relationship between generators through load module that represents the overall burden as AC impedance, which makes the vector components of the load to the output current generators and voltage vector returns on tires depending on the load characteristics (constant impedance, constant power, etc.). Electric values are modeled in axes  $d, q$ . For example, one model MTDG model consists of diesel and SG, PID speed control diesel and AVR. Function on/off for each part MTDG model simulations load connecting/disconnecting this unit to the MSB. The scheme of the general structure of the model with input and output parameters is shown in Fig. 3.

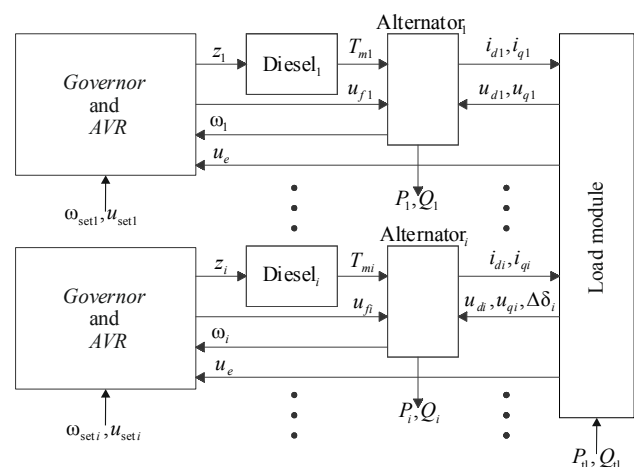


Fig. 3. Flowchart of the ship power plant model:  $z$  – fuel index, relative units.;  $T_m$  – diesel time constant, s;  $u_f$  – excitation voltage setpoint, relative units;  $\omega$  – MTDG shaft rotation speed, rad<sup>-1</sup>;  $i_d, i_q, u_d, u_q$  – current and voltage components by corresponding axes, relative units;  $P, Q$  – active and reactive powers, relative units.;  $\Delta\delta$  – load angle, rad

Developing an AVR mathematical model based on electronic PID-controller and the power semiconductor switch, consider their characteristics [9]. Appointment proportional integral differential (PID) controller is to maintain the specified value  $u_{set}$  some input values through its comparison with the initial current value which is made by negative feedback signal  $u_{fb}$ . The difference between these two values is called inconsistency or deviation from the set value. The power semiconductor switch (PSS) of AVR serves as a key between a source of constant tension and winding brushless exciter. Voltage control pathogen carried by regulating the duration included (disconnected) state of the key semiconductor, i.e. by pulse width submitted to the excitation winding of the exciter. This type of regulation is called pulse width (PWM), and the PSS have a switching frequency of 10 kHz. In general, the power converter is nonlinear dynamic link. Since the switching frequency is much higher than the bandwidth of the system, the power converter can also be viewed as lagless link. As a link in the system of regulation, the PSS is usually described aperiodic link or link with a delay.

For normal AVR operation must be specified limit values of the output voltage to prevent situations over-excited and under excited generator. Block restrictions - a stabilizing element. Also, the model must be supplemented AVR element that describes a measuring alternating voltage generator in DC signals adapted for PID controller. The converter converts the voltage signals into digital instrument transformers, its transfer function can also be expressed in terms of aperiodic link of the first order.

Regulatory parameter MTDG drive motor as the object of the automatic control system (ACS) is the speed of its shaft. The moment of the engine, offset by losses and moment resistance point generator, which prevent rotation of the shaft. Torque engine depends on the amount of fuel which enters it, thus regulating effect on the frequency of rotation of the motor shaft creates a regulatory body that changes the amount of fuel. For diesel this regulatory body is rail of the high-pressure fuel pumps (HPFP). In ship MTDG producing alternating current to drive sustainability rotational speed of the diesel engine are presented the most stringent requirements, provided that the requirements of regulations to ship frequency alternating current network, so you need to support high-speed diesel drive mode with high accuracy, irrespective of changing the ship's electrical load power. For this purpose, the system of automatic speed control. Currently, the ships of the old buildings are used in mechanical and hydromechanical regulators rotational speed diesel engines that have proven to be reliable working regulating device. However, the functionality of these controllers are limited, therefore improving modern automatic control systems (ACS) and systems of automatic control (SAC) ship diesel engines is moving towards the use of electronic controls based on microprocessor.

With the use of electronic controls in ACS and SAC diesel engine provided a new, higher level, allowing you to implement more complex control algorithms diesel and provide previously unattainable performance quality of the regulation of its speed. A prerequisite for this process

of improving the quality of regulation is to optimize how the structure of the regulator and its parameters. Choosing the structure of regulatory law and regulation is determined by several factors. In modern SPP SPC MTDG equipped with digital PID-control speed. In addition, you must also add the block, describing servomechanism HPFP rails, as which can be used executive electric and electrohydraulic units. In this case, the most convenient is to describe this item using aperiodic links of the first order. The very same diesel engine introduces some delay after repositioning rail fuel pump to a corresponding change in the frequency of rotation of its shaft is connected with the time on the course of chemical processes inside the combustion chamber, as well as the inertia of mechanical assemblies. Because it is most preferably diesel seems like pure link delay.

**Results of investigations.** Structural models of electronic AVR and regulator speed diesel according to Fig. 3, based on mathematical models of its key elements, according to the above conditions, are presented in Fig. 4.

The modeling will be done in *MatLab Simulink*, and, given the results of studies, dependence and transfer functions control speed T [5] operating in different modes that correspond to a particular operating mode of the ship in general, try to get the graphics speed shaft T and power consumption as a function of time and confirm the adequacy of mathematical models. To do this, use a software package *Ships\_CPC* developed as part of the research state budget of «Concepts, technologies and areas of improvement ship power plants combined propulsive complexes» of the National University (Odessa Maritime Academy), which is a set of functional blocks of the components of SPP SPC built on a classic the principle of «input-output». For example, according to the block diagram in Fig. 3, the outputs of functional blocks PID-regulators MTDG dependent on given excitation voltage and speed, which in turn depends on the load on the power that corresponds to a moving boat or dynamically positioned, and the input (inputs) models PID-regulators the rotation frequency of T.

SPP SPC consists of 11 kV MSB, switchboards, 5 generators, 3 azimuthal T with variable speed and several *DOL (Direct On Line)* motors. The total installed capacity is 40 MW, while T capacity of  $3 \times 2.8$  MW is powered by frequency converters (FC) of 12-pulse topology. The maximum speed for azimuth thrusters 1000 RPM but in the scheme of the line of shafts are present lowering transmission between the engines and propellers of fixed pitch (PFP) but measurements taken directly from the line of shafts via inductive sensors that provide signals of rotational speed to *DP*-controller.

Simulations using the strategy of vector control and direct control point and power, as described in [5], and flowcharts shown in Fig. 3 and 4 are shown in Fig. 5, and corresponding consumption of T capacity – in Fig. 6.

The simulation results are compared with field measurements for type vessels Supply vessel which performs dynamic positioning. To measure the ship were only available mechanical power T, so the graphs depict modulated depending on electricity consumption and power loss in induction motors T. Temporary delays in the registration of measurement data can be explained by,

for example, in the same sequence of horizontal there are some differences between simulation and measurement. In other cases, of course, affect the results of tuning con-

trollers, especially the controller of rotational speed MTDG and T.

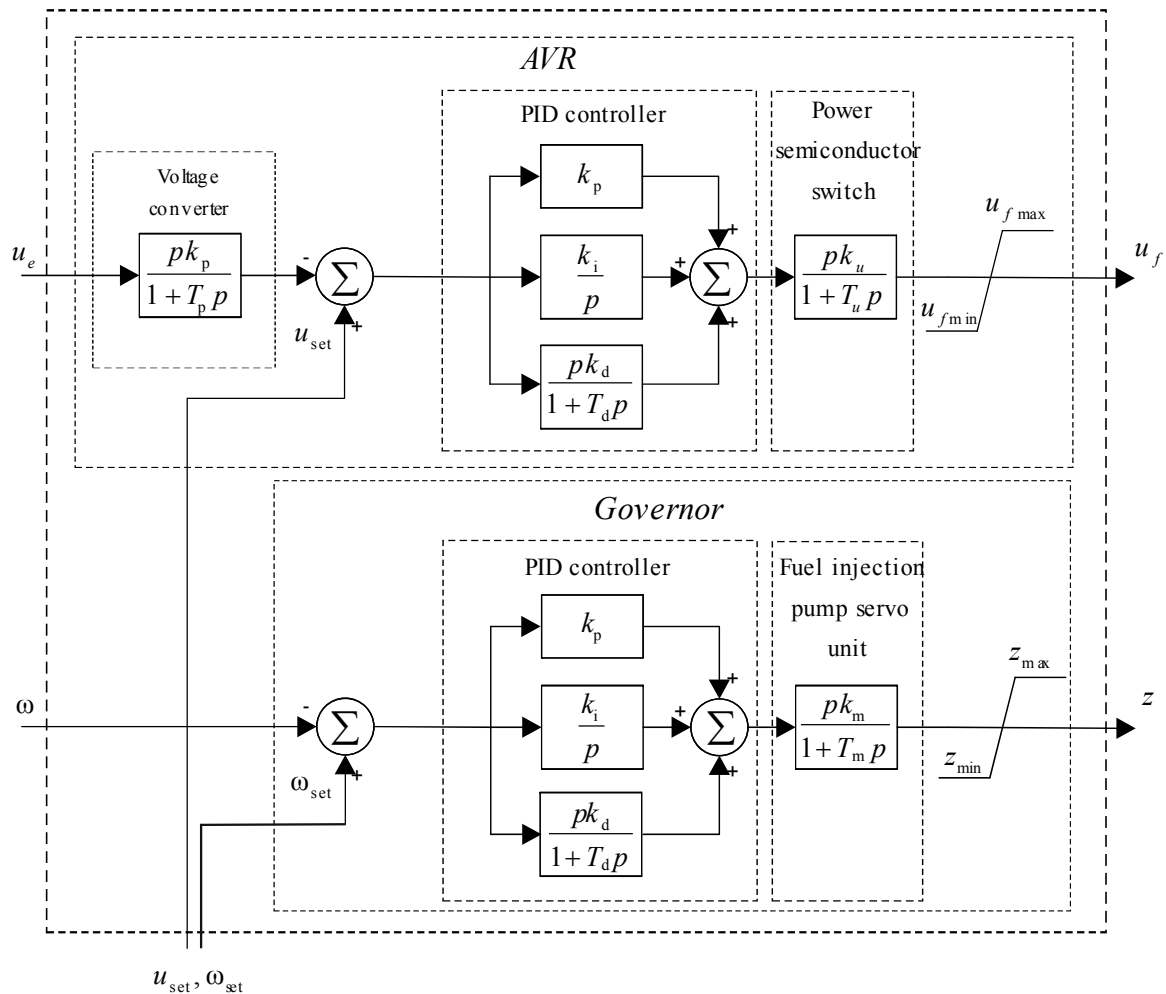


Fig. 4. Flowchart of the MTDG regulators:  $k_p, k_i, k_d, k_m, k_u$  – coefficients of proportional, integrating and differential units respectively, the converter voltage servomotor HPFP and PSS;  $T_p, T_i, T_d, T_p, T_m, T_u$  – time constants proportional, integrating and differential units respectively, the converter voltage servomotor HPFP and PSS

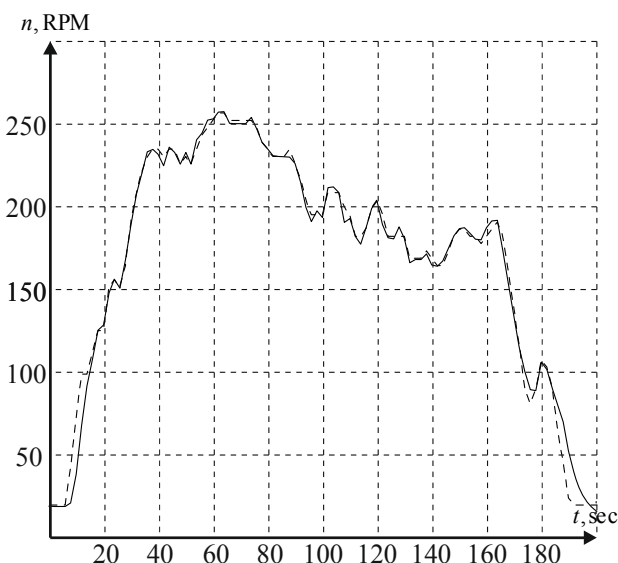


Fig. 5. Measured and modeled T rotation frequency dependencies: --- modelling, — measurement

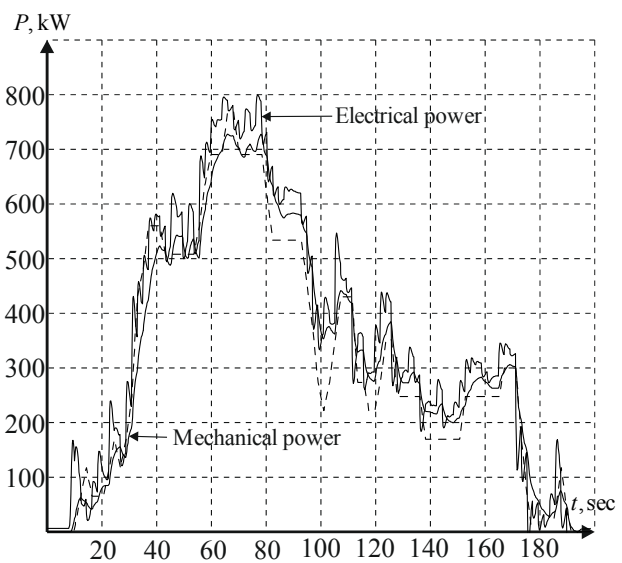


Fig. 6. Measured and modeled T consumption power dependencies: --- modelling, — simulation

Internal control loops T (torque, flux and current) are set out as the biggest gain in order to explore the process performance in regulating torque while maintaining the value stream as close to the nominal value for different load conditions.

#### Conclusions.

1. Appropriateness of comparative computer simulation in *MatLab Simulink* to build simulation models of objects based on their block diagrams and mathematical descriptions is defined.

2. In an environment *MatLab Simulink* optimization schemes mathematical models of MTDG and RPP SPC with screw- steering type Azipod are implemented installing the software complex *Ships\_CPC*, to reduce operating costs and improve fuel efficiency while loading restriction on the criterion of MTDG reduce wear and increase turn-around time.

3. The functional blocks of the proposed complex are basic structural units of RPP SPC models allowing them to investigate the normal and emergency operation modes.

Further studies will be conducted to establish the parameters of mathematical models AVR and frequency of MTDG in the environment *MatLab Simulink*. The method can be used to preselect the parameters of modern electronic controls. There will also be performed computer simulations of processes in the RPP SPC with different types of T at: the change of frequency of T rotation; the reverse; dynamic changes of emphasis propellers; failure of one T; changes of rowing propellers torque. The obtained results should reveal characteristic changes of basic parameters of RPP SPC at the relevant operation modes that will permit to consider investigated models adequate to real objects.

#### REFERENCES

1. Woud H.K., Stapersma D. *Design of propulsion and electric power generation systems*. IMarEST Publications, London, 2003. 494 p.
2. Budashko V.V., Onishchenko O.A. Improving management system combined thruster propulsion systems. *Bulletin of NTU «KhPI»*, 2014, no.38(1081), pp. 45-51. (Ukr).

#### How to cite this article:

Yushkov E.A. Modeling of operation modes of ship power plant of combined propulsion complex with control system based on electronic controllers. *Electrical engineering & electromechanics*, 2016, no.6, pp. 39-44. doi: 10.20998/2074-272X.2016.6.07.

3. Budashko V.V., Onishchenko O.A. Mathematical principles of simulation of power plant's control system at drillship. *Bulletin of Kamchatka State Technical University*, 2014, no.29, pp. 6-13. (Rus).
4. Hansen J.F. *Modelling and control of marine power systems*. Doktor ingeniør thesis, Trondheim, Norway, 2000. 119 p. Available at: [http://www.itk.ntnu.no/databaser/dr\\_ing\\_avhandling/vedlegg/110\\_pdf.pdf](http://www.itk.ntnu.no/databaser/dr_ing_avhandling/vedlegg/110_pdf.pdf) (accessed 21 September 2015).
5. Budashko V.V., Yushkov Y.A. Mathematic modeling of all-range controllers speed of thrusters for ship power plants in combined propulsion complexes. *Electronic Modeling*, 2015, vol.37, no.2, pp. 101-114. (Rus).
6. Glazeva O.V., Budashko V.V. Aspects of the mathematical modelling of the elements for Western Systems Coordinating Council of combined propulsion complexes. *Bulletin of NTU «KhPI». Series: Problems of Electrical Machines and Apparatus Perfection. The Theory and Practice*, 2015, no.42(1151), pp. 71-75. (Ukr).
7. Bojko A.A., Budashko V.V., Yushkov E.A., Bojko N.A. Synthesis and research of automatic balancing system of voltage converter fed induction motor currents. *Eastern-European Journal of Enterprise Technologies*, 2016, vol.1, no.2(79), pp. 22-34. doi: 10.15587/1729-4061.2016.60544.
8. Chernikh I.V. *SimPowerSystems: Modelirovanie elektrotekhnicheskikh ustroystv i sistem v Simulink* (SimPowerSystems: Modeling of electrotechnical devices and systems in Simulink). Available at: <http://matlab.exponenta.ru/simpower/book1/2.php> (accessed 01 October 2015). (Rus).
9. Tokarev L.N. [Automated regulation systems. Tutorial]. Saint Petersburg, Notabene Publ., 2001. 191 p. (Rus).

Received 09.05.2016

E.A. Yushkov, Postgraduate Student,  
Odessa National Maritime Academy,  
8, Didrikhson Str., Odessa, 65029,  
phone +38 048 7332367, e-mail: ushkov@te.net.ua

M.I. Baranov, S.V. Rudakov

## CALCULATION-EXPERIMENTAL METHOD OF RESEARCH IN A METALLIC CONDUCTOR WITH THE PULSE CURRENT OF ELECTRONIC WAVEPACKAGES AND DE BROGLIE ELECTRONIC HALF-WAVES

*Purpose. Development of calculation-experimental method for a discovery and study of electronic wavepackages (EWP) and of de Broglie electronic half-waves in a metallic conductor with the pulse axial-flow current of high density. Methodology. Theoretical bases of the electrical engineering, bases of quantum physics, electrophysics bases of technique of high voltage and large pulse currents, and also bases of technique of measuring of permanent and variable electric value. Results. On the basis of generalization of results of research of features of the longitudinal wave periodic distributing of negatively charged transmitters of electric current of conductivity in the thin round continuous zincked steel wire offered and approved in the conditions of high-voltage laboratory method for a discovery and direct determination in him of geometrical parameters of «hot» and «cold» longitudinal areas quantized periodic longitudinal EWP and accordingly the mediated determination of values of the quantized lengths formative their de Broglie electronic half-waves. It is shown that results of close quantum mechanical calculations of EWP and quantized lengths  $\lambda_{enz}/2$  of longitudinal de Broglie half-waves for the probed wire long  $l_0$  well comport with the results of the executed high temperature experiments on the powerful high-voltage generator of homopolar large pulse current of millisecond duration. Originality. First calculation-experimental a way the important for the theory of electricity fact of existence is set in a round metallic explorer with the impulsive axial-flow current of the quantized coherent de Broglie electronic half-waves, amplitudes of which at the quantum number of  $n=1,3,9$  correspond the middles of «hot» longitudinal areas of EWP. Calculation quantum mechanical correlation of type of  $\lambda_{enz}/2=l_0/n$  got experimental confirmation, in obedience to which on length of  $l_0$  conductor the integer of quantized electronic half-waves is always laid de Broglie. Practical value. The use of the offered method allows to expose electro-technological possibilities of practical application of features sharply not homogeneous periodic wave longitudinal distributing of drifting lone electrons and accordingly by them the conditioned thermal field in round metallic conductors with the electric axial-flow current of high-slay. References 21, figures 8.*

*Key words:* metallic conductor, pulse current, electronic wavepackage, de Broglie electronic half-wave, calculation-experimental investigation of electronic processes in the conductor.

*Описан расчетно-экспериментальный метод для обнаружения и изучения в электропроводящей макроструктуре металлического проводника с импульсным аксиальным током большой плотности квантованных (с квантовым числом  $n=1,2,3,\dots$ ) макроскопических «горячих» шириной  $\Delta z_{nh}$  и «холодных» шириной  $\Delta z_{nci}$  продольных участков, образующих шаг шириной  $(\Delta z_{nh} + \Delta z_{nci})$  периодически размещенных вдоль проводника квантованных продольных волновых электронных пакетов (ВЭП). Показано, что при протекании в круглом сплошном стальном оцинкованном проводе радиусом  $r_0=0,8$  мм и длиной  $l_0=320$  мм аperiodического импульса тока временной формы  $t_m/\tau_p \approx 9$  мс/160 мс с амплитудой его плотности  $\delta_{0m} \approx 0,37$  кА/мм<sup>2</sup> в исследуемом проводе стохастическим путем от одного протекания по нему указанного тока к другому возникают квантованные продольные ВЭП, имеющие один ( $n=1$ ), три ( $n=3$ ) и девять ( $n=9$ ) «горячих» продольных участков одинаковой ширины  $\Delta z_{nh}$ . Места расположения середин данных «горячих» продольных участков ВЭП шириной  $\Delta z_{nh} \approx 7$  мм вдоль провода соответствуют амплитудам распространяющихся вдоль него квантованных электронных полуволн де Бройля, характеризующихся в проведенных экспериментах квантовым числом  $n=1,3,9$  и квантованной длиной полуволны  $\lambda_{enz}/2 \approx l_0/n$ , равной 320, 107 и 34 мм соответственно. Полученные экспериментальные результаты соответствуют расчетным квантовомеханическим данным применительно к дрейфующим свободным электронам электропроводящего материала провода, базирующимся на фундаментальном соотношении неопределенности Гейзенберга и установленных закономерностях волнового продольного распределения в структуре провода этих электронов. Библи. 21, рис. 8.*

*Ключевые слова:* металлический проводник, импульсный ток, волновой электронный пакет, электронная полуволна де Бройля, расчетно-экспериментальное исследование электронных процессов в металле.

**Introduction.** In [1-9] presented the results of many years of theoretical and experimental studies to establish the basic laws of quantum mechanical wave longitudinal and radial distributions drift of free electrons in the non-magnetic metal circular solid cylindrical conductor of radius  $r_0$  and length  $l_0 \gg r_0$  in which longitudinally runs pulse axial current  $i_0(t)$  of arbitrary amplitude-time parameters (ATP). These results were obtained under the condition  $\Delta_i/r_0 \gg 1$ , where  $\Delta_i$  is the thickness of the skin layer of the current in the conductor, and its use in the averaged current density  $\delta_0(t) \approx i_0(t)/S_0$ , where  $S_0 = \pi r_0^2$  is

the cross section of mentioned conductor. The results obtained in [1-9] data show that in a homogeneous conductive metal conductor structure comprising quantum number  $n = 1,2,3,\dots$  of de Broglie electronic half-waves there are stochastic by longitudinal and radial quantized periodic electronic wavepackets (EWP) each of which contains one relatively «hot» and «cold» areas of the longitudinal or radial macroscopic dimensions. These sites give rise to a metal conductor macrostructure inhomogeneous temperature fields, periodically changing along its length

or radius. Moreover, the temperature levels in the «hot» and «cold» longitudinal sections conductor at the manifestation of it EWP may vary up to 3.5 times [4, 7]. The stochastic nature of the formation of the quantized data is determined by EWP quantized energy states of free electrons trapped in the microstructure of the conductor material at the time of supplying a voltage and start the flow of electric current through it or that kind [6]. We point out that the wave packets, resulting in the propagation of monochromatic electromagnetic waves in dielectric media, at one time have been described in the theory of electromagnetism and today electrophysics they studied well enough [10] as for the EWP metallic conductors with an electrical DC, AC and pulse current of different ATP formed in electrically conductive structures with their drifting free electrons as a result of the interference (superposition) of coherent electronic half-waves of de Broglie, they are currently in the theory of electricity are practically unexplored. That's why so far quantum-physical features of the spatial distribution of the main carriers of electricity in these structures - drift of free electrons, manifested most dramatically in the case of occurrence on them in regular (high-current discharges in circuits of high-voltage electrical installations [7, 11]), abnormal and emergency operating modes (overcurrent, short-circuit and direct linear lightning strikes [8, 12]) of high current density ( $10^8$  A/m<sup>2</sup> or more), and thus new areas of application in electrotechnology remain poorly understood. In this context, the development and practical use of new computational and experimental methods for the detection and study of quantized periodic EWP and quantized electronic half-waves of de Broglie in metal conductors with said electrical conduction current densities are actual scientific and technical problems.

**The goal of the paper** is development of computational and experimental method for the detection and study of quantized EWP and de Broglie electron half-waves in the metal conductor with a high density pulsed axial current.

**1. Problem definition of investigation of EWP and de Broglie electron half-waves in the metal conductor with pulse current.** Consider still housed outdoors straight round solid non-magnetic metallic conductor radius  $r_0$  and  $l_0 \gg r_0$  length. Let air environment parameters correspond to normal atmospheric conditions (air pressure is  $1.013 \cdot 10^5$  Pa and its temperature  $T_0$  is  $0^\circ\text{C}$  [10]), and the opposite ends of the conductor under consideration with the conductivity material  $\gamma_0$  its electrical potential difference is applied, in varying unipolarly time  $t$  by an arbitrary law. We suppose that on the test conductor cross-section  $S_0 = \pi r_0^2$  along its longitudinal axis takes pulse unipolar conduction current  $i_0(t)$  of amplitude  $I_{0m}$  characterized by the average density of  $\delta_0(t)$ . We restrict ourselves to the case for which the thickness of the skin layer of the current  $\Delta_i$  in the conductor material substantially greater than its radius  $r_0$ . For an approximate description of the behavior of drifting free conductor of electrons, as in [1-9], we use the well-known one-electron approximation, neglect their mutual influence on each

other, as well as the influence of the crystal lattice of the metal ion conductor on his itinerant electrons [10]. We adhere to the view that the longitudinal (radial) distribution of free electrons drifting in the test conductor subject to temporary Schrödinger wave equation, and according to their own quantized decisions [10]. It required on the basis of generalization obtained earlier in [1-9] quantum mechanical results concerning the electrical characteristics of the wave carrier distribution in the conduction current uniform conductive structures to formulate and test the in vitro methods to assess research EWP and electronic half-waves of de Broglie in thin circular metallic conductors with pulsed axial current  $i_0(t)$  aperiodic temporary shape and high density  $\delta_0(t)$ .

**2. A proposed method of detection in metal conductor with a pulse current of EWP and de Broglie electronic half-waves.** For clarity and better understanding of the problem under consideration electrophysical give first approximate quantum mechanical ratio for the smallest width  $\Delta z_{nh}$  «hot» longitudinal section through a conducting wire structure with pulsed axial current  $i_0(t)$  causing the appearance in it the average current density with amplitude  $\delta_{0m} \approx I_{0m}/S_0$  [7, 9]:

$$\Delta z_{nh} \approx e_0 n_{e0} h (m_e \delta_{0m})^{-1} [8 + (\pi - 2)^2]^{-1}, \quad (1)$$

where  $e_0 = 1.602 \cdot 10^{-19}$  C is the module of the electron electric charge [10];  $m_e = 9.109 \cdot 10^{-31}$  kg is the electron rest mass [10];  $n_{e0}$  is the average density of free electrons in the metal conductor to the test exposure to the electric current pulse [10];  $h = 6.626 \cdot 10^{-34}$  J·s is the Plank constant [10].

From (1) obtained using the fundamental Heisenberg uncertainty relation [10], it follows that the width of  $\Delta z_{nh}$  «hot» longitudinal portion of the conductor is practically determined by the numerical value of the amplitude of the pulse current density  $\delta_{0m}$  in his material. So, taking into account (1) for copper conductor ( $n_{e0} = 16.86 \cdot 10^{28}$  m<sup>-3</sup> [10]) at  $\delta_{0m} = 4 \cdot 10^6$  A/m<sup>2</sup> typical for normal operation of industrial electric alternating current networks [13], we find that it  $\Delta z_{nh}$  width is approximately equal to 0.53 m. At  $\delta_{0m} = 4 \cdot 10^8$  A/m<sup>2</sup> corresponding to the emergency mode of operation of industrial electric networks with the flow of their current distributors fault currents [13] or the normal operation of high-current circuits of high-voltage electro installations [11], the estimated width  $\Delta z_{nh}$  takes the numerical value of about 5.3 mm.  $\delta_{0m} = 4 \cdot 10^{11}$  A/m<sup>2</sup> which is characteristic for a quick electric explosion (EE) of thin metal wires [14] the width  $\Delta z_{nh}$  «hot» longitudinal section in a copper conductor according to (1) is numerically equal to about 5.3  $\mu\text{m}$ . Such microscopic value of  $\Delta z_{nh}$  is in good agreement with the linear dimensions of the conductive fine fractions resulting from EE (sublimation of conductive parts) of thin metal wires [11, 14]. In addition, according to [15] in the experimental study of the phenomenon of rapid EE in the air thin round copper wires 60 mm long and 100 mm in diameter by passing them from the high-voltage generator of pulse currents (GPC) sinusoidal decaying exponentially bit high density pulse current ( $\delta_{0m} \approx 6.4 \cdot 10^{12}$  A/m<sup>2</sup>) dispersed in the products the

explosive destruction of solid copper (in the «metal» plasma) by the high-speed photoregistration were fixed longitudinal periodic strata consisting of a layered disc-shaped longitudinal periodic structures of different luminosities, comprising alternating between a «light» in width  $\Delta z_h$  (34 pcs) and the «dark» width  $\Delta z_c$  (34 pcs) longitudinal sections. These areas formed in pairs in the discharge of said air gap with high-current circuit GPC «metallic» plasma step periodic structure EWP length about  $(\Delta z_h + \Delta z_c) \approx 1.76$  mm [11, 15]. One can reasonably assume that in the case of research [15] EV thin copper wires «light» longitudinal sections of the plasma «metal» products of the explosion in the discharge air gap correspond to «hot» areas of EWP, and their «dark» longitudinal sections - «cold» areas EWP. Experimental data from [15] indicate the accuracy of the quantum of provisions used in the basis of these estimations [1-9] of the wave distributions drift of free electrons and EWP respectively in thin metal conductors.

The above estimates indicate that identify in vitro particular longitudinal wave current distribution in the metal conductors can only mode transmission there through of DC, AC or pulse current  $i_0(t)$  which provide a flow in cross sections  $S_0$  of conductive material a relatively large current densities  $\delta_{0m}$ . According to the experimental data of [16] to the DC level of density in a thin galvanized steel wire ( $r_0=0.15$  mm;  $\Delta_0=5$   $\mu$ m is the thickness of the outer protective zinc coating) in an experimental study of its EWP is about  $6.8 \cdot 10^8$  A/m<sup>2</sup>. From own

experience in the study of quantized EWP and electronic half-waves of de Broglie in a thin circular galvanized steel wire ( $r_0=0.8$  mm;  $\Delta_0=5$   $\mu$ m) with aperiodic pulsed axial current  $i_0(t)$  millisecond duration in a research laboratory, equipped powerful high-voltage GPC to form a long-term load on the electric C- component of artificial lightning current [12], it follows that the values  $\delta_{0m}$  numerically equal about  $3.7 \cdot 10^8$  A/m<sup>2</sup> [3, 7].

In connection with the above, the proposed settlement and the experimental method of research in the macrostructure selected based on visualization of the expected electro manifestations (quantized longitudinal EWP and forming their electronic half-waves of de Broglie) metallic conductor with a pulsed axial current  $i_0(t)$  is based on the use of these quantum-physical laws and circuitry High discharge circuit of mentioned GPC-C shown in Fig. 1. As test samples (TS) of the conductor to be included as shown in Fig. 1 and 2 in the high-current high-voltage circuit GPC-C use the straight portions of commercially available galvanized steel wire ( $r_0=0.8$  mm;  $l_0=320$  mm;  $\Delta_0=5$   $\mu$ m;  $S_0=2.01$  mm<sup>2</sup>) [17]. The presence in such TS in a relatively thin coating of fusible and refractory enough massive wire base provides in its intensive local Joule heating (to temperatures of about 1500 °C) indirect detection by a sphere-like swelling on the cover of «hot» sections of longitudinal wires quantized longitudinal EWP and accordingly electronic de Broglie half-waves forming such EWP [7, 9].

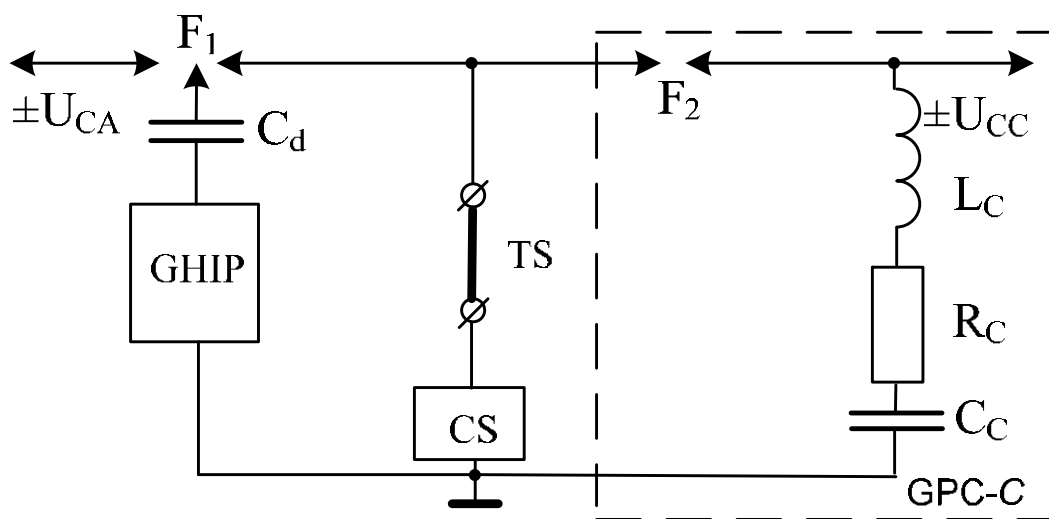


Fig. 1. Schematic diagram of high-current discharge circuit powerful high voltage GPC-C applied to the study of quantized periodic longitudinal VEP and electronic half-waves of de Broglie in the test piece of metal wire (GHIP – generator of high-voltage ignition pulses of amplitude up to  $\pm 100$  kV;  $F_1, F_2$  – respectively, three and two-electrode spark high air switches;  $C_d$  – dividing capacity of 180 pF and a pulse voltage up to  $\pm 120$  kV in the GHIP circuit controlling actuation air spark switches  $F_1$  and  $F_2$ ; TS – test sample of the metallic conductor; CS – coaxial shunt type IIIK-300 for measurement of pulse current in the conductor;  $\pm U_{CC}$  – charging voltage of capacitors GPC-C;  $\pm U_{CA}$  – charging voltage of capacitors of another GPC of existing artificial lightning current generator;  $L_C \approx 11.43$  mH,  $R_C \approx 4.74$   $\Omega$ ,  $C_C \approx 45.36$  mF – respectively, inductance, active resistance and capacitance of the discharge circuit of GPC-C)

Used a powerful single-module GPC-C at rated stores electric energy  $W_{C0}=567$  kJ arranged according to the scheme of Fig. 1 through 324 parallel-connected high-voltage pulse capacitors IM-5-140 (rated voltage  $U_0=\pm 5$

kV; nominal capacity  $C_0=140$   $\mu$ F) has the following own electrical parameters [12]:  $C_C \approx 45.36$  mF;  $R_C \approx 4.74$   $\Omega$ ;  $L_C \approx 11.43$  mH. Note that in the GPC-C was applied resistive protect it from accidental over-current capacitors

implemented by placing on their high conclusions permanent protective bulk graphite-ceramic resistors TBO-60-100  $\Omega$  [12, 18]. After charging to constant voltage  $U_{CC} \leq \pm 4.2$  kV capacitors GPC-C (at  $U_{CA}=0$ ) and the supply of high voltage generator of ignition pulses (GHIP) control microsecond pulse amplitude voltage of  $\pm 100$  kV high-voltage electrode is controlled three-electrode spark air switch  $F1$  cascade type hemispherical steel working

electrodes and the spacing length of 4 mm and 9 mm which is part of the present at the Scientific-&Research Planning-&Design Institute «Molnija» of the NTU «KhPI» artificial lightning current generator [12], due to the TS formed wire surge pulse occurs triggering high voltage two-electrode spark air switch  $F2$  rectangular graphite electrodes and insulating the working gap of 3 mm in length.



Fig. 2. General view of the continuous round galvanized steel wires ( $r_0=0.8$  mm;  $l_0=320$  mm;  $\Delta_0=5$   $\mu\text{m}$ ;  $S_0=2.01$   $\text{mm}^2$ ) included its ends by means of a bolted joint in high-power high-voltage discharge circuit GPC-C and placed on a thermal asbestos cloth, before subjecting it to an aperiodic pulse axial current  $i_0(t)$  of high density

As a result, through the TS wires will flow current pulse required ATP. ATP measurement pulse wires running through the TS current  $i_0(t)$  is performed using a digital storage oscilloscope Tektronix TDS 1012 and attorney metrological service measuring coaxial shunt (CS) ШК-300 type with its own internal resistance of 0.185 m $\Omega$  and fixable nano-, micro- and millisecond current pulse amplitude of 10 A to 200 kA [12], is included as shown in Fig. 1 nonpotential (grounded) part of the high-current discharge circuit GPC-C. We use CS at regular measurement in the discharge circuit GPC-C long aperiodic component of artificial lightning current conversion ratio was equal to approximately  $56.42 \cdot 10^2$  A/V [7, 12].

Fig. 3 shows the waveform of an aperiodic pulse of negative polarity in the discharge current circuit GPC-C if its TS instead of regular steel wire equivalent electrical load in the form of an aluminum sheet 2 mm thick and in terms 0.5 m  $\times$  0.5 m. It can be seen that when the amplitude of the module  $I_{0m} \approx 835$  A generated in this case ( $W_C \approx 400$  kJ;  $U_{CC} \approx -4.2$  kV) aperiodic pulse wave current time  $t_m/\tau_p \approx 9$  ms/160 ms ( $t_m$  is time corresponding  $I_{0m}$ ;  $\tau_p$  is the duration  $0.5I_{0m}$  current pulse level) is characterized by a complete duration  $t_0 \approx 1000$  ms and transfers in high-current discharge circuit GPC-C large electric charge, whose magnitude is approximately  $q_C \approx 191$  C.

Fig. 4 shows the negative polarity in the discharge circuit GPC-C waveform  $i_0(t)$  aperiodic current pulse in the presence of its TS investigated galvanized steel wire, losing at  $\geq 380$  ms its metallic conductivity due to intense local Joule heating and electro-thermal destruction of its structure.

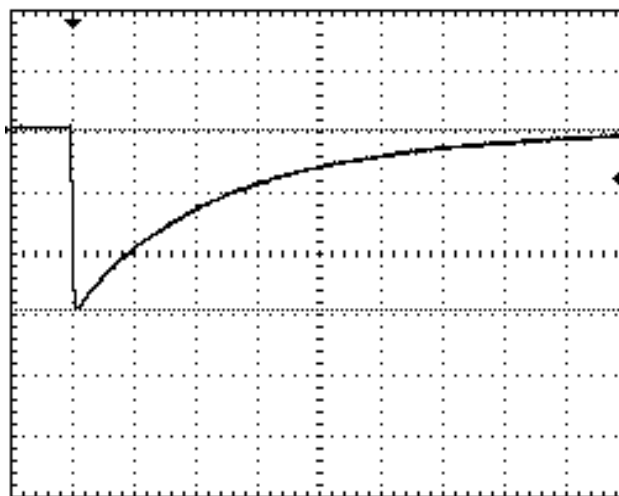


Fig. 3. Waveform of aperiodic current pulse  $i_0(t)$  negative polarity of temporary form  $t_m/\tau_p \approx 9$  ms/160 ms flowing in the discharge circuit GPC-C with the equivalent electrical load in the form of a flat aluminum plate of 2 mm thick and in terms 500 mm  $\times$  500 mm ( $W_C \approx 400$  kJ;  $U_{CC} \approx -4.2$  kV;  $I_{0m} \approx -835$  A;  $t_m \approx 9$  ms;  $\tau_p \approx 160$  ms;  $t_0 \approx 1000$  ms;  $q_C \approx -191$  C; the vertical scale - 282 A/cell; the horizontal scale - 100 ms/cell)

For this reason, the total duration of the flow in the wires of the TS aperiodic current pulse temporal shape  $t_m/\tau_p \approx 9$  ms/160 ms in our ongoing experiments did not exceed  $t_0 \approx 576$  ms. Note that the conductive structures IO wires with these TS use of current pulses is carried out under the terms of the required research the relationship between the variables  $\Delta_i$  and  $r_0$  [7]:  $\Delta_i/r_0 \approx 2r_0^{-1} [t_m/(\pi\mu_0\gamma_0)]^{1/2} \approx 42$ , where  $\mu_0 = 4\pi \cdot 10^{-7}$  H/m is the

magnetic constant [10] and  $\gamma_0 \approx 8 \cdot 10^6$  S/m is the conductivity base metal wires used in experiments [10]. Current waveform in Fig. 4 ( $W_C \approx 310$  kJ;  $U_{CC} \approx -3.7$  kV;  $I_{0m} \approx -745$  A) is a characteristic of all executed by us on GPC-C experiments intense Joule heating TS galvanized steel wire, caused by weak scattering in the crystal lattice of metal atoms it electronic half-waves of de Broglie [10, 19]. Averaged amplitude of the critical current density pulse  $i_0(t)$  as shown in Fig. 4 is not exceed  $\delta_{0m} \approx 0.37$  kA/mm<sup>2</sup>. The experiments on the GPC-C showed that when  $\delta_{0m} > 0.37$  kA/mm<sup>2</sup>, there is a complete sublimation of the electrically conductive material of the TS steel wire, eliminating any visual observations it EWP and electronic half-waves of de Broglie [7-9].

Fig. 5-7 show external views of the TS galvanized steel wire immediately after exposure to the high-current discharge circuit in the high-voltage GPC-C single aperiodic current pulse  $i_0(t)$  of negative polarity according to the Fig. 4 ( $U_{CC} \approx -3.7$  kV;  $I_{0m} \approx -745$  A;  $\delta_{0m} \approx 0.37$  kA/mm<sup>2</sup>).

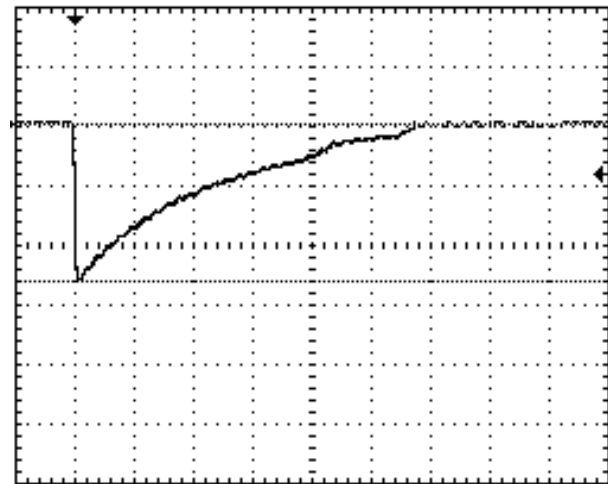


Fig. 4. Waveform of affecting the electrothermal locally destroyed analyzed straight round galvanized steel wire ( $r_0=0.8$  mm;  $l_0=320$  mm;  $\Delta_0=5$   $\mu$ m;  $S_0=2.01$  mm<sup>2</sup>) aperiodic pulse axial current  $i_0(t)$  negative polarity of temporary form  $t_m/\tau_p \approx 9$  ms/160 ms of high density ( $W_C \approx 310$  kJ;  $U_{CC} \approx -3.7$  kV;  $I_{0m} \approx -745$  A;  $\delta_{0m} \approx 0.37$  kA/mm<sup>2</sup>;  $t_m \approx 9$  ms;  $\tau_p \approx 160$  ms;  $t_0 \approx 576$  ms) (the vertical scale - 282 A/cell; the horizontal scale - 100 ms/cell)

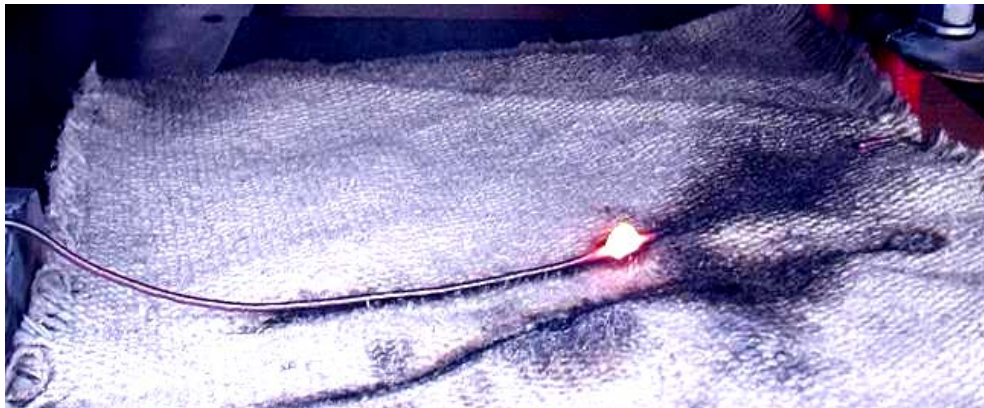


Fig. 5. External view of experimental distribution along the galvanized steel wire ( $r_0=0.8$  mm;  $l_0=320$  mm;  $\Delta_0=5$   $\mu$ m;  $S_0=2.01$  mm<sup>2</sup>) of cooling air and heatproof asbestos cloth macroscopic one «hot» (high-temperature zone width EWP  $\Delta z_{nh} \approx 7$  mm in the middle of the wire) and two extreme «cold» (width  $\Delta z_{nce} \approx 156.5$  mm at partial sublimation of one of them) longitudinal portions after flowing through it a current pulse aperiodic  $i_0(t)$  negative polarity temporary form  $t_m/\tau_p \approx 9$  ms/160 ms of high density ( $I_{0m} \approx -745$  A;  $\delta_{0m} \approx 0.37$  kA/mm<sup>2</sup>;  $n=1$ ;  $t_0 \approx 576$  ms) [20]



Fig. 6. External view of experimental distribution along the galvanized steel wire ( $r_0=0.8$  mm;  $l_0=320$  mm;  $\Delta_0=5$   $\mu$ m;  $S_0=2.01$  mm<sup>2</sup>) of cooling air and heatproof asbestos cloth macroscopic three «hot» (high-temperature zone width EWP  $\Delta z_{nh} \approx 7$  mm) and four «cold» (two extreme of width  $\Delta z_{nce} \approx 50$  mm at full sublimation of one of them and two internal of width  $\Delta z_{nci} \approx 100$  mm) longitudinal portions after flowing through it a current pulse aperiodic  $i_0(t)$  negative polarity temporary form  $t_m/\tau_p \approx 9$  ms/160 ms of high density ( $I_{0m} \approx -745$  A;  $\delta_{0m} \approx 0.37$  kA/mm<sup>2</sup>;  $n=3$ ;  $t_0 \approx 576$  ms) [20]

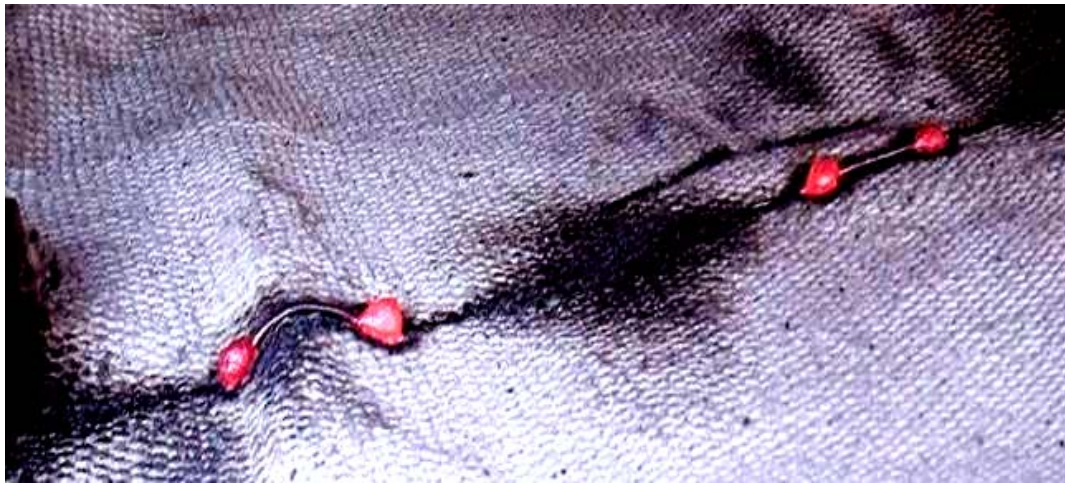


Fig. 7. External view of experimental distribution along the galvanized steel wire ( $r_0=0.8$  mm;  $l_0=320$  mm;  $\Delta_0=5$   $\mu\text{m}$ ;  $S_0=2.01$   $\text{mm}^2$ ) of cooling air and heatproof asbestos cloth macroscopic four «hot» (high-temperature zone width EWP  $\Delta z_{nh}\approx 7$  mm) and two internal «cold» (width  $\Delta z_{nci}\approx 27$  mm) longitudinal portions after flowing through it a current pulse aperiodic  $i_0(t)$  negative polarity temporary form  $t_m/\tau_p\approx 9$  ms/160 ms of high density ( $I_{0m}\approx -745$  A;  $\delta_{0m}\approx 0.37$  kA/mm<sup>2</sup>;  $n=9$ ;  $t_0\approx 576$  ms; the other five are «hot» and eight «cold» areas of the longitudinal wires have undergone complete sublimation) [20]

Thermal state of cooling air and heatproof asbestos cloth thickness 3 mm, made of chrysotile asbestos (its melting point is about 1500 °C [21]), the TS of the test wire indicates a partial sublimation of the electrically conductive structures (for zinc coating melting temperature is about 419 °C and the boiling point - 907 °C [10]; for the steel base, these temperatures are about 1535 and 2735 °C, respectively [10]) and the presence of a stochastic manner arising along the galvanized steel wire from one of said impulse current exposure to other meltblown brightly glowing sphere-like quantized «entities» the same in all cases, the width  $\Delta z_{nh}\approx 7$  mm.

The number of these «entities» in Fig. 5-7 corresponds to the quantum number  $n = 1, 3, 9$ . Between these sphere-like «formations» that have white-hot steel and, accordingly, the temperature of not less than 1200 °C [7, 16], located cylindrical «necks» in diameter  $2r_0=1.6$  mm and width of quantized  $\Delta z_{nc}$  with visually intact due to the pulsed heating zinc coating on them. Because of the heat indicated «necks», together with their surviving zinc coating acquired dark color.

Metallographic examination under an optical microscope МБС-9 type of cooled and carefully cleaned with a soft cloth cylindrical «isthmus» TS wires showed that they contain a uniform, shiny and adherent to a steel base wires zinc coating [7]. These experimental data indicate that the maximum heating temperature on cylindrical «isthmuses» TS wire does not exceed the melting temperature of the zinc coating (not more than 419 °C) [10]. With regard to the results of the survey on the optical microscope МБС-9, the cooled sphere-like «formations» TS wires inside them contained hardened fraction of the boiled and molten zinc coating steel wire base [7]. In this regard, the maximum heating temperature of the sphere-like «formations» TS wire is not less than the melting point of its steel base ( $\geq 1535$  °C [10]). This conclusion is confirmed by the fact that under all natural cooled air sphere-like «formations» TS wires occurred keyhole heat

cloth, made of chrysotile asbestos not less than 1500 °C with a melting point [21]. The above thermal results obtained with use of a powerful high-voltage GPC-C and line segments of thin galvanized steel wire high experiments indicate that the quantized sphere-like «formations» in the TS wires correspond to the «hot» longitudinal sections of its quantized periodic longitudinal EWP and cylindrical «necks» wire in the TS - «cold» longitudinal sections of these EWP.

For the case when  $n=1$  (Fig. 5), the quantized width  $\Delta z_{nxx}$  each of the two extremes of «cold» longitudinal sections of the EWP, the right of which was subjected to partial sublimation, in these experiments was found to be about 156.5 mm. The widths of these areas together with the wide  $\Delta z_{nh}\approx 7$  mm single «hot» longitudinal section EWP, located in the middle of the TS wire, according to those in [1-9] for the laws of EWP in a metallic conductor with an electrical conduction current form for the case  $n=1$  the length of the quantized  $\lambda_{enz}/2$  of one half-wave electronic de Broglie, numerically equal  $\lambda_{enz}/2\approx 2\Delta z_{nce}+\Delta z_{nh}\approx 320$  mm. The amplitude of this half-wave electronic de Broglie corresponds to the width of the middle  $\Delta z_{nh}$  «hot» longitudinal portion EWP. Obtained for  $n=1$  the experimental data for the quantized longitudinal EWP and electron de Broglie half-wave in the identity of the test wire is schematically illustrated in Fig. 8, a. From (1) at  $n_{e0}=16.82\cdot 10^{28}$  m<sup>-3</sup> [10] and  $\delta_{0m}=3.7\cdot 10^8$  A/m<sup>2</sup> we find that the estimated width of the «hot» longitudinal portion of said EWP in the test wire is about  $\Delta z_{nh}\approx 5.7$  mm. The estimated width of the quantum-mechanical assessment of the extreme «cold» longitudinal portion of the quantized longitudinal EWP in the test steel wire can be made according to the following analytical relationships [6]:

$$\Delta z_{nce}\approx l_0/(2n) - 0,5e_0n_{e0}h/(m_e\delta_{0m})[8 + (\pi - 2)^2]. \quad (2)$$

From (2) at  $n=1$ ,  $n_{e0}=16.82\cdot 10^{28}$  m<sup>-3</sup> and  $\delta_{0m}=3.7\cdot 10^8$  A/m<sup>2</sup> it follows that  $\Delta z_{nce}\approx 157.1$  mm. Then, for the calculated length  $\lambda_{enz}/2\approx 2\Delta z_{nce}+\Delta z_{nh}$  of electron half-wave

of de Broglie studied in the quantum case ( $n=1$ ) we have:  $\lambda_{enz}/2 \approx 2 \times 157.1 \text{ mm} + 5.7 \text{ mm} \approx 319.9 \text{ mm}$ . It can be seen that the results of experiments performed by high-quantum case  $n=1$  is fully correspond to the data of quantum-mechanical calculation of EWP in the studied steel galvanized wire.

For the case of  $n=3$  (Fig. 6)  $\Delta z_{nce}$  quantized width of each of the two extremes of «cold» longitudinal portions quantized longitudinal EWP, the left of which has undergone a complete sublimation is about 50 mm (if the width calculated by (2) 50.5 mm). Two internal «cold» longitu-

dinal sections located in this case between the neighboring «hot» sections of the longitudinal width  $\Delta z_{nh} \approx 7 \text{ mm}$ , had a quantized width  $\Delta z_{nci} \approx 100 \text{ mm}$ . It can be seen that the experimental width  $\Delta z_{nci}$  internal «cold» longitudinal sections twice the width  $\Delta z_{nce}$  experienced extreme «cold» longitudinal sections TS steel wire. Therefore, the quantum case  $n=3$ , the length of the quantized experienced  $\lambda_{enz}/2$  half-wave of de Broglie in TS wires will be numerically  $\lambda_{enz}/2 \approx \Delta z_{nci} + \Delta z_{nh} \approx 107 \text{ mm}$ . The experimental data obtained for the quantum case  $n=3$  is schematically shown in Fig. 8, *b*.

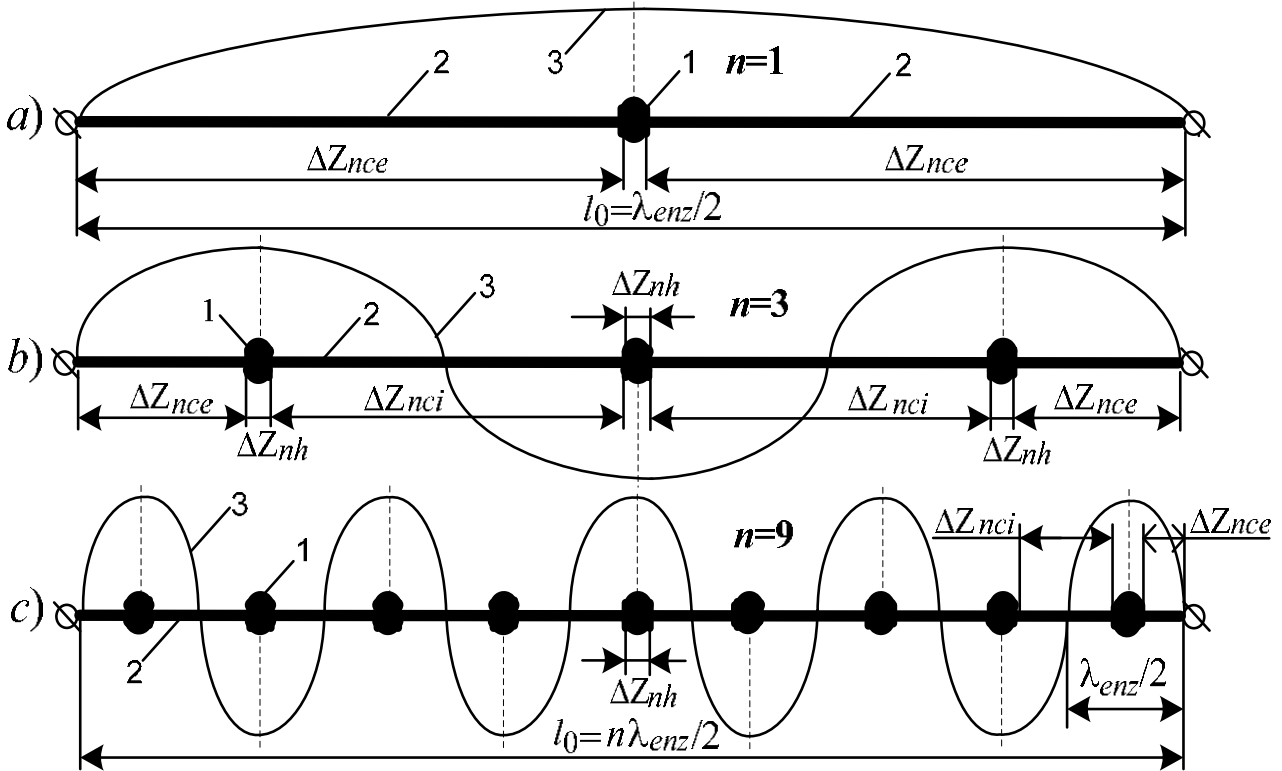


Fig. 8. Simplified schematic representation of the experimental data for the «hot» ( $\Delta z_{nh} \approx 7 \text{ mm}$ ) and «cold» longitudinal sections quantized periodic longitudinal EWP and electronic half-waves of de Broglie in TS round galvanized steel wire radius  $r_0=0.8 \text{ mm}$  and length  $l_0=320 \text{ mm}$  experiencing in the high-voltage high-current discharge circuit GPC-C single exposure time aperiodic pulse current form  $t_m/\tau_p \approx 9 \text{ ms}/160 \text{ ms}$  of high density  $\delta_{0m} \approx 0.37 \text{ kA/mm}^2$  (1 – «hot» EWP part; 2 – «cold» EWP part; 3 – electronic half-wave of de Broglie length  $\lambda_{enz}/2$ ; for *a* –  $n=1$  and  $\lambda_{enz}/2 \approx 320 \text{ mm}$ ; for *b* –  $n=3$  and  $\lambda_{enz}/2 \approx 107 \text{ mm}$ ; for *c* –  $n=9$  and  $\lambda_{enz}/2 \approx 34 \text{ mm}$ )

From the estimated settlement of (1) at  $n_{e0}=16.82 \cdot 10^{28} \text{ m}^{-3}$  and  $\delta_{0m}=3.7 \cdot 10^8 \text{ A/m}^2$  width  $\Delta z_{nh}$  «hot» longitudinal portion EWP follows that it is equal to about 5.7 mm. Settlement quantum mechanical estimate for  $n=3$  width  $\Delta z_{nci}$  internal «cold» longitudinal portion EWP in the test conductor will perform the analytical relation of the form [6]:

$$\Delta z_{nci} \approx l_0 / n - e_0 n_{e0} h (m_e \delta_{0m})^{-1} [8 + (\pi - 2)^2]^{-1}. \quad (3)$$

From (3) for  $n=3$ ,  $n_{e0}=16.82 \cdot 10^{28} \text{ m}^{-3}$  and  $\delta_{0m}=3.7 \cdot 10^8 \text{ A/m}^2$  we obtain that  $\Delta z_{nci} \approx 101 \text{ mm}$ . As a result, the estimated length  $\lambda_{enz}/2 \approx \Delta z_{nci} + \Delta z_{nh}$  electronic half-wave of de Broglie relation to the quantum case  $n=3$ , we find:  $\lambda_{enz}/2 \approx 101 \text{ mm} + 5.7 \text{ mm} \approx 106.7 \text{ mm}$ . Therefore, we can say that the experimental results on the GPC-C by indirect detection of a thin galvanized steel wire quantized longitudinal EWP and electronic de Broglie half-waves in

the quantum case  $n=3$ , and correlate well with the calculated data.

For quantum case  $n=9$  (Fig. 7) surviving «hot» EWP quantized longitudinal portions also had  $\Delta z_{nh} \approx 7 \text{ mm}$  width (the width when calculated according to (1) of 5.7 mm). Quantized width  $\Delta z_{nci}$  internal «cold» TS in the longitudinal wire portions in this case was about 27 mm (when calculated on the width (3) 29.8 mm). In this regard, the length of the quantized experienced  $\lambda_{enz}/2$  half-wave of de Broglie in TS galvanized steel wires for the quantum case  $n=9$  is approximately equal  $\lambda_{enz}/2 \approx \Delta z_{nci} + \Delta z_{nh} \approx 34 \text{ mm}$ . Fig. 8, *c* is illustrative in schematic form displayed corresponding experimental data for the TS considered in the case of quantum wires ( $n=9$ ). In this case, as in the cases with the quantum numbers  $n=1$  (see. Fig. 5) and  $n=3$  (see. Fig. 6), the middle «hot» longitudinal portions quantized

periodic EWP correspond to the amplitudes TS investigated cylindrical propagated in conductive structure wire quantized coherent electron de Broglie half-waves. In view of the above data for the calculated value for  $n=9$  length  $\lambda_{enz}/2$  electron de Broglie half-wave in the TS  $\lambda_{enz}/2 \approx 29.8 \text{ mm} + 5.7 \text{ mm} \approx 35.5 \text{ mm}$  wires we have:  $\lambda_{enz}/2 \approx 29.8 \text{ mm} + 5.7 \text{ mm} \approx 35.5 \text{ mm}$ . Therefore, we can say that in this quantum case ( $n=9$ ) experienced the results for the geometric parameters of the «hot» and «cold» longitudinal sections quantized periodic longitudinal EWP and accordingly the electronic half-waves of de Broglie in thin galvanized steel wire with aperiodic pulse current temporary form  $t_m/\tau_p \approx 9 \text{ ms}/160 \text{ ms}$  of high density ( $\delta_{0m} \approx 0.37 \text{ kA/mm}^2$ ) in the range of 4% in line with the relevant data submitted by us quantum mechanical calculation estimates for the basic geometric characteristics of EWP and de Broglie electron half-waves in the investigated steel wire.

### Conclusions.

1. The proposed and tested in a high-voltage laboratory of computational and experimental method for the detection and direct determination of geometric parameters (in particular, the widths  $\Delta z_{nh}$ ,  $\Delta z_{nce}$  и  $\Delta z_{nci}$ ) «hot» and «cold» longitudinal sections quantized periodic longitudinal EWP and thus indirectly determining the values of the quantized lengths  $\lambda_{enz}/2$  ( $n=1,2,3, \dots$ ) they form the electronic half-waves of de Broglie in a round galvanized steel wire ( $r_0=0.8 \text{ mm}$ ;  $l_0=320 \text{ mm}$ ;  $\Delta_0=5 \text{ }\mu\text{m}$ ;  $S_0=2.01 \text{ mm}^2$ ), which in a single operation from the one described in brief high-voltage high-power GPC-C developed at the Scientific-&Research Planning-&Design Institute «Molnaya» of the NTU «KhPI» unipolar momentum affects the axial current temporary form  $t_m/\tau_p \approx 9 \text{ ms}/160 \text{ ms}$  of large average density ( $\delta_{0m} \approx 0.37 \text{ kA/mm}^2$ ).

2. For the first time settlement and experimentally investigated for a round galvanized steel wires, is confirmed the important fundamentals of the theory of electricity electrophysical the fact that in this metal conductor used with aperiodic pulsed axial current conduction time form  $9 \text{ ms}/160 \text{ ms}$  and high density (about  $0.37 \text{ kA/mm}^2$ ) in the longitudinal direction extend quantized coherent electronic half-wave of de Broglie length  $\lambda_{enz}/2$  defined during the investigations by the quantum numbers  $n=1,3,9$ .

3. The interference of de Broglie electron half-waves gives rise to the conductive structure of the investigated steel galvanized wire quantized periodic longitudinal WEP macroscopic size, mid experimentally identical fixed widths  $\Delta z_{nh} \approx 7 \text{ mm}$  «hot» longitudinal sections which correspond to the amplitudes of these half-waves quantized electron de Broglie length in accordance with the established contact ratio  $\lambda_{enz}/2 \approx l_0/n$  with  $n=1,3,9$  in the 320, 107 and 34 mm, as well as an appearance in the macrostructure of the longitudinal wires inhomogeneous periodic temperature field with a temperature difference between its «hot» and «cold» longitudinal in about  $1000 \text{ }^\circ\text{C}$ .

### REFERENCES

1. Baranov M.I. Wave distribution of free electrons in conductor with electric current of the conductivities. *Russian Electrical engineering*, 2005, no.7, pp. 25-33. (Rus).

2. Baranov M.I. Energy and frequency specters of the free electrons conductor with electric current conduction. *Russian Electrical engineering*, 2006, no.7, pp. 29-34. (Rus).
3. Baranov M.I. New physical mechanisms and approaches in the study of the formation and distribution of the electric conduction current in the conductor. *Tekhnichna Elektrodynamika*, 2007, no.1, pp.13-19. (Rus).
4. Baranov M.I. Quantum-mechanical approach in the calculation of those temperature heating wire electric conduction current. *Tekhnichna Elektrodynamika*, 2007, no.5, pp. 14-19. (Rus).
5. Baranov M.I. Characteristic radial distribution of free electrons in a cylindrical conductor with varying electric current. *Tekhnichna Elektrodynamika*, 2009, no.1, pp. 6-11. (Rus).
6. Baranov M.I. Quantum-wave nature of electric current in a metallic conductor and some of its electrophysical macrophenomena. *Electrical engineering & electromechanics*, 2014, no.4, pp. 25-33. doi: 10.20998/2074-272X.2014.4.05.
7. Baranov M.I. Features heating thin bimetallic conductor large pulse current. *Elektrichestvo*, 2014, no.4, pp. 34-42. (Rus).
8. Baranov M.I. Local heating of electrical pathways of power electrical equipment under emergency conditions and overcurrents. *Russian Electrical Engineering*, 2014, vol.85, no.6, pp. 354-357. doi: 10.3103/s1068371214060030.
9. Baranov M.I. The main characteristics of the wave distribution of free electrons in a thin metallic conductor with a pulse current of high density. *Elektrichestvo*, 2015, no.10, pp. 20-32. (Rus).
10. Kuz'michev V.E. *Zakony i formuly fiziki* [Laws and formulas of physics]. Kiev, Naukova Dumka Publ., 1989. 864 p. (Rus).
11. Baranov M.I. *Izbrannyye voprosy elektrofiziki. Tom 3: Teoriya i praktika elektrofizicheskikh zadach* [Selected topics of Electrophysics. Vol. 3: Theory and practice of electrophysics tasks]. Kharkiv, Tochka Publ., 2014. 400 p. (Rus).
12. Baranov M.I., Koliushko G.M., Kravchenko V.I., Nedzel'skii O.S., Dnyshchenko V.N. A Current Generator of the Artificial Lightning for Full-Scale Tests of Engineering Objects. *Instruments and Experimental Technique*, 2008, no.3, pp. 401-405. doi: 10.1134/s0020441208030123.
13. Orlov I.N. *Elektrotehnicheskij spravochnik. Proizvodstvo i raspredelenie elektricheskoy energii. Tom 3, Kn. 1* [Electrical engineering handbook. Production and distribution of electric energy. Vol. 3, Book 1. Ed. I.N. Orlov]. Moscow, Energoatomizdat Publ., 1988. 880 p. (Rus).
14. Burtsev V.A., Kalinin N.V., Luchynskiy A.V. *Elektricheskij vzryv provodnikov i ego primeneniye v elektrofizicheskikh ustanovkakh* [Electric explosion of conductors and its application in electrophysical options]. Moscow, Energoatomizdat Publ., 1990. 288 p. (Rus).
15. Sobolev N.N. The study of electrical explosion of thin wires. *Journal of experimental and theoretical physics*, 1947, Vol.17, no.11, pp. 986-997. (Rus).
16. Marakhtanov M.K., Marakhtanov A.M. Periodical temperature changes along steel wire length caused by electrical current. *Herald of the Bauman Moscow State Technical University. Series Mechanical Engineering*, 2003, no.1, pp. 37-47. (Rus).
17. Belorussov N.I., Saakjan A.E., Jakovleva A.I. *Elektricheskie kabeli, provoda i shnury. Spravochnik* [Electrical cables, wires and cords. Directory]. Moscow, Energoatomizdat Publ., 1988. 536 p. (Rus).
18. Baranov M.I., Rudakov S.V. Development of new charts of capacitance-resistance defense of high-voltage capacitors of powerful capacity stores of energy from emergency currents. *Electrical engineering & electromechanics*, 2015, no.6, pp. 47-52. (Rus). doi: 10.20998/2074-272X.2015.6.08.

19. Baranov M.I. Strong and weak streaming free electron scattering in metallic conductor with electric conduction current. *Tekhnichna Elektrodynamika*, 2010, no.3, pp. 3-8. (Rus).

20. Baranov M.I. Theoretical and experimental results of research into explanation of de Broglie half-wave existence in the microstructure of an active metallic conductor. *Electrical engineering & electromechanics*, 2014, no.3, pp. 45-49. (Rus). doi: **10.20998/2074-272X.2014.3.09**.

21. Kuhlning H. *Spravochnik po fizike. Per. s nem.* [Dictionary on Physics. Translated from German]. Moscow, Mir Publ., 1982. 520 p. (Rus).

M.I. Baranov<sup>1</sup>, Doctor of Technical Science, Chief Researcher, S.V. Rudakov<sup>2</sup>, Candidate of Technical Science, Associate Professor,

<sup>1</sup> Scientific-&-Research Planning-&-Design Institute «Molniya», National Technical University «Kharkiv Polytechnic Institute», 47, Shevchenko Str., Kharkiv, 61013, Ukraine, phone +38 057 7076841, e-mail: eft@kpi.kharkov.ua

<sup>2</sup> National University of Civil Protection of Ukraine, 94, Chernyshevska Str., Kharkiv, 61023, Ukraine, phone +38 057 7073438, e-mail: serg\_73@i.ua

Received 01.06.2016

How to cite this article:

Baranov M.I., Rudakov S.V. Calculation-experimental method of research in a metallic conductor with the pulse current of electronic wavepackages and de Broglie electronic half-waves. *Electrical engineering & electromechanics*, 2016, no.6, pp. 45-53. doi: 10.20998/2074-272X.2016.6.08.

G.V. Bezprozvannykh, A.G. Kyessayev

## THE TECHNOLOGICAL AND EXPLOITATIVE FACTORS OF LOCAL INCREASE OF ELECTRIC FIELD STRENGTH IN THE POWER CABLE OF COAXIAL DESIGN

*Introduction.* Reliability of high voltage power cables in the process of long-term operation is largely due to the intensity of polymeric insulation aging. It is now established that the aging of polyethylene, which is the main material for the insulation of high voltage power cables, under the action of the electric field is determined primarily by the presence of structural heterogeneity arising both during cable production and during use. The cable is always there deviations from the ideal structure, which manifest in a deviation of diameters of conductors from nominal values; in the arrangement of the conductor and the insulation is not strictly coaxially and eccentrically; in elliptic (oval) core and insulation; change in relative dielectric constant and thickness of insulation on cable length force the formation of low molecular weight products (including water) in the flow at the manufacturing stage crosslinked polyethylene insulation and moisture during operation. Such defects are structural, technological and operational irregularities, which lead to a local change in the electric field. *Purpose.* Analysis of the influence of the eccentricity, elliptic and spherical inclusions in the electric field distribution in the power cable of a coaxial design with cross-linked polyethylene insulation, based on numerical simulation. *Methodology.* The bases of the numerical method of calculation of the electrical field strength are Fredholm integral equations of the first and second kind (method of secondary sources) for an axially symmetric field. Analysis of the influence of irregularities, including water treeing, the shape of the sounding signal is made using the method of discrete resistive circuit inductance and capacitance of substitution with the initial conditions. Solving systems of linear algebraic equations nodal analysis performed by the sweep method. *Results.* The presence of the eccentricity and ellipticity in the construction of cable has different effects on the distribution of the electrical field strength at the conductor and the insulation. The electrical field strength is increased by 50 % in the core and 17 % - on the surface of the insulation at 10 % eccentricity between conductor and insulation. Availability elliptic insulation leads to a redistribution of the electric field: field strength at the surface of the insulation is 2 times higher electric field strength on the surface of the conductor. Water treeing spherical shape filled with water with a dielectric constant of 6.9, lead to a local increase of electric field intensity is 5 - 10 times. *Originality.* Simulation results show that the presence of water treeing concentrated with individual heterogeneity characteristic impedance causes a change in shape and duration of the probe signal rectangular. *Practical value.* Time domain reflectometer can be considered as one of the promising methods for diagnosing operational irregularities (ellipticity, eccentricity, water treeing) in power cables. References 10, figures 12.

*Key words:* eccentricity, ellipticity of insulation, water treeing, electric field strength, the wave impedance, the probe pulse.

*На основе численного моделирования выполнен анализ влияния эксцентриситета между токопроводящей жилой и изоляцией, эллиптичности изоляции и включений сферической формы на распределение напряженности электро-статического поля в силовом кабеле коаксиальной конструкции со шиной полиэтиленовой изоляцией. Показано, что активный характер и высокие значения эффективной проводимости полупроводящих экранов не влияют на распределение поля между жилой и изоляцией. Наличие в толще изоляции водных включений сферической формы приводит к усилению электрического поля в 5 и более раз в зависимости от диэлектрической проницаемости. Водные трининги, как локальные сосредоточенные неоднородности в структуре полиэтиленовой изоляции, приводят к изменению формы зондирующего прямоугольного сигнала, распространяющегося в силовой кабельной линии, что дает возможность в эксплуатации диагностировать их с помощью импульсной рефлектометрии. Библиография 10, рис. 12.*

*Ключевые слова:* эксцентриситет, эллиптичность изоляции, водные трининги, напряженность электрического поля, волновое сопротивление, зондирующий импульс.

**Introduction.** Reliability of high voltage power cables in the process of long-term operation is largely due to the intensity of polymeric insulation aging. The high-voltage power cables under the effect of electric field aging of polyethylene is determined primarily by the presence of irregularities arising in the process of production of cables, as well as during operation. The cable is always there deviations from the ideal structure, which manifest in a deviation of diameters of conductors from nominal values; in the arrangement of the conductor and the insulation is not strictly coaxially and eccentrically; in elliptic (oval) core and insulation; change in relative dielectric constant and thickness of insulation on cable length force the formation of low molecular weight products (including water) in the flow at the manufacturing stage crosslinked polyethylene insulation and moisture during

operation. Such defects are structural, technological and operational irregularities, which lead to a local change in the electric field strength [1-3].

**The goal of the paper** is analysis of the influence of eccentricity, ellipticity and the spherical inclusions on the electric field distribution on the basis of the numerical simulation.

**Effect of semiconductive screens on the distribution of the electric field strength.** A feature of the construction of high-voltage cables with XLPE insulation semiconducting screens is the presence on the surface of the core and the surface of the insulation. Three layers - semiconducting coating on the core, insulation and semiconducting layer insulation - applied simultaneously per core using triple extrusion. As a result, air gaps between

© G.V. Bezprozvannykh, A.G. Kyessayev

the layers are not formed. In addition, the high conductivity of semiconducting layers of an electric field provides a bypass air gaps between the conductor and semiconductive coating on the core, between the semi-conductive coating on the insulation and the metal shield of the cable. The partial discharges in these gaps do not arise.

In [4] it is shown that the effective conductivity of the RC chain, replacing the semi-conductive layer is not capacitive but active. In this case it is 40 - 40,000 times higher than the conductivity of the capacitive layer with relative dielectric constant  $\epsilon=10$ . The effective dielectric constant of the semiconducting layers is about 400 - 400,000, which makes it possible to neglect their effect on the field distribution in the gap «conductive wire - metal screen» (Fig. 1).

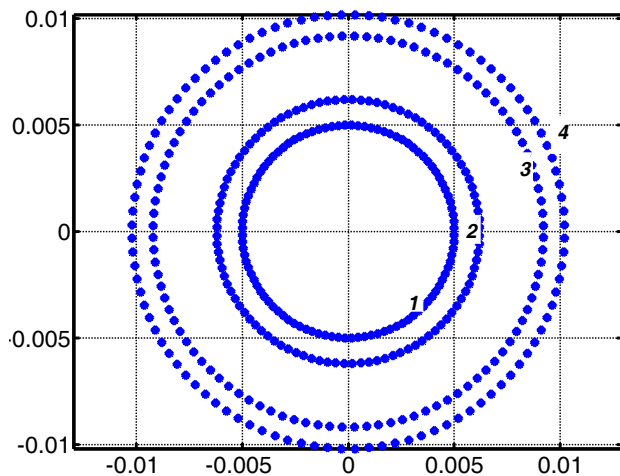


Fig. 1. The schematic arrangement of nodes on the surface of wire (1), semiconductive screen by wire (2), surface of the insulation (3), and semiconductive screen by insulation (4)

Fig. 2 shows the distribution of the line of tension along the boundaries between the media 1 - 4 (Fig. 2). When switching from the first layer (semiconductive coating cores) for the second (core insulation), the field strength increases abruptly in  $\epsilon_1/\epsilon_2$  times. In the transition from the second to the third layer (semi-conductive shield insulation) field strength abruptly decreases in  $\epsilon_3/\epsilon_2$  times [5]. The strength at the beginning of the third layer and the end of it (on the metal screen of the cable) is the same in magnitude but opposite in sign: the tension on the surface of the screen is taken negative, in contrast to the tension on the surface of the semiconductive screen by wire, which is assumed to be positive.

**Influence of eccentricity and ellipticity.** In the case of a homogeneous electric field in the insulation of the power cable coaxial design (Fig. 3) is nonuniform by thickness of insulation: the maximum on the conductor and the minimum at the surface of the cable insulation.

Presence of eccentricity  $\Delta Z$  between conductive wire and insulation leads to thickening ( $\Delta_1$ ) and thinning ( $\Delta_2$ ) insulation (Fig. 4) resulting in the distortion of electric field (Fig. 5, curve 2) on the surface of the wire ( $I$ ) and insulation ( $II$ ). The electric field intensity increases locally thinned areas and isolation areas in decreases thick-

ening, i.e. there is also the heterogeneity of distribution on the surface of the conductor and the insulation (curves 2). At eccentricity  $\Delta Z = 10\%$  of the radius of the conductor to tension in the core is increased by 20%, on the surface of the insulation - 25%. When eccentricity 100% of the diameter of the conductor coefficient of uneven distribution of the electric field strength equal to the ratio of electric field strength with eccentricity  $E_e$  to field without eccentricity  $E$  increases in 1.5 and 3 times on the surface of wire ( $K1$ ) and isolation ( $K2$ ), respectively (Fig. 6) [2].

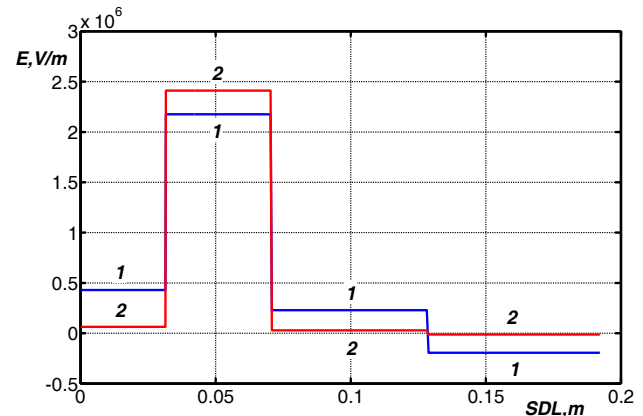


Fig. 2. The distribution of the electric field strength along the boundaries between the media 1 - 4 (Fig. 1) at different parameters of semiconducting layers: 1)  $\epsilon_1=\epsilon_3=15$ ; 2)  $\epsilon_1=\epsilon_3=150$ . The relative dielectric constant of the insulation  $\epsilon_2=2.3$

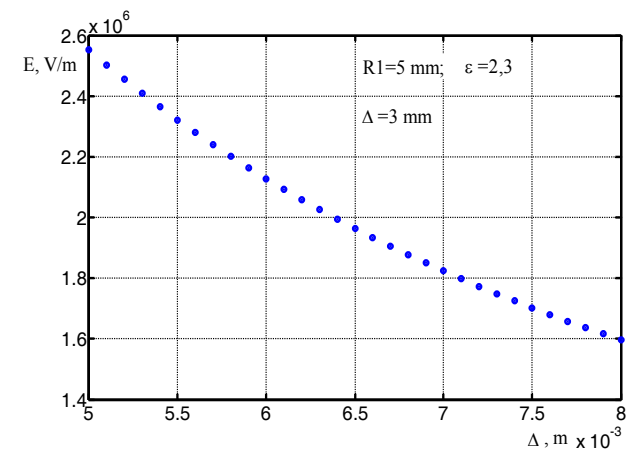


Fig. 3. The distribution of the electric field strength in the thickness of the homogeneous cross-linked polyethylene insulation in single-core high voltage power cables of perfect coaxial structure

The ellipticity (roundness) of insulation (Fig. 7) also leads to a distortion of the electric field on the surface of the conductor ( $I$ ) and insulation ( $II$ ): with ellipticity of 5% (curve 1) the field strength in the wire increases by 10%, on the surface of the insulation - 20%; with ellipticity of 11% (curve 2) by 30% and 45%; with ellipticity of 18% (curve 3) by 53% and 87%, respectively, relative to the field strength in a perfectly round cable design.

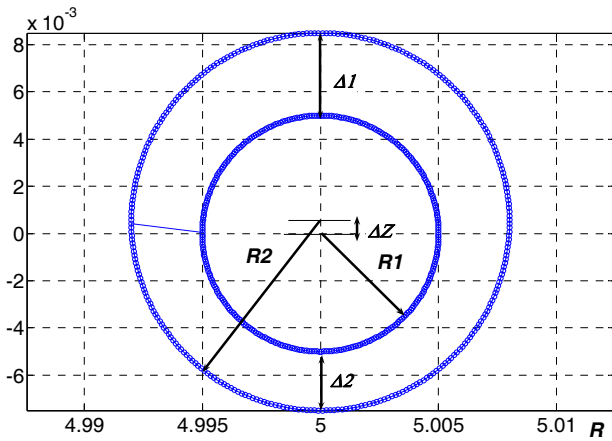


Fig. 4. The schematic arrangement of nodes in the calculation of the electric field strength in the power cable of coaxial design with eccentricity  $\Delta Z$  between wire and insulation

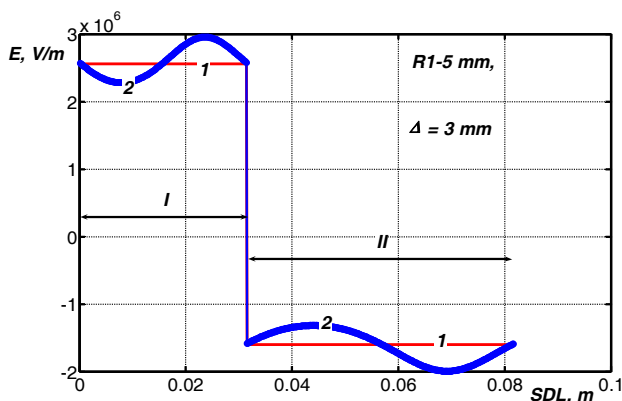


Fig. 5. The distribution of the electric field strength on the surface of the conductive wire and the insulation when absence (curve 1) and the presence of eccentricity  $\Delta Z=0,1R_1$  (curve 2) between the wire and insulation

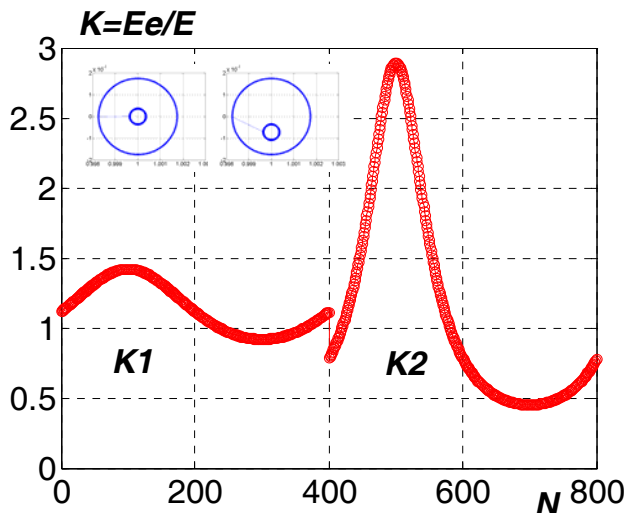


Fig. 6. Coefficient of uneven distribution of the electric field strength on the surface of wire ( $K_1$ ) and insulation ( $K_2$ ) at 100% eccentricity  $\Delta Z=R_1$

The presence of the eccentricity and ellipticity causes a change in wave resistance of the single-core power cable of coaxial design [1, 2]

$$\dot{Z}_w = \sqrt{\frac{R + j\omega L}{G + j\omega C}}, \quad (1)$$

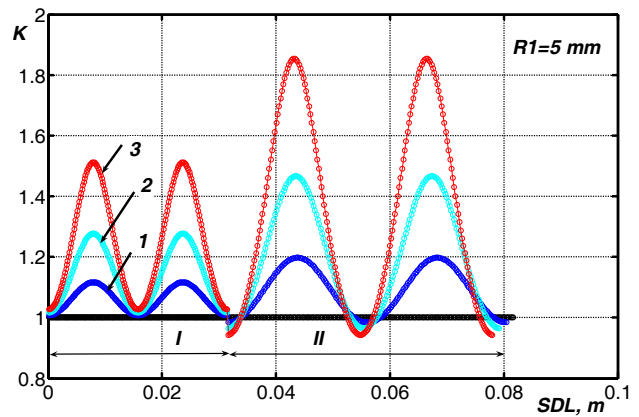


Fig. 7. Coefficient of uneven distribution of the electric field strength on the surface of the conductive wire ( $I$ ) and insulation ( $II$ ) in the presence of insulation ellipticity

where  $R$  is the total active resistance of the conductive wire and metal screen,  $\Omega/m$ ;  $L$  is the total inductance as a sum of internal inductance of the conductive wire and screen and mutual inductance (external),  $H/m$ ;  $G$  is the active conductance of insulation,  $S/m$ ;  $C$  is the cable capacitance,  $F/m$ ;  $\omega=2\pi f$  is the angular frequency,  $rad/s$ .

In the high frequency range for single-core power cables coaxial structure can assume that  $R \leq \omega L$  and  $G \leq \omega C$ . Then the wave resistance is active and is determined by the simplified formula

$$Z_w = \sqrt{L/C}. \quad (2)$$

Cable inductance in this range is determined by external inductance only [1]

$$L \cong L_{out} = \frac{\mu_0 \mu}{\pi} \ln \frac{R_2}{R_1}, \quad C = 2\pi \epsilon_0 \epsilon / \ln \frac{R_2}{R_1},$$

where  $\mu_0=4\pi \cdot 10^{-7}$  H/m is the magnetic constant,  $\epsilon_0=8.85 \cdot 10^{-12}$  F/m is the electric constant,  $\epsilon$  is the relative dielectric permittivity of the insulation material,  $\mu$  is the magnetic permeability of the conductive materials (for diamagnetics –copper and paramagnetics – aluminum  $\mu \approx 1$ ).

Fig. 8 shows the change in inductance, capacitance and wave resistance of the coaxial cable design with increasing eccentricity between conductive wire and insulation.

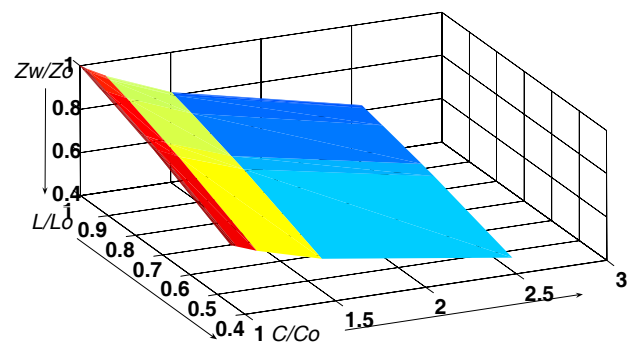


Fig. 8. Effect of eccentricity on the inductance, capacitance and wave resistance of the power cable of coaxial design (indexes «0» show parameters without eccentricity)

Having a thicker crosslinked polyethylene power cable insulation MV two water treeing spherical shape filled completely (Fig. 9, curve 1,  $\epsilon_2 = \epsilon_3 = 80$ ), [6], or partially (Fig. 9, curve 2,  $\epsilon_2 = \epsilon_3 = 6.9$ ) with water, leads to an increase in strength is 5 - 10 times or more. The basis of the numerical method of calculation of the field strength is Fredholm integral equations of the first and second kind (method of secondary sources) for an axisymmetric field [6].

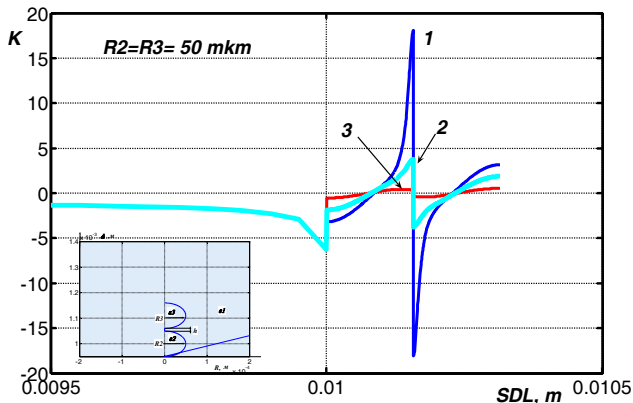


Fig. 9. The influence of the relative permittivity of two spherical inclusions of 100  $\mu\text{m}$  in diameter, spaced 2.5  $\mu\text{m}$  apart, by a factor of electric field inhomogeneity. The dielectric constant of polyethylene  $\epsilon_1 = 2.3$

At presence a thicker cross-linked polyethylene insulation of two spherical inclusions, filled with air (Fig. 9, curve 3,  $\epsilon_2 = \epsilon_3 = 1$ ), the electric field strength on the surface of the inclusions is less than the average value (2 kV/mm for medium voltage power cables).

**Influence of the electrical characteristics of the water treeings on the form of probe signals.** Degradation of high-power cables with cross-linked polyethylene insulation, laid in the ground, due to the formation of water treeing is a growing problem. Such tree structures - clusters [7-9] representing the number of water-filled microcavities with connecting channels, reduce the electric strength of the polymer insulation.

Water treeings (WT) lead to local concentration of electric field in the insulation of crosslinked polyethylene (see Fig. 9), the capacity increase, reduction of insulation resistance, increase of dielectric loss tangent. Thus, the numerical simulation of WT growth in power cables show [10] that the increase in capacity does not exceed 1.5% in the case of a single elliptical water treeing in full (100%) germination through the thickness of the insulation (from the metal screen to the conductor) regardless of the design screen performance. Insulation resistance at the same time significant changes: more than an order of magnitude. The result of this change in the insulation resistance is to increase the dissipation factor, conductance and insulation, eventually, decrease in cable impedance. Water treeing are local discontinuities in the structure of polyethylene insulation with wave resistance different from the wave resistance of the main part of the cable. At the distributing by cable high-frequency electromagnetic waves (probe signal - voltage certain of form and frequency) will

be observed from the reflection part inhomogeneities that lead to distortion of the (reflectometry in time-domain). To analyze the effect of water treeing in the form of concentrated defect with relevant electrophysical characteristics of the shape of the probe pulse the power cable represented in the form of T-shaped equivalent circuit (Fig. 10) [4]:  $R, L$  - resistance and inductance of the cable wires;  $C_0, R_0$  - geometrical capacity (capacity due to rapid polarization modes), and insulation resistance of the leak;  $R_1, C_1$  - parameters due to polarization processes in isolation. The number of units of the equivalent circuit to 1 meter for a correct representation of the cable must be large enough, depending on the operating frequency [4]. Thus, at 1 MHz - not less than 10. The cable is connected to a source of pulsed EMF  $E(t)$  with an internal resistance  $R_e$ . Resistances  $R_s$  and  $R_n$  - resistances of a source and the load respectively.

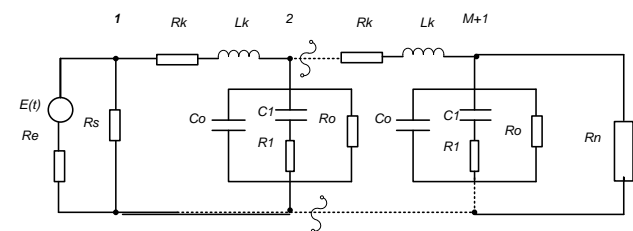


Fig. 10. T-shaped equivalent circuit of the power high-voltage cable of coaxial design [4]

To ensure a consistent mode of operation, excluding the appearance of additional reflected waves influencing the shape of the probe pulse, it is necessary that the equality of load impedances, source and cable impedance. For this purpose, at a frequency of 1 MHz, the measurements of the parameters of the sample single-core power cable length 25 cm АПВГ-1×95/16 for 35 kV with aluminum conductor section 95  $\text{mm}^2$  and copper screen section 16  $\text{mm}^2$ :  $R=0.3262 \Omega$ ;  $L=112 \text{ nH}$ ;  $C=36.3 \text{ pF/m}$ ;  $G = 0.7 \mu\text{S}$ ;  $\text{tg}\delta=2 \cdot 10^{-3}$ ;  $R_{ins}=10^{12} \Omega \cdot \text{m}$ .

Complex wave resistance determined by (1) is practically active:  $7.1906\text{e}+002 - 5.7684\text{e}+000\text{j}$ . The real part of 125 times the imaginary component. Wave impedance is 719  $\Omega$  module that significantly exceeds the typical values for coaxial cables construction: 93  $\Omega$ , 75  $\Omega$  and 50  $\Omega$ . Complex longitudinal resistance per unit length is  $(1.4480 + 0.0001\text{j}) \Omega/\text{m}$ : determining a real component due to the resistance contribution of the metallic screen (more than 10,000 times greater than the inductance component). Integrated transverse conductivity per unit length is equal to  $(2.8000\text{e}-006 + 4.5216\text{e}-008\text{j}) \text{ S/m}$ : the real part is more than 60 times the imaginary (capacitive) component. High values of conductance display screen processes semiconductive insulation and water-swellaable tape, and not in the cross-linked polyethylene insulation. The value of the wave resistance, determined according to the simplified formula (2) based on the inductance and capacitance of the cable is equal to 57.5  $\Omega$  (close to the value of 50  $\Omega$ )! For a correct simulation of the probing signal

propagation in the insulation of the power cable characteristic impedance is accepted equal to 57.5 Ω.

Measurement data cable parameters are used to determine the parameters of the T-link for a given number  $M$  and length  $l$  of the cable. The next step is to compile the equivalent circuit cable line method of discrete resistive circuit inductance and capacitance of substitution, taking into account the initial conditions. The next step is made a system of linear algebraic equations (SLAE) of nodal potential method [4]

$$\bar{G} \cdot \bar{\varphi} = \bar{J},$$

where  $\bar{G}$  is the tree-diagonal matrix of coefficients – own ( $G_{11}, G_{22}, \dots, G_{M+1, M+1}$ ) and mutual ( $G_{12}, G_{21}, \dots, G_{M, M+1}$ ) conductivities of branches

$$\begin{pmatrix} G_{11} & G_{12} & 0 & 0 & \dots & 0 \\ G_{21} & G_{22} & 0 & 0 & \dots & 0 \\ 0 & 0 & G_{32} & G_{33} & \dots & 0 \\ \dots & & & & \dots & 0 \\ 0 & 0 & 0 & 0 & G_{M+1, M+1} \end{pmatrix},$$

where  $\bar{\varphi}$  is the desired column matrix of nodal potentials,  $\bar{J}$  the column matrix of nodal currents.

SLAE is solved by the sweep method. currents are determined at each sampling step, flowing through the inductor and the voltage drop across the containers.

Numerical calculations are performed when connected to a pulsed source of EMF ( $E = 100$  V) power cable line length of 1 m at a frequency of 1 MHz. The duration of the sounding of the rectangular pulse is 4.0 ns. Resistances of the source and load are assumed equal to 57.5 Ω.

Fig. 11 shows the behavior of the shape and duration of the probing signal traveling along the cable line: curve 1 - cable with characteristic impedance of 57.5 Ω (measured parameters); curve 2 – cable with wave resistance 48 Ω (eccentricity between the conductor and insulation); curve 3 - cable with wave resistance of 60 Ω and the isolation parameters:  $R_{ms} = 10^{11}$  Ω·m,  $\text{tg}\delta = 2 \cdot 10^{-2}$  (water treeings). Area I is the beginning of the line, area II is the middle of the line. Influence of dielectric losses (imitation WT) on the shape of the probe pulse is shown in Fig. 12: curve 1 corresponds to  $\text{tg}\delta = 2 \cdot 10^{-4}$ ; curve 2 –  $\text{tg}\delta = 2 \cdot 10^{-3}$ ; curve 3 –  $\text{tg}\delta = 2 \cdot 10^{-1}$ .

### Conclusions.

The presence of the eccentricity and ellipticity in the construction of cable has different effects on the distribution of the electric field strength at the conductor and the insulation. When eccentricity between the wire and the insulation is 10 % of the radius of the core the field strength increases by 1.5 times in the wire and 1.17 times - on the surface of the insulation. The electric field strength on the surface of the insulation is doubled with respect to the strength on the tendon when roundness insulation.

The presence in the thicker crosslinked polyethylene insulation aqueous inclusions spherical shape leads to an increase in tension of 5-10 times the average value of

2 kV/mm in the high-voltage power cables. At such electric fields in the cross-linked polyethylene insulation threshold effects occur, in particular, the nonlinear dependence of the density of the current field, the dependence of the dielectric constant of the applied high voltage.

Simulation results show that the presence of water treeings as concentrated with individual heterogeneity characteristic impedance causes a change in shape and duration of the probe signal rectangular.

Time domain reflectometry can be considered as one of the promising methods for diagnosing operational irregularities (ellipticity, eccentricity, water treeing) in high-voltage power cables.

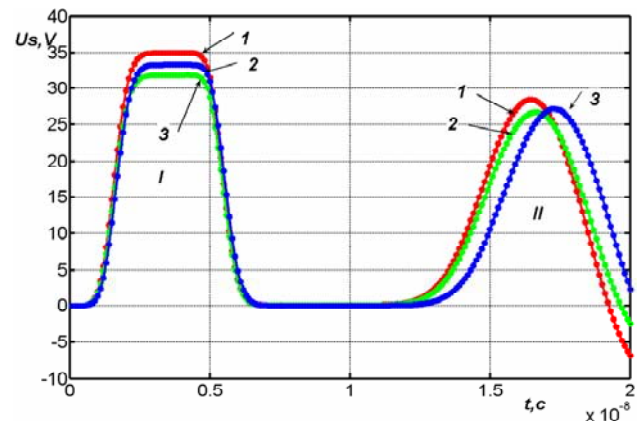


Fig. 11. Character of change of shape and duration probing signal traveling along the cable line in the presence of defects located at a distance  $\frac{1}{2}$  from the start line

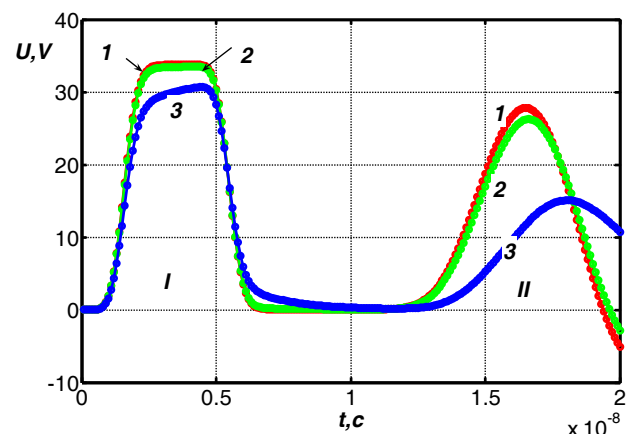


Fig. 12. Effect of dielectric losses due the presence of water treeings on the shape of the probe signal

### REFERENCES

1. Bezprozvannyh G.V., Boyko A.N., Kyessayev A.G. Influence of constructive and technological defects on coaxial radio-frequency cable impedance. *Electrical engineering & electromechanics*, 2013, no.2, pp. 57-61. (Ukr). doi: 10.20998/2074-272X.2013.2.11.
2. Kyessayev A.G. Impact on the transmission parameters eccentricity and ellipticity RF coaxial cables. *Bulletin of NTU «KhPI»*, 2013, no.59, pp. 62-69. (Ukr).
3. Shcherba A.A., Shcherba M.A. Modeling and analysis of the electric field in a dielectric medium, perturbed conductive microscopic inclusions of various sizes and configurations. *Tekhnichna Elektrodynamika*, 2010, no.6, pp. 3-9. (Rus).

4. Bezprozvannykh A.V., Naboka B.G. *Matematicheskie modeli i metody rascheta elektroizoljacionnyh konstrukcij* [Mathematical models and methods of calculation electrical insulation constructions]. Kharkov, NTU «KhPI» Publ., 2011. 92 p. (Rus).
5. Bezprozvannykh G.V., Naboka B.G., Moskvitin E.S. Substantiation of electrophysical characteristics of high-voltage power cable semiconducting screens with stitched insulation. *Electrical engineering & electromechanics*, 2010, no.3, pp. 44-47. (Rus). doi: **10.20998/2074-272X.2010.3.10**.
6. Bezprozvannykh A.V., Kyessayev A.G. Computing experiments for calculation of electrostatic axisymmetric field in piecewise-homogeneous insulation with spherical inclusions. *Electrical engineering & electromechanics*, 2014, no.5, pp. 67-72. (Rus). doi: **10.20998/2074-272X.2014.5.13**.
7. Dissado L.A., Hill, R.M. The fractal nature of the cluster model dielectric response functions. *Journal of Applied Physics*, 1989, vol.66, no.6, pp. 2511-2524. doi: **10.1063/1.344264**.
8. Chen Q., Burkes K., Makram E., Hadidi R., Xu X. Capacitance of Water Tree Modeling in Underground Cables. *Journal of Power and Energy Engineering*, 2014, vol.02, no.11, pp. 9-18. doi:**10.4236/jpee.2014.211002**.
9. Bezprozvannykh A.V., Kessaev A.G., Shcherba M.A. Frequency Dependence of Dielectric Loss Tangent on the Degree of Humidification of Polyethylene Cable Insulation *Tekhnichna Elektrodynamika*, 2016, no.3, pp. 18-24. (Rus).
10. Burkes K., Makram E., Hadidi R. Modeling the effect of a water tree inside tape shield and concentric neutral cables. *COMSOL Conference*, Boston, September 25, 2014. 8 p.

*Received 19.09.2016*

*G.V. Bezprozvannykh<sup>1</sup>, Doctor of Technical Science, Professor,  
A.G. Kyessayev<sup>1</sup>, Postgraduate Student,  
<sup>1</sup>National Technical University «Kharkiv Polytechnic Institute»,  
21, Kyrpychova Str., Kharkiv, 61002, Ukraine,  
phone +38 057 7076010,  
e-mail: bezprozvannykh@kpi.kharkov.ua*

*How to cite this article:*

Bezprozvannykh G.V., Kyessayev A.G. The technological and exploitative factors of local increase of electric field strength in the power cable of coaxial design. *Electrical engineering & electromechanics*, 2016, no.6, pp. 54-59. doi: 10.20998/2074-272X.2016.6.09.

I.V. Nizhevskiy, V.I. Nizhevskiy, V.E. Bondarenko

## THE EXPERIMENTAL VALIDATION OF THE GROUNDING DEVICE RESISTANCE MEASUREMENT METHOD

*Purpose.* The paper considers experimental research of three-electrode units for measuring the resistance of grounding devices for different purposes. *Methodology.* The experimental study of the method of resistance measurement of grounding devices for any design in any soil structure using the method of physical modeling is presented. *Results.* By results of model operation the set of equations of the sixth order is solved. It allowed to determine the own and mutual impedance in the three-electrode unit with high accuracy without searching the point of zero potential. *Features of measuring and defining the own and relative resistances of various combinations of electrodes for three-electrode measuring unit are considered. Originality.* The necessity of finding a zero potential point is excluded. *Practical value.* The proposed method provides the smallest possible spacing of potential electrodes outside the grounding devices. This reduces the wiring length measurement circuit in several times, increases the ratio «signal – noise», removes the restrictions on building of the territory outside the test grounding device. References 7, tables 10, figures 5.

*Key words:* experimental research, grounding device, the resistance measurement method, three-electrode unit, the method of physical modeling, experimental validation.

*Рассмотрены экспериментальные исследования трехэлектродной установки для измерения сопротивления заземляющих устройств различного назначения. На основе использования метода физического моделирования представлено экспериментальное обоснование метода измерения сопротивления заземляющего устройства любой конструкции в произвольной структуре грунта. По результатам моделирования решена система уравнений шестого порядка, что позволило определить собственные и взаимные сопротивления в трехэлектродной установке с достаточно высокой точностью и без отыскания точки нулевого потенциала. Библ. 7, табл. 10, рис. 5.*

*Ключевые слова:* экспериментальные исследования, заземляющее устройство, метод измерения сопротивления, трехэлектродная установка, метод физического моделирования, экспериментальное обоснование.

**Introduction and problem definition.** Currently, the three-electrode measuring device for measuring the resistance of grounding devices (GD) is widespread [1]. One of the main problems to be solved to get to this setting, sufficiently accurate results, is as specified in [2], the right choice of locations of measuring electrodes, i.e. such their arrangement in which the resistance of the measured value differs from its true value by not more than 10 % in either direction. However, in many cases (50 %) measuring the GD resistance for urban and industrial substations poses a serious problem to the present.

**Analysis of recent investigations and publications.** The problem of improving the accuracy of measurement of electrical parameters of the earth and GD are engaged many scientists both domestic and foreign.

Calculation method for determining the optimal position of the measuring electrodes in the measurement of GD resistance of large dimensions allowing to place the electrodes at short distances from the GD is described in [3]. However, it is noted that the calculations with the help of considered GD models have only limited application due to their external fields.

Analysis of Tagg methods for measurement of GD resistance given in [4] is shown that Tagg method is not suitable in soils with increasing of soil resistivity by depth.

The theoretical possibility of precise measurement of the GD resistance for each character of the soil heterogeneity and of any size and configuration of GD without the use of computer codes is noted in [5]. However, unfortunately, in this case it will be necessary to determine

the location of the potential electrode by finding the point of zero potential on-site measurements.

Mathematical modeling of the process of GD resistance measurement current of industrial frequency in multilayer soil is presented in [6] which describes an algorithm for calculating measurement errors at different locations of the measuring electrodes and an example of the construction of lines of equal errors for GD of complex shapes in a four ground. Unfortunately, as the authors note [6], choose a layout of electrodes, in which the measured GD resistance equals true, experimentally in measurements on the ground impossible.

In [7] the author provides a theoretical basis of a new method of GD resistance measurement with a three-electrode measuring setup with any character of soil heterogeneity, of any size and configuration of GD and the arbitrary placement of the measurement electrodes without finding the point of zero potential.

**The goal of the work** is the experimental validation of the method [7] for measurement of GD resistance by means of a three-electrode measuring unit without finding a point of zero potential.

**Experimental technique.** For the study models of GD in the form of discs of different diameters  $d1 = 10$  cm,  $d2 = 5$  cm,  $d3 = 9$  cm were accepted. The locations of GD in the electrolytic bath are shown in Fig. 1 and did not change in all experiments. The minimum distance between the edges of GD were  $a = b = c = 1$  cm. Several series of experiments were performed.

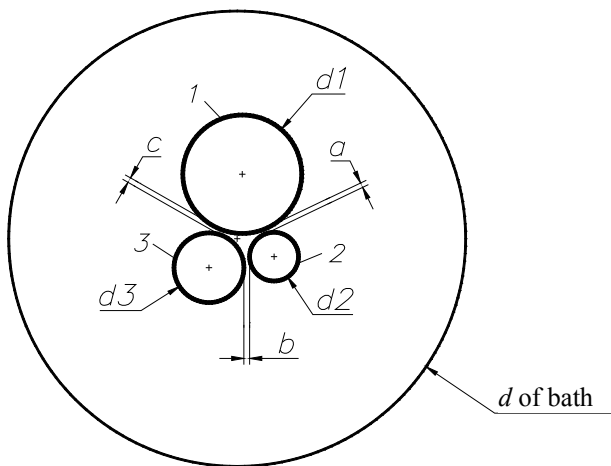


Fig. 1. Location of GD on the water surface in the electrolytic bath (plan view)

In the **first series** measurements of flowing from the GD current ( $I_{10}$ ,  $I_{20}$ ,  $I_{30}$ ) and voltage ( $U_{10}$ ,  $U_{20}$ ,  $U_{30}$ ) were performed to determine the internal resistance of GD, i.e. of each in its place in the absence of the others as shown in Fig. 2 for GD 1 and dashed to GD 2 and 3. The results of measurements and calculations of own GD ( $R_{10}$ ,  $R_{20}$  и  $R_{30}$ ) resistances are presented in Table 1.

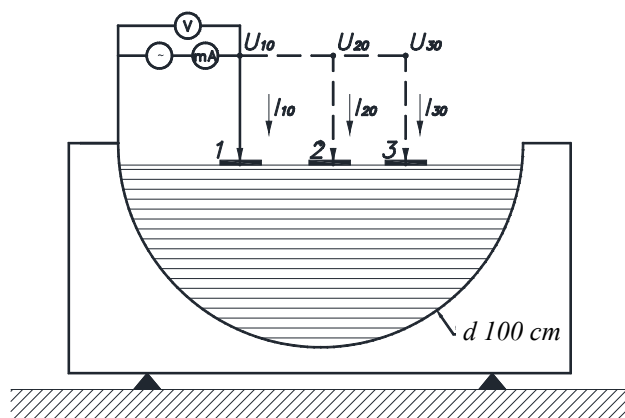


Fig. 2. Schematic layout of GD in the electrolytic bath (sectional view) and connection of devices for measurements

Table 1  
Results of measurements and calculations  
of own GD resistances

| GD No.             | 1             |              |                     | 2             |              |                     | 3             |              |                     |
|--------------------|---------------|--------------|---------------------|---------------|--------------|---------------------|---------------|--------------|---------------------|
| Measured parameter | $I_{10}$ , mA | $U_{10}$ , V | $R_{10}$ , $\Omega$ | $I_{20}$ , mA | $U_{20}$ , V | $R_{20}$ , $\Omega$ | $I_{30}$ , mA | $U_{30}$ , V | $R_{30}$ , $\Omega$ |
| Parameter value    | 159           | 8.63         | 54.28               | 84            | 8.8          | 104.76              | 146           | 8.65         | 59.246              |

The **second series** of experiments was carried out using the three GD. In this case, a source connected to the earth electrode 1 and the bath body, i.e., current is injected into the first GD. We conducted  $I_{10}$  current measuring circuit, the voltage on the grounding conductors 1, 2 and 3 with respect to the bath housing ( $U_{10}$ ,  $U_{20}$ ,  $U_{30}$ ), the voltage between grounding 1 and 2 ( $U_{12}$ ), GD between 1 and 3 ( $U_{13}$ ), and the GD 2 and 3 ( $U_{23}$ ) in the circuit shown in Fig. 3.

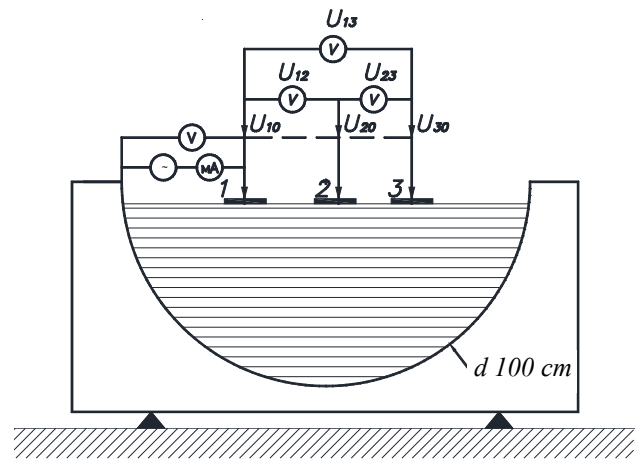


Fig. 3. Schematic layout of GD in the electrolytic bath (sectional view) and connection of devices for measurements

Similar measurements were made for cases source connection between the bath housing and the GD 2, and then GD 3. The results are shown in Table 2.

Table 2  
Results of measurements at the source connection  
between the bath body and GD

| Source input into GD 1 |                 | Source input into GD 2 |                 | Source input into GD 3 |                 |
|------------------------|-----------------|------------------------|-----------------|------------------------|-----------------|
| Measured parameter     | Parameter value | Measured parameter     | Parameter value | Measured parameter     | Parameter value |
| $I_{10}$ , mA          | 159.4           | $I_{20}$ , mA          | 82.1            | $I_{30}$ , mA          | 137.2           |
| $U_{10}$ , V           | 8.7             | $U_{20}$ , V           | 8.89            | $U_{30}$ , V           | 8.75            |
| $U_{12}$ , V           | 7.7             | $U_{12}$ , V           | 8.4             | $U_{12}$ , V           | 0.3             |
| $U_{13}$ , V           | 7.9             | $U_{13}$ , V           | 0.01            | $U_{13}$ , V           | 7.7             |
| $U_{23}$ , V           | 0.2             | $U_{23}$ , V           | 8.4             | $U_{23}$ , V           | 7.4             |

Then, studies were carried out in the **third series** with three GD without their connection with the bath. In this case the source is introduced between GD 1 and 2 as shown in Fig. 4. In this case, measured flowing in the current circuit  $I_{12}$  and the voltage between GD 1 and 2 ( $U_{12}$ ), between GD 1 and 3 ( $U_{13}$ ), between 2 and 3 ( $U_{23}$ ), and the voltage between each GD (1, 2 or 3) and the wall (casing) of bath, i.e.  $U_{10}$ ,  $U_{20}$  and  $U_{30}$  as shown in Fig. 4 for GD 3.

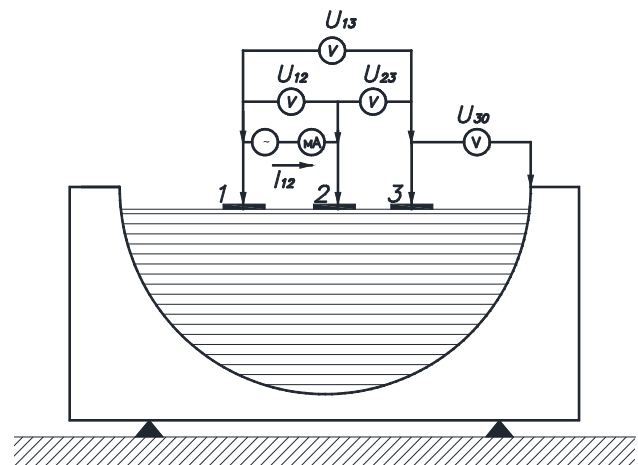


Fig. 4. Measurement circuit for three GD without their connection with bath housing

Similar measurements were made while entering the source between GD 2 and 3, and between GD 1 and 3. The results of these measurements are presented in Table 3.

Table 3

Results of measurements of GD parameters without source connection with bath housing

| Measured parameter | Source entering between GD 1 and 2 | Source entering between GD 1 and 3 | Source entering between GD 2 and 3 |
|--------------------|------------------------------------|------------------------------------|------------------------------------|
| $I_{12}$ , mA      | 70.4                               | –                                  | –                                  |
| $I_{13}$ , mA      | –                                  | 103.6                              | –                                  |
| $I_{23}$ , mA      | –                                  | –                                  | 70.1                               |
| $U_{12}$ , V       | 8.97                               | 4.175                              | 5.447                              |
| $U_{13}$ , V       | 3.27                               | 8.65                               | 3.05                               |
| $U_{23}$ , V       | 5.7                                | 4.475                              | 8.5                                |
| $U_{10}$ , V       | 2.34                               | 3.58                               | 0.65                               |
| $U_{20}$ , V       | 6.62                               | 0.6                                | 6.1                                |
| $U_{30}$ , V       | 0.94                               | 5.1                                | 2.4                                |

In the **fourth series** of experiments, measurements were made with two GD, i.e., in the absence of the third one and without their connection with bath housing. Sources include grounding between 1 and 2, as shown in Fig. 5. In this case, we measured flowing in the current circuit ( $I_{12}$ ), the voltage between the GD 1 and 2 ( $U_{12}$ ) and the voltage between the bath housing and GD 1 ( $U_{10}$ ), and between the bath housing and the GD 2 ( $U_{20}$ ).

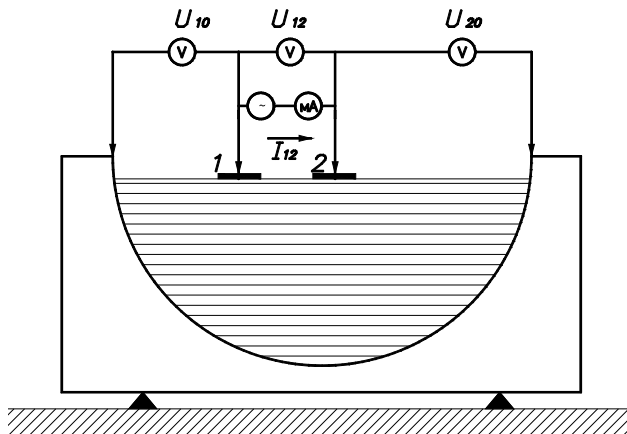


Fig. 5. Measurement circuit for two GD without their connection with bath housing

Similar measurements were made and when the source is turned on between the GD 1 and 3, and between the GD 2 and 3. The measurement results are shown in Table 4.

**Comparative analysis of the results of physical modeling of three-piece group of GD and the results of determination by the developed method of measuring own and mutual resistances of GD.** According to the results of experiments for the measurements of earth models derived parameters that are given in the Table 5. In this case, the definition of resistivity of the medium gives  $\rho = 12 \Omega \cdot \text{m}$ , i.e.  $\Delta R = 3.8 \Omega$  - the amendment to the final dimensions of the bath as determined by the formula for the hemisphere.

Table 4

Results of measurements for two GD without their connection with bath housing

| Measured parameter | Source entering between GD 1 and 2 | Source entering between GD 1 and 3 | Source entering between GD 2 and 3 |
|--------------------|------------------------------------|------------------------------------|------------------------------------|
| $I_{12}$ , mA      | 71.6                               | –                                  | –                                  |
| $I_{13}$ , mA      | –                                  | 105.3                              | –                                  |
| $I_{23}$ , mA      | –                                  | –                                  | 69.8                               |
| $U_{12}$ , V       | 8.9                                | –                                  | –                                  |
| $U_{13}$ , V       | –                                  | 8.8                                | –                                  |
| $U_{23}$ , V       | –                                  | –                                  | 8.8                                |
| $U_{10}$ , V       | 2.4                                | 3.7                                | –                                  |
| $U_{20}$ , V       | 6.5                                | –                                  | 6                                  |
| $U_{30}$ , V       | –                                  | 5.1                                | 2.8                                |

Table 5

Results of assessment of GD own resistances

| Determined parameter           | Own resistances, $\Omega$ |        |        |
|--------------------------------|---------------------------|--------|--------|
|                                | $R_1$                     | $R_2$  | $R_3$  |
| By Table 1                     | 54.28                     | 104.76 | 59.246 |
| Taking into account $\Delta R$ | 58.08                     | 108.56 | 63.046 |

The measurement results shown in Table 4 can determine the input resistance at the input source between GD, for example as 1 and 2, by the expression

$$R_{12\text{inp}} = U_{12} / I_{12} = 8.9 / 0.0716 = 124.3 \Omega.$$

Similarly we obtain  $R_{13\text{inp}}$  and  $R_{23\text{inp}}$ . Results are presented in Table 6.

Table 6

Results of assessment of GD input resistances for two GD without their connection with bath

| Determined parameter | Input resistances between GD, $\Omega$ |                    |                    |
|----------------------|--|--------------------|--------------------|
|                      | $R_{12\text{inp}}$                     | $R_{13\text{inp}}$ | $R_{23\text{inp}}$ |
| Parameter value      | 124.3                                  | 83.6               | 126                |

The obtained results for the input resistances (see Table 6) make it possible to determine the approximate values their own resistances of separate GD as follows. Measurements performed for the respective pairs of GD, i.e., input resistance between the GD (Table 6) allow us to write the following equations

$$\begin{aligned} R_1 + R_2 - 2R_{12} &= R_{12\text{inp}}; \\ R_1 + R_3 - 2R_{13} &= R_{13\text{inp}}; \\ R_2 + R_3 - 2R_{23} &= R_{23\text{inp}}. \end{aligned} \quad (1)$$

Neglecting (assumption) mutual resistances ( $R_{12}$ ,  $R_{13}$  and  $R_{23}$ ) within a couple and the influence of the third electrode we obtain a system of three equations with three unknowns. We carry out solution to this system, and the results of calculations of its own approximate values of GD resistances are summarized in Table 7.

Table 7

Approximate values of own GD resistances

| Determined parameter | Own resistances, $\Omega$ |       |       |
|----------------------|---------------------------|-------|-------|
|                      | $R_1$                     | $R_2$ | $R_3$ |
| Parameter value      | 40.95                     | 83.35 | 42.65 |

We calculate approximate values of the mutual resistances of the corresponding pairs of GD based on the fact

that the mutual resistance of two interacting GD resistance is always less than the least of them. [4] On the basis of the relation (1):

$$R_{12mut} = (R_1 + R_2 - R_{12imp})/2 = (58.08 + 108.56 - 124.3)/2 = 21.17 \Omega.$$

Similarly we obtain mutual resistances  $R_{13mut}$  and  $R_{23mut}$  and summarize results in Table 8.

Table 8  
Assessment of mutual resistances between corresponding GD couples

| Determined parameter | Mutual resistances between GD, $\Omega$ |             |             |
|----------------------|---|-------------|-------------|
|                      | $R_{12mut}$                             | $R_{13mut}$ | $R_{23mut}$ |
| Parameter value      | 21.17                                   | 18.79       | 22.8        |

The obtained approximate values of circuit parameters (see Table 7 and Table 8) according to the procedure described in [7] we input as initial values for the solutions of the system of six equations with six unknowns in which the right sides are represented by measurements shown in Table 3 as follows.

The results of voltages  $U_{13}$  and  $U_{23}$  and current  $I_{12}$  measurements at the input of the source between GD 1 and 2 allow to obtain input resistances:

$$R_{13A} = U_{13}/I_{12} = 46.45 \Omega;$$

$$R_{32A} = U_{23}/I_{12} = 81.1 \Omega.$$

Results of similar calculations for input of the source between GD 2 and 3, as well as D 1 and 3 are shown in Table 9.

Table 9  
Results of assessment of input resistances at the input of the source between corresponding GD

| Source connection         | Between GD 1 and 2 |           | Between GD 1 and 3 |           | Between GD 2 and 3 |           |
|---------------------------|--------------------|-----------|--------------------|-----------|--------------------|-----------|
|                           | $R_{13A}$          | $R_{32A}$ | $R_{12B}$          | $R_{32B}$ | $R_{12C}$          | $R_{13C}$ |
| Determined parameter      | $R_{13A}$          | $R_{32A}$ | $R_{12B}$          | $R_{32B}$ | $R_{12C}$          | $R_{13C}$ |
| Parameter value, $\Omega$ | 46.45              | 81.1      | 40.3               | 43.2      | 77.7               | 43.599    |

Results of solving the system of equations [7] by developed by the author program in MathCad packet are summarized in Table 10.

Table 10  
Assessment of discrepancies between calculated and experimental values of own and mutual GD resistances

| Parameter, $\Omega$ | $R_1$ | $R_2$  | $R_3$  | $R_{12}$ | $R_{13}$ | $R_{23}$ |
|---------------------|-------|--------|--------|----------|----------|----------|
| Initial value       | 40.95 | 83.35  | 42.65  | 21.17    | 18.79    | 22.8     |
| Calculation         | 60.42 | 98.43  | 62.39  | 20.62    | 17.56    | 22.74    |
| Experiment          | 58.08 | 108.56 | 63.046 | 21.17    | 18.79    | 22.8     |
| Discrepancy, %      | 4.04  | 9.33   | 1.03   | 2.57     | 6.5      | 0.2      |

Analyzing the data in Table 10 we conclude that the results of the calculations are in good agreement with the results of measurements obtained in the experiments. The discrepancy does not exceed 10 % which is a good result with acceptable error.

It should be noted that during the time of measurement, as the voltage source has been applied, the voltage change occurred almost negligible and can be neglected.

However, due to the processes taking place at the surface of the electrodes when the current flows the current change occurred more noticeable. This affects the results which are shown in Table 9 and Table 4, and it should be excluded.

Obviously, this can be attributed to the resulting discrepancy between calculated and experimental results. In the real world measurements, these differences should be significantly less. In all cases possible real conditions discrepancy can expect less than 10 %.

It should also be emphasized that the definition of the own and mutual GD resistances as the initial values was performed and the results of measurements in the three-element system (Table 3). The values obtained for GD own and mutual resistances have a slight difference from the similar values obtained for the respective pairs of GD in the absence of a third grounding (Table 4). Substitution of these values as the initial program for calculating own and mutual resistances of GD gives the same result as in Table 10. This important factor must be used when performing on-site measurements.

### Conclusions.

Firstly experimental investigation in the electrolytic bath at the NTU «KhPI» of a three-electrode unit for measuring the resistance of grounding devices for different purposes is carried out

On the basis of the method of physical modeling experimental validation of the method of resistance measurement of grounding devices of any design in any soil structure is presented.

By simulation results the system of the sixth-order equations is solved that allowed to determine own and mutual resistances in three-electrode unit with high accuracy and without finding a point of zero potential.

The proposed method provides the smallest possible spacing of the measuring electrodes outside the grounding devices. This is several times reduces the length of the connecting wires of the measuring circuit increases the ratio «signal - noise», removes the restrictions on the development of the territory outside the tested grounding device.

The obtained results showed that developed in [7] method provides fairly accurate results in all cases of measurements of resistance of grounding devices of electrical equipment.

### REFERENCES

1. *SOU 31.2-21677681-19:2009. Viprobuвання ta kontrol' pristroyiv zazemlennya elektroustanovok. Tipova instruktsiya* [SOU 31.2-21677681-19:2009. Test and control devices, electrical grounding. Standard instruction.]. Kyiv, Minenergovugillya Ukrainy Publ., 2010. 54 p. (Ukr).
2. Burgsdorf V.V., Yakobs A.I. *Zazemlyayushchie ustroystva elektroustanovok* [Grounding device of electrical installations]. Moscow, Energoatomizdat Publ., 1987. 400 p. (Rus).
3. Oslon A.B., Kostruba S.I. Measuring the resistance of large grounding devices. *Electrichestvo*, 2006, no.8. pp. 49-56. (Rus).
4. Oslon A.B. Tagg methods analysis for measuring grounding resistance. *III Rossiiskaia konferentsiia po zazemliayushchim ustroystvam: Sbornik dokladov* [3rd Russian Conf. on Grounding Devices: Collected Papers]. Novosibirsk, Russia, 27-31 October 2008, pp. 111-120. (Rus).
5. Oslon A.B., Tselebrovskii Iu.V. The intersection of the potential curves and the resistance of the grounding device *III Ros-*

siiskaia konferentsiia po zazemliaiushchim ustroistvam: Sbornik dokladov [3rd Russian Conf. on Grounding Devices: Collected Papers]. Novosibirsk, Russia, 27-31 October 2008, pp. 121-130. (Rus).

6. Oslon A.B., Kostruba S.I. Mathematical modeling of the process of grounding resistance measurement current of industrial frequency in multilayer soil. *Elektrichestvo*, 2008, no.5, pp. 12-17. (Rus).

7. Nizhevskiy I.V., Nizhevskiy V.I. A technique of measuring of resistance of a grounding device. *Electrical engineering & electromechanics*, 2016, no.3, pp. 50-57. (Rus). doi: **10.20998/2074-272X.2016.3.08**.

I.V. Nizhevskiy<sup>1</sup>, Engineer,

V.I. Nizhevskiy<sup>1</sup>, Candidate of Technical Science, Associate Professor,

V.E. Bondarenko<sup>1</sup>, Doctor of Technical Science, Professor,

<sup>1</sup>National Technical University «Kharkiv Polytechnic Institute», 21, Kyrpychova Str., Kharkiv, 61002, Ukraine, phone +38 057 7076977,

e-mail: victornizhevski@gmail.com

*Received 01.09.2016*

How to cite this article:

Nizhevskiy I.V., Nizhevskiy V.I., Bondarenko V.E. The experimental validation of the grounding device resistance measurement method. *Electrical engineering & electromechanics*, 2016, no.6, pp. 60-64. doi: 10.20998/2074-272X.2016.6.10.

Yu.L. Sayenko, D.N. Kalyuzhniy

## IDENTIFICATION OF GENERALIZED LINEAR LOAD IN THREE-PHASE THREE-WIRE NETWORK IN THE PROBLEM OF THE DISTRIBUTION OF ACTUAL CONTRIBUTIONS AT THE POINT OF COMMON COUPLING

*Purpose.* To perform structural and parametric identification of generalized load equivalent circuit of three-phase three-wire load in the network in the space of phase components. *Methodology.* Underlying structural identification methods are matrix analysis of electrical circuits. *Parametric identification* is based on the basic laws of electrical engineering. *Results.* The structure of a generalized load equivalent circuit is composed in three independent nodes. An approximate method for determining its parameters is proposed. The estimation error determination undistorted and distorted parts of the parameters of generalized load equivalent circuit. *Originality.* Approximate determination of equivalent circuit parameters are based on the results of a single measurement of voltages and phase currents. *Practical value.* The proposed replacement structure and a method for determining its parameters of the circuit can be used in the problem of the distribution of actual contributions at the point of common coupling. References 7, tables 1, figures 4.

*Key words:* equivalent circuit of linear generalized load, actual contribution, point of common coupling.

*На основе матричного метода анализа электрических цепей определена структура эквивалентной схемы замещения обобщенной нагрузки. Предложен способ приближенного определения параметров эквивалентной схемы замещения обобщенной нагрузки. Выполнен анализ ошибок приближенного определения параметров эквивалентной схемы замещения обобщенной нагрузки применительно к задаче распределения фактических вкладов в точке общего присоединения.* Библи. 7, табл. 1, рис. 4.

*Ключевые слова:* эквивалентная схема замещения линейной обобщенной нагрузки, фактический вклад, точка общего присоединения.

**Introduction.** The asymmetry and deviation of voltages is one of the main characteristics of electric power, which in most cases do not meet its quality [1]. Consequences of electrical consumption and lower quality of transmission power are well known [2], and, ultimately, to reduce financial losses [3]. Determination of the actual contributions to the reduction of electric power quality at the point of common coupling (PCC) is a solution of the problem of the distribution of compensation for economic loss to the injured party by all electricity market participants.

**Problem definition.** Existing methods for the distribution of actual contributions [4], irrespective of the implementation of the selected mathematical space, have a common problem. It is an adequate representation and parameterization of the generalized equivalent circuit load. So, in the space of generalized symmetrical components are load in the form of a set of current source or EMF with its resistance, which corresponds to the Norton or Thevenin equivalent circuits. In the space of phase components can restrict passive elements, where a clear opinion on the equivalent circuit of the structure in relation to the actual distribution of the contributions is not the problem. At asymmetrical load using the method of symmetrical components does not give any advantages over the phase space components. On this basis, the paper discusses the definition of the structure and parameters of equivalent circuit linear distorting the generalized three-phase three-wire load in networks within the space of phase components.

**The goal of investigations** is to develop an approach for generalized linear identification in three-phase three-wire load in the network within the space of phase components for task allocation of actual contributions to the current of common coupling.

**Results of investigations.** We consider the power supply system (PSS) with a dedicated load relatively PCC which made measurement of indicators of quality of electric energy (Fig. 1,a). We assume that all the elements of the electric power system and electric energy receivers generalized stress can cause only linear (sinusoidal) voltage distortion. Then, the equivalent circuit can be represented PSS such as active and passive elements connection (Fig. 1,b). In addition, we take the assumption of neglecting the mutual impedance and conductivity of individual PSS components.

According to the method of nodal potentials the total equivalent circuit of power system and the generalized load described by the following matrix equation:

$$\begin{bmatrix} Y_{aa} & Y_{ab} \\ Y_{ba} & Y_{bb} \end{bmatrix} \times \begin{bmatrix} \Phi_a \\ \Phi_b \end{bmatrix} = \begin{bmatrix} J_a \\ J_b \end{bmatrix}, \quad (1)$$

where  $a$  is the serial number of the last node from the side of the equivalent circuit of power system;  $b$  is the number of independent nodes in the overall equivalent scheme of the electric power system and the generalized load.

The solution of equation (1) relative the sub-matrix  $\vec{\Phi}_a$  in the absence of active elements in the equivalent circuit of the generalized load is as follows:

$$(Y_{aa} + Y_{eq}) \times \vec{\Phi}_a = \vec{J}_a, \quad (2)$$

where  $Y_{eq}$  is matrix of nodal conductivities of equivalent generalized load which characterizes the structure of its equivalent circuit.

The matrix  $Y_{eq}$  is determined as follows:

$$Y_{eq} = -Y_{ab} \times Y_{bb}^{-1} \times Y_{ba}. \quad (3)$$

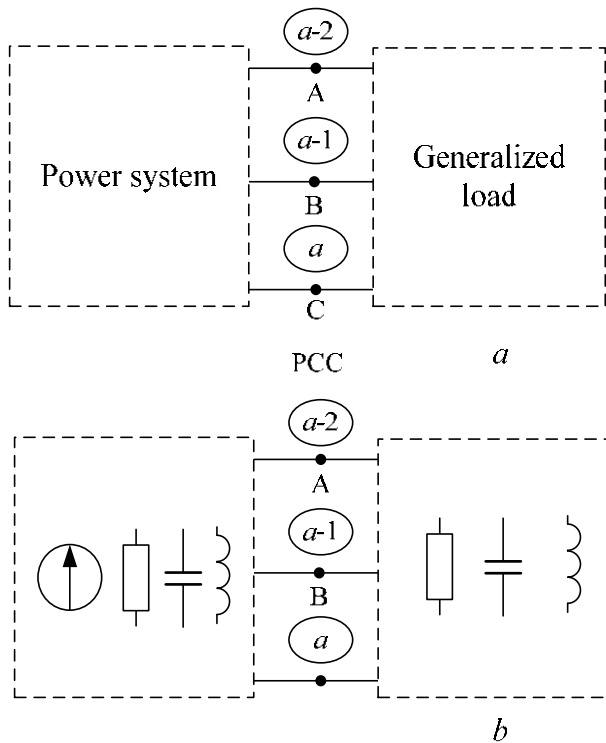


Fig. 1. Power supply system: *a* – structural circuit relative PCC; *b* – schematic diagram of the replacement of the power system and the generalized load

A feature of the matrix  $Y_{eq}$  in our case is that all the elements in it, except for the block elements of the dimension  $[3 \times 3]$ , zero. This implies that an equivalent substitution of generalized load circuit must have three independent nodes. This condition corresponds to the structure of the equivalent circuit shown in Fig. 2.

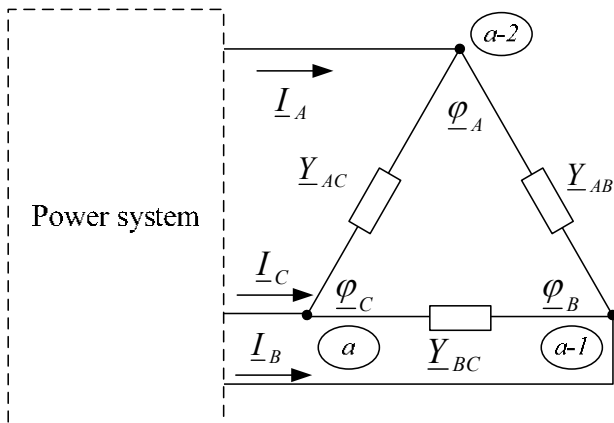


Fig. 2. Structure of the equivalent circuit of the generalized load

Let us consider a problem of the determination of the generalized load equivalent circuit parameters. Initial data are measured in the PCC phase currents ( $I_A$ ,  $I_B$  and  $I_C$ ) and linear voltages ( $U_{AB}$ ,  $U_{BC}$  and  $U_{AC}$ ).

Parameters of the equivalent circuit and measured mode parameters are interconnected as follows:

$$\begin{cases} U_{AB} \cdot Y_{AB} + 0 \cdot Y_{BC} + U_{AC} \cdot Y_{AC} = I_A; \\ U_{BA} \cdot Y_{AB} + U_{BC} \cdot Y_{BC} + 0 \cdot Y_{AC} = I_B. \end{cases} \quad (4)$$

The system (4) consisting of two linear algebraic equations and containing three unknowns ( $Y_{AB}$ ,  $Y_{BC}$  and  $Y_{AC}$ ) is uncertain and joint. Its general solution has the form

$$\begin{cases} Y_{AB} = (I_A - U_{AC} \cdot Y_{AC}) / U_{AB}; \\ Y_{BC} = -(I_C + U_{AC} \cdot Y_{AC}) / U_{BC}. \end{cases} \quad (5)$$

To determine unknown conductivities  $Y_{AB}$ ,  $Y_{BC}$  and  $Y_{AC}$  it is possible to resort to a redefinition of the system (5) by the use of two independent data, for example, successive measurements. Applying the least squares method to such a system of equations, unknown conductivity will be determined as follows:

$$\vec{Y} = (U^T U)^{-1} U^T \vec{I}, \quad (6)$$

где  $U$  is the matrix of measured voltages;  $\vec{I}$  is the column matrix of measured currents;  $\vec{Y}$  is the column matrix of unknown conductivities.

Using the above approach determine the unknown conductivities requires compliance with the following conditions. Measured parameters mode must display two different PSS condition caused by changes only from the electric power system. From a practical point of view, this situation is unlikely in PSS so many researchers, for example, [5, 6], propose to conduct active experiment based on forced switching capacitor banks in the PCC. Taking into account the method of measuring the parameters of electrical energy quality, where the minimum measurement interval mode settings begins with 0.2 s this approach is unacceptable. In addition, the results of mathematical modeling show high sensitivity of the solution (6) to minor changes in the state of generalized load, as well as the magnitude of the disturbance from the power system. As a consequence, an adequate definition of the equivalent circuit parameters of the generalized load according to the expression (6) in a real operation is not technically feasible.

We consider the possibility of determining the approximate equivalent circuit parameters of the generalized load. For this purpose, we turn to its equivalent circuit represented as a star connection of elements (Fig. 3).

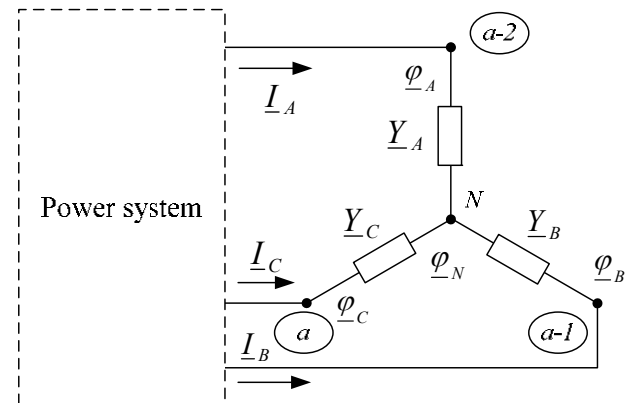


Fig. 3. Equivalent circuit of the generalized load with star connection of elements

The considered equivalent circuit with four nodes is the described by the following system of three equations:

$$\begin{cases} \underline{U}_A \cdot \underline{Y}_A = \underline{I}_A; \\ \underline{U}_B \cdot \underline{Y}_B = \underline{I}_B; \\ \underline{U}_C \cdot \underline{Y}_C = \underline{I}_C. \end{cases} \quad (7)$$

As it is known, an accurate measurement of the phase voltages of three-phase three-wire in the networks due to a physical lack of a neutral point, generally can not be performed. Therefore, for an approximate determination of the phase voltages use the measured values of the line voltages:

$$\begin{cases} \underline{U}_A^{\approx} = (\underline{U}_{AB1} \cdot e^{-j30} + \underline{U}_{AB2} \cdot e^{j30}) / \sqrt{3}; \\ \underline{U}_B^{\approx} = \underline{U}_{BA} + \underline{U}_A^{\approx}; \\ \underline{U}_C^{\approx} = \underline{U}_{CB} + \underline{U}_B^{\approx}, \end{cases} \quad (8)$$

where  $\underline{U}_{AB1}$  and  $\underline{U}_{AB2}$  are the linear voltages of direct and inverse sequences, respectively.

The error of the determination of phase voltages for the equivalent circuit of Fig. 3 will be determined by the difference of exact  $\varphi_N$  and approximate  $(\underline{U}_A^{\approx} + \underline{U}_B^{\approx} + \underline{U}_C^{\approx})/3$  values of potentials of the point  $N$  (Fig. 4):

$$\Delta\varphi = \varphi_N - (\underline{U}_A^{\approx} + \underline{U}_B^{\approx} + \underline{U}_C^{\approx})/3. \quad (9)$$

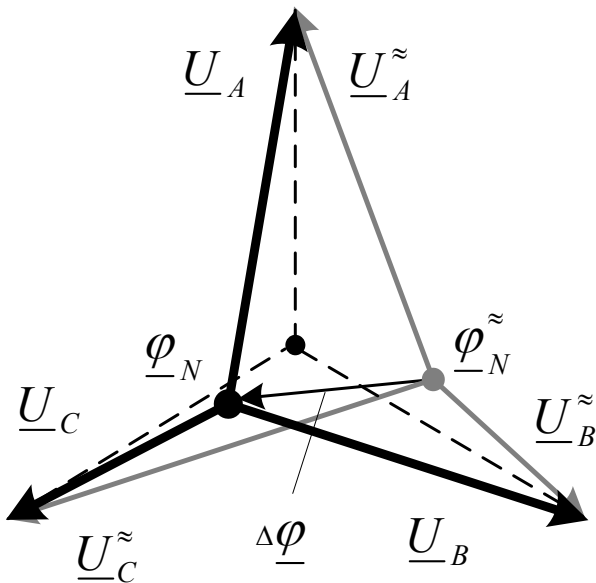


Fig. 4. Exact and approximate values of phase voltages for the equivalent circuit of the generalized load with star connection of elements (Fig. 3)

So, approximate values of conductivities  $\underline{Y}_A^{\approx}$ ,  $\underline{Y}_B^{\approx}$  and  $\underline{Y}_C^{\approx}$ , calculated by (7) taking into account (8) connected with their exact values by the following equality:

$$\underline{Y}_{ph}^{\approx} = \underline{Y}_{ph} - \underline{Y}_{ph} \cdot \Delta\varphi / \underline{U}_{ph}^{\approx}, \quad (10)$$

where the symbol "ph" corresponds to phase A, B or C.

To solve the problem of the distribution of phase values the basic is dividing of the equivalent circuit into

nondisturbing and disturbing parts. Here, from the point of view of phase conductivities determination, the most sensitive for this dividing are *nondisturbing* and *disturbing* parts used for the phase values determination by the voltage asymmetry:

$$\begin{cases} \underline{Y}_{ph}^{nondis} = (\underline{Y}_A + \underline{Y}_B + \underline{Y}_C) / 3; \\ \underline{Y}_{ph}^{dis} = \underline{Y}_{ph} - \underline{Y}_{ph}^{nondis}. \end{cases} \quad (11)$$

From here, we conduct analysis of error of determination of nondisturbing and disturbing parts of the generalized load equivalent circuit parameters for two characterized cases when on buses of balanced and nonbalanced loads there is asymmetric voltage.

At the balanced load with asymmetric voltage errors of determination of  $\underline{Y}_{ph}^{nondis}$  and  $\underline{Y}_{ph}^{dis}$  are:

$$\delta \underline{Y}_{ph}^{nondis} = \frac{\underline{Y}_{ph} \cdot \Delta\varphi}{3} \cdot \left( \frac{1}{\underline{U}_A^{\approx}} + \frac{1}{\underline{U}_B^{\approx}} + \frac{1}{\underline{U}_C^{\approx}} \right); \quad (12)$$

$$\delta \underline{Y}_{ph}^{dis} = \underline{Y}_{ph} \cdot \Delta\varphi / \underline{U}_{ph}^{\approx} - \frac{\underline{Y}_{ph} \cdot \Delta\varphi}{3} \cdot \left( \frac{1}{\underline{U}_A^{\approx}} + \frac{1}{\underline{U}_B^{\approx}} + \frac{1}{\underline{U}_C^{\approx}} \right). \quad (13)$$

We simplify the factor  $\left( \frac{1}{\underline{U}_A^{\approx}} + \frac{1}{\underline{U}_B^{\approx}} + \frac{1}{\underline{U}_C^{\approx}} \right)$  assuming

that  $\left| \underline{U}_{A2}^{\approx} / \underline{U}_{A1}^{\approx} \right| \ll 1$ :

$$\begin{aligned} & \left( \frac{1}{\underline{U}_{A1}^{\approx} + \underline{U}_{A2}^{\approx}} + \frac{1}{\underline{U}_B^{\approx}} + \frac{1}{\underline{U}_C^{\approx}} \right) \approx \\ & \approx - \left( \frac{\underline{U}_{A2}^{\approx}}{(\underline{U}_{A1}^{\approx})^2} + \frac{\underline{U}_{B2}^{\approx}}{(\underline{U}_{B1}^{\approx})^2} + \frac{\underline{U}_{C2}^{\approx}}{(\underline{U}_{C1}^{\approx})^2} \right) = - \frac{3 \cdot \underline{U}_{A2}^{\approx}}{(\underline{U}_{A1}^{\approx})^2}. \end{aligned} \quad (14)$$

Then, taking into account (14) the approximate value of  $\delta \underline{Y}_{ph}^{nondis}$  is:

$$\delta \underline{Y}_{ph}^{nondis} \approx - \underline{Y}_{ph} \cdot \Delta\varphi \cdot \frac{\underline{U}_{A2}^{\approx}}{(\underline{U}_{A1}^{\approx})^2}. \quad (15)$$

Taking into account that factor  $\underline{U}_{A2}^{\approx} / (\underline{U}_{A1}^{\approx})^2$  in two order reduces the result of product  $\underline{Y}_{ph} \cdot \Delta\varphi$  в (15), the value of error  $\delta \underline{Y}_{ph}^{nondis}$  can be considered as tending to zero. For example, at  $|\Delta\varphi|$  equal to 10 % of the direct sequence phase value module ( $|\underline{U}_{A1}^{\approx}|$ ) and  $|\underline{U}_{A2}^{\approx}|$  equal to 4 % of  $\left| (\underline{U}_{A1}^{\approx})^2 \right|$  the error of determination  $\underline{Y}_{ph}^{nondis}$  of balanced load will have order of  $-0,004 \cdot \underline{Y}_{ph}$  which corresponds in relative units to  $-0.4$  %.

Error  $\delta \underline{Y}_{ph}^{dis}$  taking into account (14) will be approximately determined as follows:

$$\delta Y_{-ph}^{dis} \approx Y_{-ph} \cdot \Delta \varphi \cdot \left( \frac{1}{U_{-ph}} + \frac{U_{A2}^{\approx}}{(U_{A1}^{\approx})^2} \right). \quad (16)$$

Taking into account that  $U_{A2}^{\approx}/(U_{A1}^{\approx})^2$  is the value of the second order with respect to  $1/U_{-ph}$ , we can write:

$$\delta Y_{-ph}^{dis} \approx Y_{-ph} \cdot \frac{\Delta \varphi}{U_{-ph}}. \quad (17)$$

From (17) it can be seen that the value of error  $\delta Y_{-ph}^{dis}$  will be determined by the value  $\Delta \varphi$ . For example, at  $|\Delta \varphi| = 0.1 |U_{-ph}^{\approx}|$  the order of the error  $\delta Y_{-ph}^{dis}$  is  $0.1 Y_{-ph}$  at the true value  $Y_{-ph}^{dis} = 0$ .

At the unbalanced load with asymmetric voltage we have:

$$\delta Y_{-ph}^{nondis} = \frac{1}{3} \cdot \left( \begin{aligned} & \left| \frac{Y_A}{U_A^{\approx}} \cdot \frac{\Delta \varphi}{U_A^{\approx}} \cdot e^{j(\alpha - \varphi_A)} + \frac{Y_B}{U_B^{\approx}} \cdot \frac{\Delta \varphi}{U_B^{\approx}} \right| \times \\ & \times e^{j(\alpha - \varphi_B)} + \frac{Y_C}{U_C^{\approx}} \cdot \frac{\Delta \varphi}{U_C^{\approx}} \cdot e^{j(\alpha - \varphi_C)} \end{aligned} \right). \quad (18)$$

$$\delta Y_{-ph}^{dis} = Y_{-ph} \cdot \Delta \varphi / U_{-ph}^{\approx} - \frac{1}{3} \cdot \left( \begin{aligned} & \left| \frac{Y_A}{U_A^{\approx}} \cdot \frac{\Delta \varphi}{U_A^{\approx}} \cdot e^{j(\alpha - \varphi_A)} + \right. \\ & \left. + \frac{Y_B}{U_B^{\approx}} \cdot \frac{\Delta \varphi}{U_B^{\approx}} \cdot e^{j(\alpha - \varphi_B)} + \frac{Y_C}{U_C^{\approx}} \cdot \frac{\Delta \varphi}{U_C^{\approx}} \cdot e^{j(\alpha - \varphi_C)} \right), \quad (19)$$

where  $\alpha = \arg(\Delta \varphi)$ ;  $\varphi_{ph} = \arg(U_{-ph}^{\approx})$ .

Let us assume that phase voltages values ( $U_A^{\approx}$ ,  $U_B^{\approx}$  и  $U_C^{\approx}$ ) are approximately symmetrical. Then, with the possibility of an arbitrary rotation of the system of vectors, we have:

$$\begin{aligned} & \left| \frac{Y_A}{U_A^{\approx}} \cdot \frac{\Delta \varphi}{U_A^{\approx}} \cdot e^{j0} + \frac{Y_B}{U_B^{\approx}} \cdot \frac{\Delta \varphi}{U_B^{\approx}} \cdot e^{j120} + \frac{Y_C}{U_C^{\approx}} \cdot \frac{\Delta \varphi}{U_C^{\approx}} \cdot e^{j240} \right| \approx \\ & \approx \frac{|\Delta \varphi|}{|U_{-ph}^{\approx}|} \cdot \left[ Y_A^{dis} \cdot e^{j0} + Y_B^{dis} \cdot e^{j120} + Y_C^{dis} \cdot e^{j240} \right] \end{aligned} \quad (20)$$

Assuming that arguments of disturbing parts of conductivities ( $Y_A^{dis}$ ,  $Y_B^{dis}$  and  $Y_C^{dis}$ ) are such that their multiplication on unit vectors  $e^{j0}$ ,  $e^{j120}$  and  $e^{j240}$  in a sum give a vector  $\left| \frac{Y_A^{dis}}{U_A^{\approx}} \right| + \left| \frac{Y_B^{dis}}{U_B^{\approx}} \right| + \left| \frac{Y_C^{dis}}{U_C^{\approx}} \right|$ , the error module  $\delta Y_{-ph}^{nondis}$  for the case of unbalanced load can be estimated by the following inequality:

$$\left| \delta Y_{-ph}^{nondis} \right| < \frac{|\Delta \varphi|}{|U_{-ph}^{\approx}|} \cdot \left| \frac{Y_{-ph}^{dis}}{U_{-ph}^{\approx}} \right|_{\max}, \quad (21)$$

where  $Y_{-ph \max}^{dis}$  is the maximal phase disturbing conductivity which for the limit case (asymmetric load with star connection (Fig.3) set by one shoulder) equals to:

$$Y_{-ph \max}^{dis} = \frac{2}{3} Y_{-ph}. \quad (22)$$

So, for  $|\Delta \varphi| = 0.1 |U_{-ph}^{\approx}|$  we have

$$\left| \delta Y_{-ph}^{nondis} \right| < 0,067 \cdot \left| \frac{Y_{-ph}^{dis}}{U_{-ph}^{\approx}} \right|.$$

Let us consider the error  $\delta Y_{-ph}^{dis}$  taking into account that the second summand in (19) is  $\delta Y_{-ph}^{nondis}$  (21):

$$\delta Y_{-ph}^{dis} \approx \frac{\Delta \varphi}{U_{-ph}^{\approx}} \cdot \left( Y_{-ph} - \delta Y_{-ph}^{nondis} \right). \quad (23)$$

Taking into account (22), the module of the maximum error value  $\delta Y_{-ph}^{dis}$  can be estimated by the following inequality:

$$\left| \delta Y_{-ph \max}^{dis} \right| < \frac{|\Delta \varphi|}{|U_{-ph}^{\approx}|} \cdot \frac{5}{3} \left| \frac{Y_{-ph}}{U_{-ph}^{\approx}} \right|. \quad (24)$$

Quantitatively, at  $|\Delta \varphi| = 0.1 |U_{-ph}^{\approx}|$ ,  $\left| \delta Y_{-ph \max}^{dis} \right| < 0,17 \cdot \left| \frac{Y_{-ph}}{U_{-ph}^{\approx}} \right|$ .

From the carried out analysis of errors  $\delta Y_{-ph}^{nondis}$  and  $\delta Y_{-ph}^{dis}$  it follows that disturbing parts of conductivities of balanced and unbalanced generalized load can be determined with high accuracy. Determination of disturbing parts is characterized by significant errors commensurate with the exact values of the unknown quantities.

### Conclusions.

The structure of the equivalent circuit of substitution generalized linear loads in three-phase three-wire network is determined by three independent units, which corresponds to the connection diagram of elements in a triangle. The exact definition of the equivalent circuit parameters based on the methodology for measuring the quality parameters of electric energy is not technically feasible. A method for the approximate determination of the parameters of the equivalent circuit of substitution generalized linear load based on an approximate determination of the phase voltages. Errors calculating nondisturbing parts equivalent circuit parameters of generalized linear substitution loads are characterized by small quantities, which can be neglected. Errors calculation distorting parts may reach values comparable with the exact values.

### REFERENCES

1. Kartashev I., Tulsy V., Shamonov R. Assessing of impact of disturbing load on power quality. *17th International Conference on Electricity Distribution*. Barcelona, 12-15 May, 2003. pp. 1-5.
2. Zhezhenko I.V., Shidlovskiy A.K., Pivnyak G.G., Sayenko Yu.L., Noyberger N.A. *Elektromagnitnaya sovместimost potrebitel'ey* [Electromagnetic compatibility of customers]. Moscow, Mashinostroenie Publ., 2012. 349 p. (Rus).

3. Chepmen D. Price of low power quality. *Energoberezhnie - Energy Saving*, 2004, no.1, pp. 66-69. (Rus).
4. Sayenko Yu., Kalyuzhniy D. Analytical methods for determination of the factual contributions impact of the objects connected to power system on the distortion of symmetry and sinusoidal waveform of voltages. *Przeglad Elektrotechniczny*, 2015, vol.11, pp. 81-85. doi: **10.15199/48.2015.11.23**.
5. Gamazin S.I., Petrovich V.A. Determining the actual contribution of the consumer in the distortion of the quality parameters of electric energy. *Promyishlennaya energetika*, 2003, no.1, pp. 38-42. (Rus).
6. Aiqiang Pan, Jian Zhou. Power quality analysis and harmonic tracing in city grid based on big monitoring data. *23rd International Conference on Electricity Distribution*. Lyon, 15-18 June 2015. pp. 1-4.
7. Sayenko Y., Sukhonos M., Kalyuzhniy D., Bolgov V. Mathematical model for real-time assessment of contributions of disturbing sources to power quality level at a Point of Common

Coupling. *10th Electric Power Quality and Supply Reliability (PQ) Conference*, Tallinn, 29-31 August, 2016, pp. 29-35. doi: **10.1109/pq.2016.7724085**.

Received 29.09.2016

Yu.L. Sayenko<sup>1</sup>, Doctor of Technical Science, Professor,  
D.N. Kalyuzhniy<sup>2</sup>, Candidate of Technical Science, Associate Professor,

<sup>1</sup> Pryazovskyi State Technical University,  
7, Universytets'ka Str., Mariupol, 87500, Ukraine,  
phone +38 0629 446551, e-mail: YuriSayenko@mail.ru

<sup>2</sup> O.M. Beketov National University of Urban Economy  
in Kharkiv,

12, Revolution Str., Kharkiv, 61002, Ukraine,  
phone +38 050 5606835, e-mail: KalyuzhniyDN@mail.ru

How to cite this article:

Sayenko Yu.L., Kalyuzhniy D.N. Identification of generalized linear load in three-phase three-wire network in the problem of the distribution of actual contributions at the point of common coupling. *Electrical engineering & electromechanics*, 2016, no.6, pp. 65-69. doi: 10.20998/2074-272X.2016.6.11.

I.V. Khomenko, S.K. Berezka, I.V. Poliakov

## ANALYSIS OF OPTIMUM OPERATING MODES OF POWER TRANSFORMERS UNDER OPERATING CONDITIONS

*Purpose.* The study of parallel operation optimal modes of transformer equipment for a variety of operating conditions: same or different types of transformers, with or without reactive power flows. *Methodology.* Losses of energy in transformers make 30 % of all losses. Therefore the choice of the economically justified parallel operation of transformers is effective action to reduce losses. Typically, in the calculations of reactive power flows in the transformers are not taken into account. It is interesting to analyze the optimal operating conditions of transformers with and without reactive power flows. *Results.* Calculations for transformers in distribution networks showed that the inclusion of reactive power flows in transformers significant impact on the calculated optimum regimes of transformers. References 9, tables 1, figures 2.

*Key words:* transformer equipment, parallel operation, optimal mode, reactive power, economically reasonable mode.

*Приведены теоретические и практические положения оптимальности режимов работы трансформаторного оборудования на подстанции при их параллельной работе. Расчеты адаптированы для реальных условий эксплуатации для энергетики Украины.* Библ. 9, табл. 1, рис. 2.

*Ключевые слова:* трансформаторное оборудование, параллельная работа, оптимальный режим, реактивная мощность, экономически целесообразный режим.

**Introduction.** In the power system of Ukraine in operation there are more than 100 high-voltage substations. At the same time in parallel operation can be up to four transformers at a substation. At the same time a substantial part of all electricity losses account for losses in transformers. Therefore, any cost-effective modes of transformers in substations are effective measures to reduce energy losses.

Theoretical studies provide enough valid recommendations for optimizing the operation of the transformer equipment based on catalog data. However, in actual use due to the aging of the individual elements of the transformer has to operate passport or experimental values. Experiments show that the values of no-load losses are most affected. When operating of transformer over 20 years loss value can be increased by 1.75 % per year [1].

**Analysis of recent investigations and publications.** The problem of reducing losses in power transformers are engaged many scientists both domestic and foreign. In the end, it all comes down to the controversial problem of determining the optimal test operation of transformers in substations. The most widely used graph-analytic methods.

The optimization criterion of minimum active power losses presented in [2]. This approach is simple, gives good qualitative results in terms of operation but requires significant additions.

In [3] the criterion discussed above is designed to meet the reactive power flows. The proposed method improves the accuracy of calculations, bringing the theoretical calculations to real practical results in the field.

The optimization criterion of minimum energy loss is represented in [4]. This approach is different interpretations are today widely used in a variety of regulatory, scientific and practical materials. These criteria are effective, but require a sufficiently accurate and reliable de-

termination of the time of inclusion in the work of power transformers.

Optimization criteria given transformer efficiency values presented in [5]. This complex combination of important characteristics of the transformer equipment requires precise calculations and studies [6], but clearly is of great scientific and practical interest.

Connection of optimization criteria and the period of service of power transformers are presented in [7].

Based on the literature and the wide statistical material can draw the following conclusion: any optimization criteria reflect the various aspects of efficient operation of power transformers. Addressing practical value criteria optimal performance of parallel-connected transformers is impossible without taking into account the reliability of power supply circuits, load profiles, on-time, the technical condition of the main power equipment (transformers, switches).

**The goal of investigations** is a comparative analysis of the optimal mode of parallel operation of transformer equipment for a variety of operating conditions and the same type for different types of transformers, with and without reactive power flows. As an optimization criterion used for at least the total active power losses. In view of the above, this problem is an actual scientific and practical problem [6, 8].

**Theoretical principles.** Most economic mode corresponds to a load of transformers, proportional to their nominal power [9].

Economic load distribution between parallel operating transformers occurs in the case of identical parameters. Unfortunately, in practice it is not always possible to achieve such a position that would have on each substation transformers are of the same type. This transformer load will be slightly different from the economic due to the occurrence of circulating currents.

To determine the most economical mode of transformers built according to the loss of its power load of transformers  $\Delta P_t = f(S)$ .

Consider the substation with  $n$ -parallel operating transformers of the same type. Power loss in the transformers of the same type, excluding the reactive power flows are according to the formula:

$$\Delta P_T = n \cdot \Delta P_0 + \frac{1}{n} \cdot \frac{\Delta P_k \cdot S^2}{S_{rat}^2}, \quad (1)$$

where  $n$  is the number of parallel operating transformers;  $\Delta P_0$  is the no-load losses of the transformer;  $\Delta P_k$  is the losses of short-circuit of the transformer;  $S$  is the load power;  $S_{rat}$  is the nominal power of the transformer.

Power losses in the transformers of the same type based on the reactive power flows are according to the formula:

$$\Delta P_T = n \cdot (\Delta P_0 + K \cdot Q_{Fe}) + \frac{1}{n} \cdot \frac{(\Delta P_k + K \cdot Q_{Cu}) \cdot S^2}{S_{rat}^2}, \quad (2)$$

where  $K$  is the coefficient equal 0.08;

$$Q_{Fe} = \frac{I_0 \cdot S_{rat}}{100} \quad (3)$$

is the reactive power losses in the steel,  $I_0$  is the transformer no-load current;

$$Q_{Cu} = \frac{U_k \cdot S_{rat}}{100} \quad (4)$$

is the reactive power losses in the copper,  $U_k$  is the transformer no-load voltage.

If installed at the substation transformers of different type or different power, they will have different losses  $P_0$  and  $P_k$ . Use under these conditions of inequality can not be listed above. Then to select the number of parallel-connected transformers are the curves shown losses. They build on the coordinate plane for each transformer for several simultaneously [3].

The power loss for different types of transformers without taking into account the reactive power flows:

$$\Delta P_T = \sum P_0 + \sum P_k \cdot \frac{\sum S^2}{\sum S_{rat}^2}. \quad (5)$$

The power loss for different types of transformers, taking into account the reactive power flows:

$$P_T = \sum (P_0 + K \cdot Q_{Fe}) + \sum (P_k + K \cdot Q_{Cu}) \cdot \frac{\sum S^2}{\sum S_{rat}^2}. \quad (6)$$

If the substation is installed  $n$  three-winding transformers with capacities of all three windings, equal to the nominal capacity of the transformer  $S_T$ , it is necessary to postpone the loading  $S_{SUB}$  substation on the  $x$ -axis:

$$S_{sub} = \sqrt{(S_{LV}^2 + S_{MV}^2 + S_{HV}^2)} / 2. \quad (7)$$

Indeed, in this case, the expression takes the form:

$$\Delta P_{sub} = n \cdot \Delta P_0 + \frac{R_{100}}{n} \cdot \left( \frac{S_{HV}^2 + S_{MV}^2 + S_{LV}^2}{U_{rat}^2} \right), \quad (8)$$

where  $R_{100}$  is the rated the active resistance of the coil, which is equal to the power 100 % of  $S_T$ :

$$R_{100} = \Delta P_k \cdot U_{rat}^2 / (2S_T^2). \quad (9)$$

Substituting this relation in (8), together with (7) we obtain

$$\Delta P_{sub} = n \cdot \Delta P_0 + \frac{P_k}{n} \cdot \left( \frac{S_{sub}}{S_T} \right)^2. \quad (10)$$

In those cases where a low voltage output winding (LV) of the transformer is 50, 40, or 25 % of nominal,  $R_{100}$  resistance must be correspondingly increased in 2, 2.5 or 4 times, after which it will be equal to the resistance given winding LV. If by « $a$ » denote the coefficient of resistance reduction, in general terms the value of the dummy load of three-winding transformers can be represented as follows:

$$S_{sub} = \sqrt{(aS_{LV}^2 + S_{MV}^2 + S_{HV}^2)} / 2. \quad (11)$$

**Calculations.** As initial data for calculation examples we use the passport data of transformers ТРДН-80000/110 and ТРДН-63000/110 of life of 32 and 37 years, respectively (Table 1). The calculations were performed in the environment *MathCad*.

Table 1

Passport data of transformers

|  | ТРДН 80000/110 | ТРДН-63000/110 |
|--|----------------|----------------|
| Rated power $S_{rat}$ , MVA            | 80             | 63             |
| Short-circuit losses $\Delta P_k$ , MW | 0.310          | 0.245          |
| No-load losses $\Delta P_0$ , MW       | 0.0696         | 0.06           |
| No-load current $I_0$ , %              | 0.5            | 0.5            |
| Short-circuit voltage $U_k$ , %        | 10.5           | 10.5           |
| $K$                                    | 0.08           | 0.08           |

#### Example 1.

We optimize the work of similar ТРДН-80000/110  $n = 3$ , without taking into account the reactive power flows.

Total losses, depending on the number of parallel operating transformers ( $n$ ) and the load ( $S$ ) are defined by the expression (1).

Load range  $S = 0 \dots 110$ . Optimization zones are shown in Fig. 1, *a*.

#### Example 2.

We optimize the work of similar ТРДН-80000/110  $n = 3$ , taking into account the reactive power flows.

Reactive power losses in the steel are determined by the expression (3)  $Q_{Fe} = 0.4$  MVar, and in copper - by the expression (4)  $Q_{Cu} = 8.4$  MVar.

Total losses, taking into account the reactive power losses are determined by the expression (2).

Load range  $S = 0 \dots 100$ . Optimization zones are shown in Fig. 1, *b*.

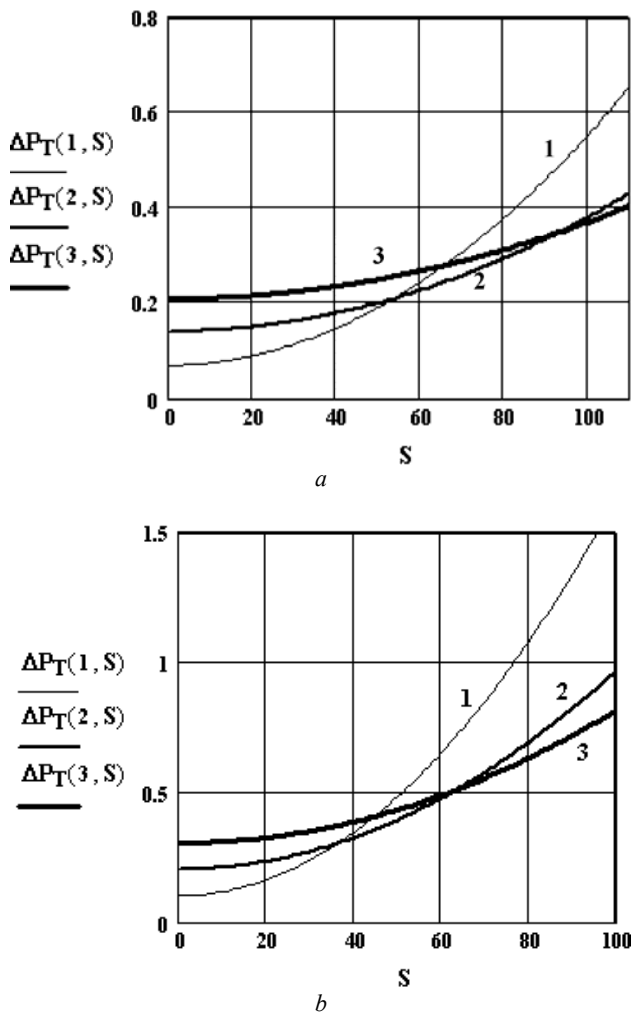


Fig. 1. Dependence of power losses on the load and the number of similar transformers ТРДН-80000/110 (1 - one transformer operates, 2 - two transformer operate; 3 - three transformers operate):  
*a* - excluding the flow of reactive power;  
*b* - taking into account the flow of reactive power

**Example 3.**

We optimize the diverse ТРДН-80000/110 and ТРДН-63000/110 transformers operation excluding reactive power flows.

$$\Delta P_{T1}(S) := \Delta P_{0,1} + \frac{\Delta P_{k1} \cdot S^2}{S_{rat1}^2} - \text{losses in ТРДН-80000/110,}$$

$$\Delta P_{T2}(S) := \Delta P_{0,2} + \frac{\Delta P_{k2} \cdot S^2}{S_{rat2}^2} - \text{losses in ТРДН-63000/110,}$$

Total losses are determined by (5).

Load range  $S = 0 \dots 60$  MVA. Optimization zones are shown in Fig. 2,*a*.

**Example 4.**

We optimize the diverse transformers ТРДН-80000/110 and ТРДН-63000/110 taking into account the reactive power flows.

Reactive power losses in the steel and copper of the indicated transformers are determined by (3) – (4):  $Q_{Fe1} = 0.4$  MVar,  $Q_{Cu1} = 8.4$  MVar,  $Q_{Fe2} = 0.315$  MVar,  $Q_{Cu2} = 6.615$  MVA.

$$\Delta P_{T1}(S) := (\Delta P_{0,1} + K \cdot Q_{Fe1}) + \frac{(\Delta P_{k1} + K \cdot Q_{Cu1}) \cdot S^2}{S_{rat1}^2} .-$$

losses in ТРДН-80000/110,

$$\Delta P_{T2}(S) := (\Delta P_{0,2} + K \cdot Q_{Fe2}) + \frac{(\Delta P_{k2} + K \cdot Q_{Cu2}) \cdot S^2}{S_{rat2}^2} .-$$

losses in ТРДН-63000/110,

Total losses are determined by (6).

Load range  $S = 0 \dots 40$  MVA. Optimization zones are shown in Fig. 2,*b*.

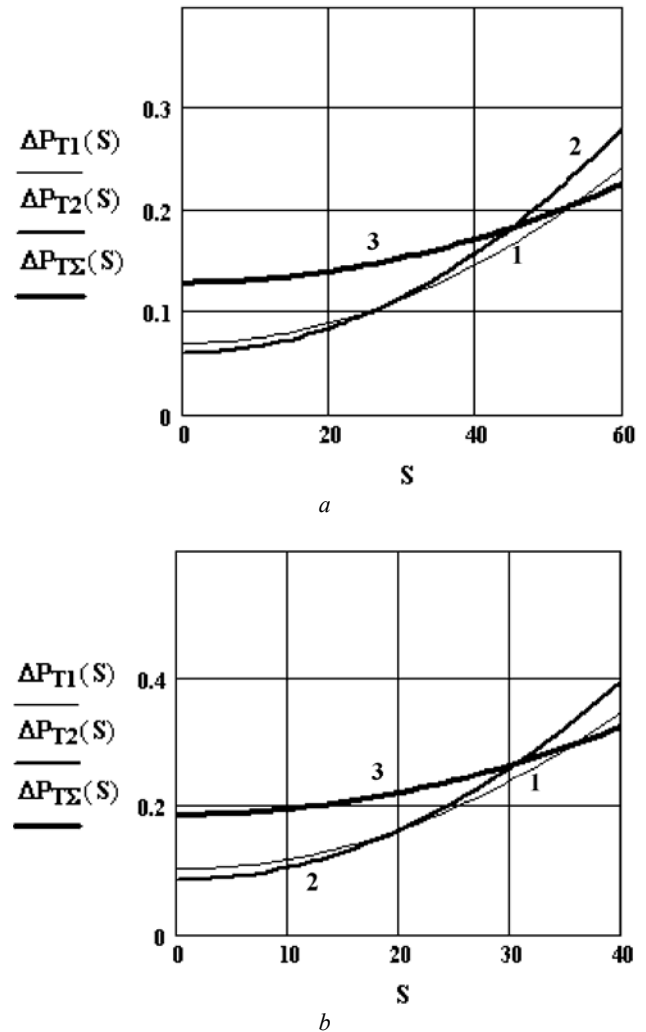


Fig. 2. Dependence of power losses in transformers of different types of loads (1 - transformer ТРДН-80000/110 operates, 2 – transformer ТРДН-63000/110 operates; 3 - both transformers operate):  
*a* - excluding the flow of reactive power;  
*b* - taking into account the flow of reactive power

**Conclusions.**

As a result of the calculations optimization zones of transformer equipment of the substation at their parallel operation are determined. The calculations were performed for the actual operating conditions: for the same type and different types of transformers, with and without reactive power flows.

Comparative analysis shows errors due to the use of certain optimization techniques that ultimately determine the admissibility of their use. Maximum error due to the

difference of catalog and passport data for the cases examined, does not exceed 20 %.

#### REFERENCES

1. Korotkov V.V., Kozlov A.B., Korotkov A.V. Quantification of losses depending on the idling of power transformers lifetime. *Proceedings of the Ivanovo State Power University*, 2007, iss.8, pp. 351-356. (Rus).
2. Radkevich V.N., Trutnikov A.L. On the choice of optimization of the criterion power transformer. *Energy and management*, 2004, no.4-5, pp. 32-33. (Rus).
3. Filatov A.A. *Obsluzhivanie elektricheskikh podstantsiy operativnyim personalom* [Service of electric substations by operation personnel]. Moscow, Energoatomisdat Publ., 1990. 304 p. (Rus).
4. *Metodyka vyznachennia neratsionalnogo vykorystannia palyvno-energetychnyh resursiv*. [Method of determining the irrational (inefficient) use of energy resources]. Kyiv, NAER Publ., 2009. 134 p. (Ukr).
5. Fursanov M.I. *Metodologia i praktika opredelenia i analiza poter elektroenergii*. Autoref. diss. dokt. tekhn. nauk [Methodology and practice of identification and analysis of power losses in electric networks of power supply. Abstracts of doct. tech. sci. diss.] Minsk, 2002. 39 p. (Rus).
6. Gonchar A.A. On criteria for optimization of the power transformer. *Energy and management*, 2004, no.2, p. 45. (Rus).
7. Balabin A.A. *Razrabotka metodiki raschete poter elektroenergii v magniti provodah dlitelno ekspluatiruyuschihsia transformatorov*. Autoref. diss. kand. tekhn. nauk [Development of the method of calculating energy losses in magnetic wires long maintained power transformers. Abstracts of cand. tech. sci. diss.]. Orel, 2009. 18 p. (Rus).
8. Kutsenko G.F., Parfenov A.A. Selecting distribution transformers 6-10 kV at a minimum electricity losses. *Energy efficiency*, 2001, no.11, pp. 18-19. (Rus).
9. Idelchik V.I. *Elektricheskie sistemy i seti: Uchebnik dlia vuzov* [Electrical Systems and Grids: Textbook for high schools]. Moscow, Energoatomisdat Publ., 1989. 592 p. (Rus).

Received 01.09.2016

I.V. Khomenko<sup>1</sup>, Candidate of Technical Science, Associate Professor,  
S.K. Berezka<sup>1</sup>, Candidate of Technical Science,  
I.V. Poliakov<sup>1</sup>, Candidate of Technical Science, Associate Professor,  
<sup>1</sup>National Technical University «Kharkiv Polytechnic Institute»,  
21, Kyrpychova Str., Kharkiv, 61002, Ukraine,  
e-mail: igor.v.khomenko@gmail.com, serg.berezka@gmail.com

#### How to cite this article:

Khomenko I.V., Berezka S.K., Poliakov I.V. Analysis of optimum operating modes of power transformers under operating conditions. *Electrical engineering & electromechanics*, 2016, no.6, pp. 70-73. doi: 10.20998/2074-272X.2016.6.12.